

# Microstructural modeling of ferroelectric material behavior

vom Fachbereich Maschinenbau und Verfahrenstechnik  
der Technischen Universität Kaiserslautern  
zur Verleihung des akademischen Grades

**Doktor-Ingenieur (Dr.-Ing.)**

genehmigte

**Dissertation**

von

**Dipl.-Ing. David Schrade**

aus Darmstadt

Hauptreferent: Prof. Dr.-Ing. Ralf Müller

Korreferenten: Prof. Dr.-Ing. Dietmar Gross

Prof. Dr.-Ing. Sven Klinkel

Vorsitzender: Prof. Dr.-Ing. Martin Eigner

Dekan: Prof. Dr.-Ing. Siegfried Ripperger

Tag der Einreichung: 24.11.2010

Tag der mündlichen Prüfung: 28.04.2011

Kaiserslautern, 2011

D386

## **Herausgeber**

Lehrstuhl für Technische Mechanik  
Technische Universität Kaiserslautern  
Gottlieb-Daimler-Straße  
Postfach 3049  
67653 Kaiserslautern

© David Schrade

Ich danke der „Prof. Dr. Hans Georg und Liselotte Hahn Stiftung“ für die finanzielle Unterstützung bei der Drucklegung.

## **Druck**

Lasertype GmbH Darmstadt

Alle Rechte vorbehalten, auch das des auszugsweisen Nachdrucks, der auszugsweisen oder vollständigen Wiedergabe (Photographie, Mikroskopie), der Speicherung in Datenverarbeitungsanlagen und das der Übersetzung.

ISBN 978-3-942695-03-9

# Vorwort

Die vorliegende Arbeit ist größtenteils während meiner Tätigkeit am Fachgebiet Festkörpermechanik der Technischen Universität Darmstadt entstanden.

Mein besonderer Dank gilt Herrn Prof. Dr.-Ing. R. Müller für die hervorragende Betreuung und Unterstützung, die sehr zum Gelingen dieser Arbeit beigetragen haben. Ebenfalls danken möchte ich Herrn Prof. Dr.-Ing. D. Gross, der mir die Mitarbeit in seiner Arbeitsgruppe ermöglicht hat und die Forschungsarbeit stets mit Interesse begleitet hat. Weiterhin danke ich Herrn Prof. Dr.-Ing. S. Klinkel für die Übernahme des Korreferates und das damit verbundene Interesse an dieser Arbeit.

Ich möchte mich auch bei meinen ehemaligen Arbeitskolleginnen und -kollegen für die anspruchsvolle wissenschaftliche Umgebung sowie für die ausgesprochen angenehme Arbeitsatmosphäre bedanken. Insbesondere denke ich hier an die fachlichen Diskussionen und nicht-fachlichen Aktivitäten mit meinem ehemaligen Zimmerkollegen Oliver Goy, Xu Baixiang, Christian Sator und Andreas Trondl.

Die grundlegenden Voraussetzungen für diese Arbeit wurden sicherlich vor vielen Jahren gelegt, daher gilt mein Dank an dieser Stelle ebenso meinen Eltern.

Darmstadt, Juni 2011

David Schrade





# Contents

<b>Zusammenfassung</b>	<b>iii</b>
<b>1 Introduction</b>	<b>1</b>
1.1 Motivation . . . . .	1
1.2 Outline . . . . .	2
1.3 Notation . . . . .	3
<b>2 Ferroelectric ceramics</b>	<b>5</b>
<b>3 Basic equations</b>	<b>11</b>
3.1 Motion and deformation . . . . .	11
3.2 Electrostatics . . . . .	15
3.3 Discontinuities . . . . .	23
3.4 Balance equations . . . . .	25
3.5 Piezoelectric constitutive law . . . . .	34
<b>4 Sharp interface approach</b>	<b>37</b>
4.1 Driving force and interface kinetics . . . . .	38
4.2 Numerical aspects . . . . .	41
4.3 Examples . . . . .	43
4.3.1 Electrode defect . . . . .	45
4.3.2 Side defect . . . . .	53
4.3.3 Polarization defect . . . . .	57
<b>5 Phase field approach</b>	<b>61</b>

5.1	Theory . . . . .	62
5.1.1	Thermodynamics . . . . .	63
5.1.2	Phase field potential . . . . .	65
5.1.3	Phase field parameters . . . . .	68
5.2	Numerical implementation . . . . .	72
5.3	Examples . . . . .	76
5.3.1	Introduction . . . . .	76
5.3.2	Parameter verification . . . . .	78
5.3.3	Domain wall pinning . . . . .	86
5.3.4	Microstructure evolution . . . . .	93
5.3.5	Bimodality . . . . .	96
5.3.6	Wedge formation . . . . .	100
<b>6</b>	<b>Effective material behavior</b>	<b>103</b>
6.1	Theory . . . . .	103
6.2	Multiaxial loading . . . . .	107
<b>7</b>	<b>Conclusion</b>	<b>113</b>
	<b>Appendix</b>	<b>115</b>
A.1	Driving force acting on a $180^\circ$ interface . . . . .	115
A.2	Comparison of phase field models . . . . .	115
A.3	Alternative derivation of the evolution equation . . . . .	117
A.4	Parameters of the phase separation potential . . . . .	117
A.5	Element stiffness and damping matrix . . . . .	118
	<b>Bibliography</b>	<b>121</b>

# Zusammenfassung

Ferroelektrische Materialien waren in den letzten Jahrzehnten aufgrund ihrer elektromechanischen und pyroelektrischen Eigenschaften Gegenstand umfangreicher wissenschaftlicher Betrachtungen. Die Kopplung von elektrischen und mechanischen Materialeigenschaften ist von großem Interesse für industrielle Anwendungen, so zum Beispiel in der Aktuator- und Sensortechnik oder bei der Herstellung von ferroelektrischen Ultraschallmotoren.

Die makroskopischen Materialeigenschaften ferroelektrischer Keramiken (andere Typen ferroelektrischer Materialien sind nicht Gegenstand dieser Arbeit) lassen sich anhand ihrer kristallinen Mikrostruktur erklären. Unter den einundzwanzig Kristallklassen, die über kein Symmetriezentrum verfügen, gibt es zehn, die eine eindeutige polare Achse haben und, da positiver und negativer Ladungsschwerpunkt lokal einen Dipol bilden, eine spontane elektrische Polarisierung aufweisen. Die Stärke der spontanen Polarisierung ist temperaturabhängig, was als *pyroelektrischer Effekt* bezeichnet wird. Eine weitere Folge der polaren Symmetrie ist der direkte und inverse *piezoelektrische Effekt*, der die lineare Beziehung zwischen mechanischer Deformation und induzierter dielektrischer Verschiebung bzw. zwischen angelegtem elektrischen Feld und mechanischer Deformation bezeichnet. *Ferroelektrika* zeichnen sich dadurch aus, dass der Polarisationszustand entlang der polaren Achse umgekehrt bzw. geschaltet werden kann; dies betrifft auch die Zustände kristallographisch äquivalenter Achsen. Bereiche einheitlicher Polarisierung werden *Domänen*, ihre Übergänge *Domänenwände* genannt; zusammen bilden sie die mikrostrukturellen Elemente eines Kornes oder Kristallites einer polykristallinen Keramik. Die makroskopischen Materialeigenschaften resultieren aus dem Polungsvorgang, bei dem die anfangs zufällig verteilte Polarisierung sich durch Anlegen eines elektrischen Feldes im Zuge von Schaltvorgängen in dessen Richtung reorientiert. Durch eine möglichst gute Ausrichtung der polaren Achsen wird die gewünschte makroskopische Anisotropie mit ihren piezo- und pyroelektrischen Eigenschaften induziert.

Ziel der vorliegenden Arbeit ist die Simulation der Mikrostrukturentwicklung in ferroelektrischen Materialien auf der Längenskala der ferroelektrischen Domänen. Dazu werden zwei verschiedene Modelle zur Beschreibung der Domänenstruktur herangezogen, die getrennt voneinander behandelt werden. Im ersten Modell werden Domänenwände als scharfe oder singuläre (Grenz-)flächen abgebildet, an der unter anderem die spontane Polarisierung eine Diskontinuität besitzt. Dies ermöglicht, die Grenzflächen als materielle Inhomogenitäten aufzufassen, so dass auf

die Theorie der Konfigurationskräfte zurückgegriffen werden kann. Die homogenen Bereiche werden auf der Basis der elektrischen Enthalpie, additiv erweitert um das Skalarprodukt zwischen spontaner Polarisierung und elektrischem Feld, modelliert. Mit der Lösung des linearen gekoppelten Feldproblems, das mit Hilfe der Finiten-Elemente-Methode (FEM) näherungsweise gelöst wird, lässt sich die thermodynamisch konjugierte (treibende) Kraft auf die Grenzfläche berechnen. Die Bewegung eines Punktes auf der Grenzfläche wird durch die Wahl eines thermodynamisch konsistenten kinetischen Gesetzes beschrieben, das die treibende Kraft mit dessen Geschwindigkeit in Verbindung setzt. Im Hinblick auf Simulationen zu Experimenten an zweidomänen Proben aus Gadoliniummolybdat wird die Komplexität des Problems durch das Betrachten einer einzelnen, planaren Domänenwand reduziert. Die Bewegung der Domänenwand kann dann durch Zeitintegration der Domänenwandgeschwindigkeit verfolgt werden; mit aktualisierter Grenzflächenposition wird dann eine neue FEM-Berechnung gestartet. Die numerischen Simulationen, die sich auf den 2d-Fall beschränken, beziehen sich zum Teil auf experimentelle Studien, in denen der Einfluss von verschiedenen Defekten auf die Mobilität einer  $180^\circ$  Domänenwand, die mit Hilfe eines elektrischen Feldes in Richtung der Flächennormalen bewegt wird, untersucht wurde. Dabei stimmen Experiment und Simulation qualitativ insoweit überein, als in beiden Fällen eine beschädigte Elektrode die Domänenwandmobilität einschränkt und die Grenzfläche zum Stoppen bringen kann (*domain wall pinning*) und weiterhin als ein seitlicher Defekt, der die Elektroden unberührt lässt, keinen wesentlichen Einfluss auf die Domänenwandmobilität hat. Ein Polarisationsdefekt, gekennzeichnet durch nicht-schaltbare Polarisierung, hat ebenfalls einen *pinning*-Effekt auf die Domänenwand.

Der Schwerpunkt dieser Arbeit liegt in der Mikrostruktursimulation mittels eines Phasenfeldmodells, in dem die Unstetigkeiten des Grenzflächenmodells durch Einführung eines zweifach stetig-differenzierbaren Ordnungsparameters reguliert werden. Abweichend von anderen Arbeiten auf diesem Gebiet, in denen die gesamte materielle Polarisierung als Ordnungsparameter verwendet wird, dient hier die *spontane* Polarisierung zur Beschreibung des Polungszustandes. Innerhalb einer Domäne ist der Ordnungsparameter homogen verteilt; an Domänengrenzen findet ein glatter Übergang von einer spontan polarisierten Variante in eine andere statt. Der Ordnungsparameter wird als zusätzliche unabhängige Feldvariable zusammen mit dem konjugierten Mikrospannungstensor in den zweiten Hauptsatz der Thermodynamik eingearbeitet. Das thermodynamische Potential setzt sich additiv aus einer modifizierten elektrischen Enthalpie, die ordnungsparameterabhängige Materialkonstanten enthält, einem Phasenseparationspotential, das die Bildung von Domänen erlaubt, und einem Gradientenpotential, das der Regularisierung der Domänengrenzen dient. Nach der Gewinnung von Materialgesetzen

für die Cauchyspannung und die elektrische Verschiebung liefert eine Auswertung der Dissipationsungleichung eine nichtlineare Evolutionsgleichung für die spontane Polarisierung, die vom Ginzburg-Landau-Typ ist. Die im Zusammenhang mit dem Separations- und Gradientenpotential eingeführten Parameter werden mit Hilfe eines 1d-Modells als spezifische Energiedichte und charakteristische Breite einer  $180^\circ$  Domänenwand identifiziert. Diese Erkenntnis erweist sich als hilfreich in der numerischen Behandlung des Phasenfeldmodells, das in das FE-Programm *FEAP* implementiert wurde. Dabei werden der Verschiebungsvektor, das elektrische Potential und der Ordnungsparameter als Knotenfreiheitsgrade definiert, um damit die gekoppelten mechanischen und elektrostatischen Feldgleichungen näherungsweise zu lösen; die zeitliche Integration der Evolutionsgleichung wird mit einem impliziten Verfahren erster Ordnung unter Anwendung der Newton-Raphson-Methode durchgeführt. Im Ergebnisteil wird zunächst eine Reihe von Simulationen zur Verifikation der verwendeten Voraussetzungen und Parameter sowie der grundlegenden Modelleigenschaften vorgestellt; dies beinhaltet Statik und Dynamik von  $180^\circ$  und  $90^\circ$  Domänenwänden. Eine weitere Reihe von Simulationen ist der Frage nach dem Einfluss von Elektroden-, seitlichen und Polarisationsdefekten auf die Mobilität der beiden Domänenwandtypen gewidmet. Je nach der Stärke des angelegten elektrischen Feldes, der Defektgröße oder der Art der Defektmodellierung lässt sich insgesamt ein einschränkender Effekt auf die Domänenwandmobilität, insbesondere *domain wall pinning*, feststellen. In weiteren Simulationen werden die Mikrostrukturentwicklung ausgehend von einer zufällig verteilten Anfangspolarisation sowie bimodale und keilförmige Domänenkonfigurationen untersucht. Das experimentell beobachtete Auftreten von bimodalen, also alternierenden schmalen und breiten  $90^\circ$  Domänen, kann in der Simulation einerseits als Folge elektrischer, andererseits als Folge mechanischer Effekte reproduziert werden. Die ebenfalls experimentell festgestellten spitz zulaufenden keilförmigen Domänen können als Folge elektrischer Gegebenheiten an den Keilspitzen gedeutet werden.

Im Umgang mit dem Phasenfeldmodell hat sich gezeigt, dass das Separationspotential, zusammen mit der modifizierten elektrischen Enthalpie, sich für die Simulation des makroskopischen Materialverhaltens bei uniaxialen elektrischen und mechanischen Belastungen eignet. Dies ist der Ausgangspunkt für die Simulation von multiaxialen Polungsexperimenten, in denen "Fließflächen" für die irreversible Polarisierung konstruiert wurden. Die makroskopische Modellantwort wird durch einen Mittelungsprozess über die Antworten einer Reihe von Simulationen mit verschieden orientierten Kristallachsen erhalten. Die so gewonnenen Fließflächen befinden sich in unerwartet guter Übereinstimmung mit den experimentell bestimmten Fließflächen.



# Chapter 1

## Introduction

### 1.1 Motivation

Ferroelectric ceramics are polycrystalline solids exhibiting strongly non-linear dielectric properties which are related to electrically polarizable domains on the microscopic length scale. After the manufacturing process, which involves the sintering of powders, the material is poled by the application of an external electric field. The microstructural changes during the poling process induce macroscopic material anisotropy with respect to the electrical, mechanical, and thermal properties. As in many materials, these physical properties exhibit some degree of coupling. For example, all solids respond to an electric field with a strain that is quadratic in the applied field. Coupling effects are often weak and therefore neglected, but in the case of ferroelectrics the electromechanical coupling due to the direct and inverse piezoelectric effect is strong enough to be useful in industrial applications such as sensors, actuators, transducers, or ultrasonic motors.

Although most applications are limited to the linear small-signal range, it is important to understand the underlying microstructural aspects. The initial poling process, by which the material receives its electromechanical properties, involves complex changes in the domain structure. Also, the local conditions at electrode tips, defects, or other boundaries may cause microstructural changes that may possibly compromise the desired macroscopic or microscopic behavior (as e.g. in non-volatile ferroelectric RAMs).

The simulation techniques for ferroelectric material behavior mainly depend on the considered length scale. Phenomenological models are most useful for the simulation of the macroscopic material behavior relevant to applications. These models are not further discussed here, instead the reader is referred to the review articles

by KAMLAH (2001) and LANDIS (2004) as well as to the broad overview given in MEHLING (2007). Micromechanically motivated formulations make simplifying assumptions about the effective polarization state of individual grains (e.g. HWANG ET AL. 1995, MICHELITSCH & KREHER 1998, LU ET AL. 1999); some models consider multiple domain states within a grain (e.g. CHEN ET AL. 1997, HUBER ET AL. 1999, KIM ET AL. 2003). Energetic switching criteria are used to determine when phase transformations in grains or volume fractions of grains take place. Finite element homogenization is used e.g. in HWANG & ARLT (2000) and KAMLAH ET AL. (2005).

While the cited models are based on effective poling states of individual grains to describe the macroscopic behavior, the focus of this work lies on the modeling of the microstructure and its evolution on the length scale of ferroelectric domains. Domain structures are characterized by regions of homogeneous polarization within a grain which are separated by atomically thin interfaces, so-called *domain walls*. Geometrically, these interfaces may be modeled as singular surfaces with vanishing thickness or as continuous transitions between differently polarized domains. The first concept allows for the application of the theory of configurational forces, since sharp interfaces can be interpreted as material inhomogeneities. Within the second, so-called *phase field* approach, the local polarization state is described by an order parameter which enters the thermodynamic problem as an independent field variable and evolves due to a time-dependent Ginzburg-Landau type evolution equation.

The following section gives a brief outline of the contents; further details on the two modeling approaches, including literature citations, can be found at the beginnings of Ch. 4 and 5.

## 1.2 Outline

The focus of this work lies on the simulation of ferroelectric domain structures. Chapter 2 gives an overview of ferroelectric ceramics with respect to crystallographic aspects, the electromechanical coupling principle, microstructure, and macroscopic material behavior.

Chapter 3 provides basic continuum-mechanical and electrostatic material for later reference in the description of the sharp interface and phase field model. This includes a review of discontinuities and a general statement of the thermo-mechanical and electric balance equations leading to the formulation of the linear piezoelectric material law.



Chapter 4 is devoted to the sharp interface simulation approach. The driving force on a domain wall, which can be viewed as a material inhomogeneity, is obtained from thermodynamic considerations. By describing the interface position with a single parameter, an average driving force is defined to postulate a thermodynamically consistent kinetic relation for the interface velocity. The resulting linear field problem is then implemented using standard finite element techniques; explicit numerical time integration is adopted for the interface position. Numerical simulations for single crystal gadolinium molybdate are used to study the effect of different kinds of defects on the domain wall mobility.

Chapter 5 introduces the phase field approach in which phase transformations are modeled with a continuous order parameter, i.e. the spontaneous polarization. The introduction of the vector-valued order parameter adds another independent variable, which is included in the thermodynamic framework developed in Sec. 5.1.1. This procedure gives a non-linear time-dependent Ginzburg-Landau type evolution equation for the spontaneous polarization. The electric enthalpy introduced in Sec. 3.5 is altered to account for poling-dependent material parameters; furthermore, it is extended by a phase separation and gradient potential to allow for the formation of domains and non-vanishing interface widths. The additional model parameters are then identified and physically interpreted in Sec. 5.1.3. The model is implemented in a finite element scheme in which the order parameter enters as a nodal degree of freedom. Implicit time integration of the evolution equation in context with a non-linear Newton scheme and the use of the algorithmic tangent yields a robust numerical solution strategy. In Sec. 5.3, the model is first validated with a series of basic simulations. Further examples include domain wall pinning at different kinds of defects, microstructure evolution, and bimodally and wedge-shaped domain structures.

In Ch. 6, a microscopically motivated model is derived from the phase field model to be utilized for the simulation of multiaxial poling experiments.

## 1.3 Notation

Symbolic notation is used in most equations throughout this work. Scalar quantities are denoted by non-bold, italic Latin or Greek letters (e.g.  $a$ ,  $H$ ,  $\Theta$ ). Vectors are indicated by boldface italic letters such as  $\mathbf{u}$  or  $\boldsymbol{\Sigma}$ . Components of higher-order quantities with respect to an orthonormal basis system are indexed with italic letters, i.e.  $(\mathbf{P})_i = P_i$ . Second-order tensors are identified by boldface non-italic letters ( $\mathbf{A}$ ,  $\mathbf{F}$ ) and, in some instances, by boldface Greek symbols (e.g.  $\boldsymbol{\varepsilon}$ ,  $\boldsymbol{\sigma}$ ).

The third- and fourth-order tensors used are  $\mathbb{C}$ ,  $\mathfrak{e}$ , and  $\mathfrak{d}$ , besides the fourth-order identity tensor  $\mathbb{1}$ . The second-order identity tensor is denoted by  $\mathbf{1}$ , its components are  $\delta_{ij}$  (the Kronecker symbol);  $\epsilon_{ijk}$  are the components of the permutation tensor.  $(\mathbf{A}^T)_{ij} = A_{ji}$  and  $(\mathfrak{e}^T)_{ijk} = \epsilon_{kij}$  is used for the transposition operator along with  $\mathbf{A}^{-T} = (\mathbf{A}^{-1})^T$ . The subscripts  $(\cdot)_{\text{sym}}$  and  $(\cdot)_{\text{skew}}$  give the symmetric and skew-symmetric part of a second tensor, respectively. For multiplications, the notation  $(\mathbf{A}\mathbf{u})_i = A_{ik}u_k$ ,  $(\mathbb{C}\boldsymbol{\varepsilon})_{ij} = \mathbb{C}_{ijkl}\varepsilon_{kl}$ ,  $(\mathbf{A}\mathbf{B})_{ij} = A_{ik}B_{kj}$  are exemplary. The dyadic product between two vectors is denoted by  $\mathbf{u} \otimes \mathbf{v}$ . Inner products are written as  $\mathbf{u} \cdot \mathbf{v} = u_k v_k$  and  $\mathbf{A} \cdot \mathbf{B} = A_{ij}B_{ij} = \text{tr}(\mathbf{A}\mathbf{B}^T)$ , where  $\text{tr} \mathbf{A} = A_{kk}$  is the trace of  $\mathbf{A}$ . The Euclidean norm of a vector and second-order tensor is defined as  $|\mathbf{u}| = \sqrt{\mathbf{u} \cdot \mathbf{u}}$  and  $\|\mathbf{A}\| = \sqrt{\mathbf{A} \cdot \mathbf{A}}$ , respectively. The vector product is denoted as  $\mathbf{u} \times \mathbf{v}$ , and  $(\mathbf{u} \times \mathbf{A})_{ij} = \epsilon_{ikm}u_k A_{mj}$ . The axial vector of a skew-symmetric second-order tensor  $\mathbf{W}$  is given by  $(\text{axl } \mathbf{W})_i = \frac{1}{2}\epsilon_{ijk}W_{kj}$ .

Partial derivatives with respect to  $A$  are sometimes written as  $\partial_A(\cdot)$ ; the material time derivative of  $A$  is indicated by  $\dot{A} = \frac{dA}{dt}$ . The differential operators  $\text{curl}(\cdot)$ ,  $\text{div}(\cdot)$ , and  $\text{grad}(\cdot)$  are the curl, the divergence, and the spatial gradient in the current configuration (in the reference configuration when capitalized). After geometric linearization,  $\nabla(\cdot)$  is used for the sake of brevity;  $\Delta(\cdot)$  denotes the Laplace operator. Specifically,  $(\text{grad } \mathbf{u})_{ij} = u_{i,j}$  and  $(\text{div } \mathbf{A})_i = A_{ik,k}$ , where  $(\cdot)_{,i} = \partial_{x_i}(\cdot)$ . Discretized quantities in context with Voigt notation are denoted by an underbar, e.g.  $\underline{\boldsymbol{\sigma}}$ .

# Chapter 2

## Ferroelectric ceramics

Introductions to the general topic of ferroelectric ceramics can be found in the textbooks by JAFFE ET AL. (1971), JONA & SHIRANE (1993), and XU (1991) (which also covers experimental procedures and non-crystalline ferroelectrics) or e.g. in the review article KAMLAH (2001). The following remarks summarize the main aspects of ferroelectrics relevant to this work.

In crystallography, there are thirty-two crystal classes which classify a given crystal according to its symmetry properties. As is the case for all materials, an applied electric field causes a strain which is quadratic in the applied field; this reversible effect is called *electrostriction*. Of the thirty-two crystal classes, eleven possess a center of symmetry; these centrosymmetric crystals have no polar axes. The remaining twenty-one crystal classes have no center of symmetry and, with the exception of the cubic class 432, exhibit the *piezoelectric effect*. This linear effect occurs when the material is subjected to an elastic strain causing a voltage difference between two sides of the sample. Also, the application of an electric field results in elastic strain; this is the *inverse piezoelectric effect*, which is also linear. Of the twenty non-centric, piezoelectric crystal classes, ten have a unique polar axis and are thus spontaneously polarized. The value of the spontaneous polarization is sensitive to temperature changes of the crystal, this is the so-called *pyroelectric effect*. A crystal is defined as *ferroelectric* if it belongs to the pyroelectric class and if the spontaneous polarization can be reversed or switched by an electric field.

Some of the most relevant ferroelectric crystals have a perovskite-type lattice structure, e.g. barium titanate ( $\text{BaTiO}_3$ ), lead titanate ( $\text{PbTiO}_3$ ), and lead zirconate titanate ( $\text{Pb}(\text{Zr}_{1-x}\text{Ti}_x)\text{O}_3$ ) which is also known as PZT. These materials have a non-polar cubic lattice structure above the Curie temperature and spontaneously polarize when cooled below that temperature. In the case of PZT, the unit

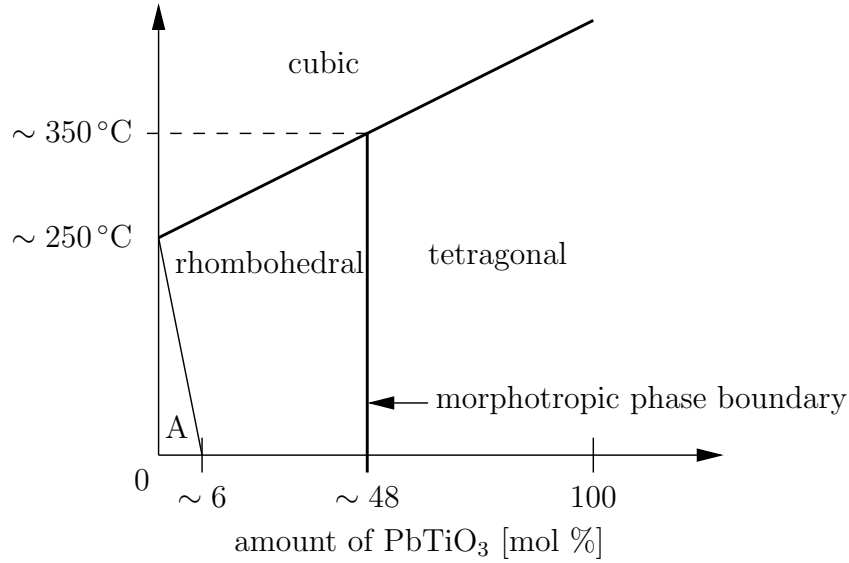


Figure 2.1: Schematic PZT phase diagram. The rhombohedral and tetragonal phase is separated by the morphotropic phase boundary. The antiferroelectric phase labelled “A” is not of interest in the present context.

cell of the polar phase depends on the composition, see Fig. 2.1. However, in the following only tetragonal (besides cubic) unit cells are considered.

The cubic and tetragonal perovskite-type phases of barium titanate and PZT are illustrated in Fig. 2.2. In the course of the phase transition, the central ion of the cubic cell is displaced along the  $c$ -axis so that an electric dipole is created. The spontaneous polarization is then defined as the dipole moment per unit volume. The phase transition is accompanied by a spontaneous strain under which the unit cell is stretched in the polar direction and contracted along the  $a$ -axes. Since the polar  $c$ -axis has two crystallographically equivalent axes in the cubic phase, there are six distinct spontaneous states in 3d; this number reduces to four in 2d and to two in 1d. Since two states with opposite spontaneous polarization exhibit the same spontaneous strain, there are only three different spontaneous strain states in 3d.

A ferroelectric crystal is defined by the ability to switch among spontaneously polarized states. In the perovskite structure under consideration, this is accomplished by either  $180^\circ$  or  $90^\circ$  switching. The former transition is characterized by a change in the absolute value of the spontaneous polarization, the latter primarily by a rotation of the polar axis. Note that a crystal has *ferroelastic* properties if  $90^\circ$  switching can be achieved by the application of purely mechanical loading.

Ferroelectric ceramics are usually not produced as single crystals (which is dif-

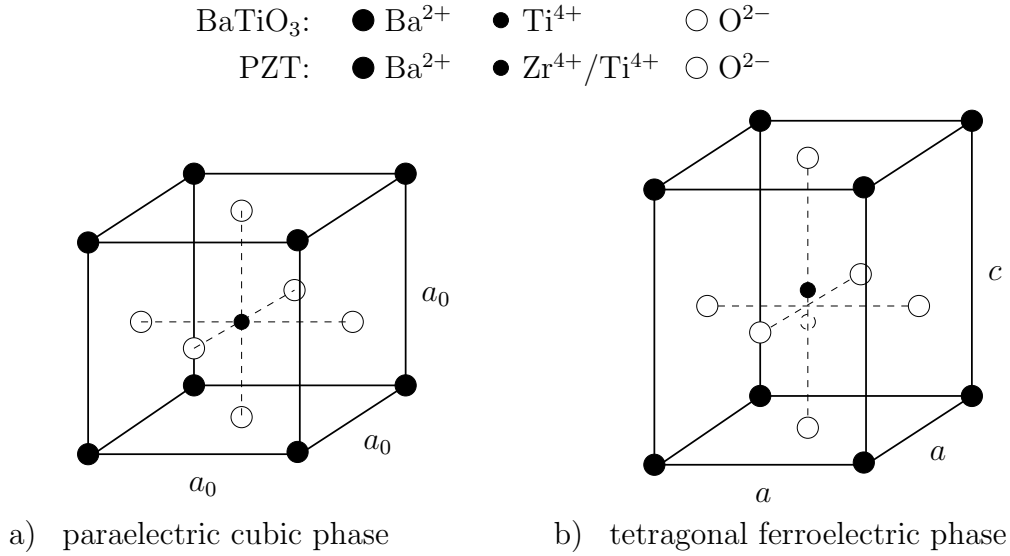


Figure 2.2: Sketch of perovskite structure in barium titanate and PZT. The high-temperature paraelectric phase a) is cubic and non-polar, the low-temperature phase b) has a unique polar axis and becomes tetragonal in the course of the phase transition.

ficult and expensive) but rather as polycrystals consisting of a large number of crystallites or grains. The spatial orientation of the dipoles is generally not homogeneous within one grain; rather, the volume is partitioned in a number of uniformly poled regions, so-called *ferroelectric domains*. The transition region between two adjacent domains is the *domain wall* which has a width of only a few unit cells. In tetragonal systems, only 180° and 90° domain walls are of relevance. As sketched in Fig. 2.3 a), the designation of the interfaces stands for the change in the orientation of the spontaneous polarization across the interface. The complexity of a typical ferroelectric microstructure can be observed in Fig. 2.3 b). Electrical conditions at grain and domain boundaries, internal stresses due to mismatching spontaneous strains, and various kinds of defects in the bulk material or at internal boundaries appear to be important factors for the formation of domain patterns during the phase transition at the Curie temperature.

The macroscopic properties of a ferroelectric ceramic depend on the internal polarization state which is subject to change under electrical or mechanical loading. Due to the ferroelectric effect, the spontaneous states can be switched which leads to domain wall movement and the emergence and growth of new domains at nucleation points. An untreated ferroelectric ceramic has a vanishing net polarization as the randomly distributed polarizations of individual domains add up to zero. By the application of an external electric field, dipoles are reoriented

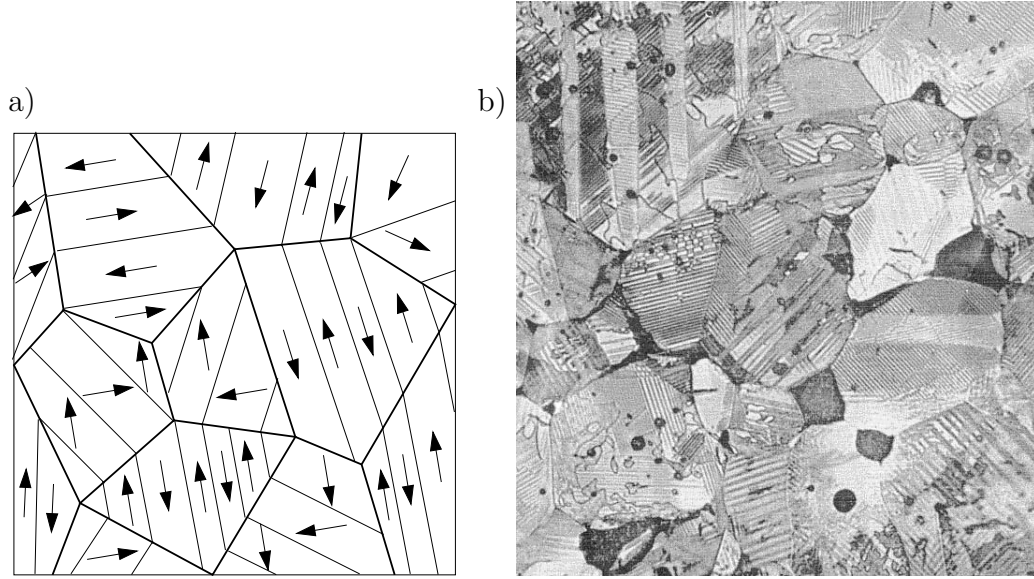


Figure 2.3: a) schematic sketch of a ferroelectric domain structure containing  $180^\circ$  and  $90^\circ$  interfaces; b) ferroelectric microstructure in barium titanate, reprinted from JAFFE ET AL. (1971).

toward a closer alignment with the electric field. This poling process leads to a macroscopically polarized crystal in the direction of the applied field as well as to a macroscopic eigenstrain due to the alignment of the  $c$ -axes with the poling direction. When the electric field is disabled, the microstructural changes during poling are not reversed. The remaining net polarization is called *remanent polarization*, and the macroscopic eigenstrain with respect to the original unpoled state is the *remanent strain*. Furthermore, a poled probe can be mechanically depolarized by the application of a compressive stress in the poling direction. The compressive stress favors a reorientation of the  $c$ -axes orthogonal to the loading direction that is achieved by  $90^\circ$  switching. The resulting state has no remanent polarization but a non-vanishing remanent strain.

The non-linear macroscopic behavior is characterized by the dielectric and butterfly hystereses under cyclic uniaxial electric loading, see Fig. 2.4. Starting at ①, an unpoled probe with randomly polarized domains is loaded with an increasing electric field. The initial response is linear dielectric until the poling process sets in. The degree of poling depends on the strength of the electric field and its ability to switch unaligned polarization. When the polarization of the domains is in optimal alignment with the electric field at ②, further loading only leads to a linear dielectric response. As the electric field is reduced to zero at ③, the net polarization reduces to the remanent polarization. If the probe was fully poled at ①,

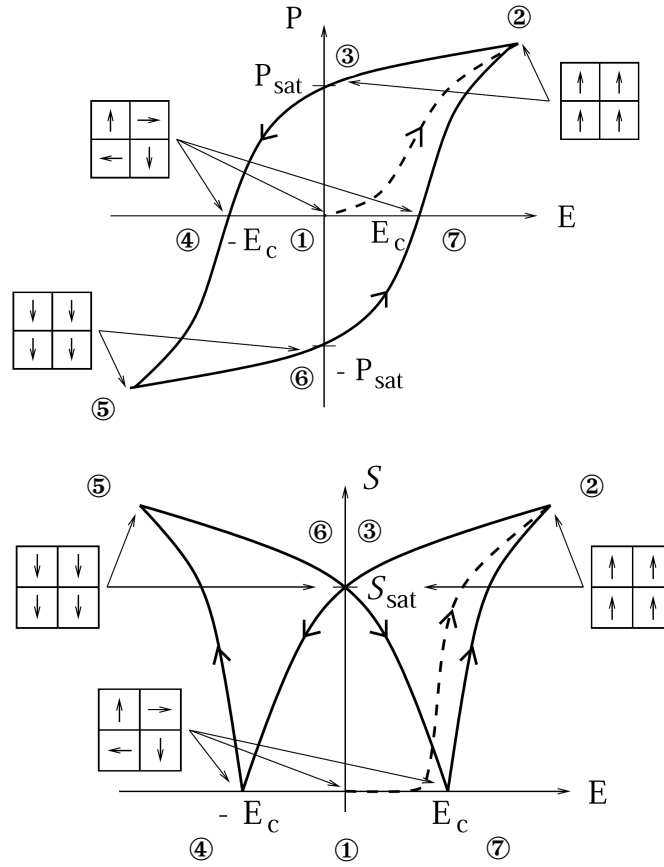


Figure 2.4: Uniaxial electric loading yields the typical dielectric and strain hystereses. The states of completely switched and randomly distributed polarization are indicated by simplified domain state symbols. Reprinted from KAMLAH (2001).

this highest achievable value is referred to as the *saturation polarization*. Reversal of the electric field leads to switching of polarization in the opposite direction. The coercive field is reached at ④ when the net polarization vanishes. Domain switching continues to ⑤, where the material is fully poled in the opposite direction. By reversing the electric field once more, the points ⑥, ⑦, and ② are passed in an analogous way. These characteristic points are also observed in the strain hysteresis plotted in Fig. 2.4. In the initial poling process, there is no piezoelectric strain until domain switching is triggered and the material becomes macroscopically piezoelectric. When the fully poled state is reached at ②, the strain increases only due to the inverse piezoelectric effect. The *saturation strain* is then reached at point ③. The strain vanishes when the coercive field is reached and increases again as poling in the other direction takes place.

The response for a mechanical depolarization experiment is shown in Fig. 2.5.

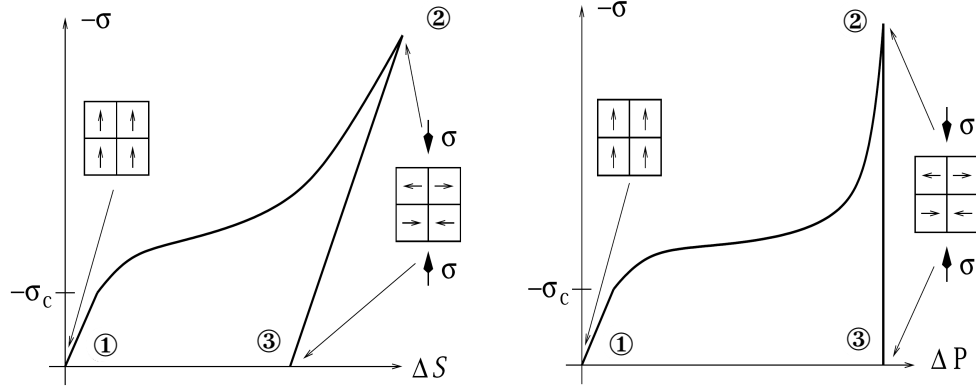


Figure 2.5: Strain and polarization changes relative to the poled initial state under mechanical compression. Again, simplifying symbols are used to visualize overall domain distributions. Reprinted from KAMLAH (2001).

Since the initial poling state may not be known, only changes in strain and polarization relative to this initial state are given in the diagrams. The initial linear response of the poled material at ① is due to linear elasticity and the piezoelectric effect. When the *coercive stress* is passed, the switching of polarization accelerates the depolarization process until the macroscopically unpolarized state is reached at ②. Increasing the compressive stress beyond this point gives a linear elastic response but no further change in polarization; the same is true when the stress loading is reduced to zero at the point ③.

The macroscopic behavior of ferroelectric ceramics is time and rate dependent, see e.g. ZHOU (2003). The switching of polarization introduces an internal time scale, which leads to variations in the hystereses curves when the external loading frequency is changed. Explicit time dependency is observed in ageing and fatigue effects, see LUPASCU (2004) for a detailed discussion.



# Chapter 3

## Basic equations

### 3.1 Motion and deformation

There are many textbooks on the subject of classical continuum mechanics (e.g. GURTIN 1981, OGDEN 1984, HOLZAPFEL 2000). In order to achieve a consistent notation, the following review is based on the (rather formal) approaches given in HAUPT (2000) and TSAKMAKIS (1998).

In continuum mechanics, a material body  $\mathfrak{B}$  which consists of material points  $\chi$ , is represented by a region  $\mathcal{B}$  in the three-dimensional Euclidean point space  $\mathcal{E}$ . A material point  $\chi \in \mathfrak{B}$  is identified with its position  $x \in \mathcal{E}$  or, equivalently, with its position vector  $\mathbf{x}$  in the three-dimensional Euclidean vector space  $\mathbb{E}$ . Mathematically this is expressed by the mapping<sup>1</sup>

$$\begin{aligned}\chi &: \mathfrak{B} \rightarrow \mathbb{E} \\ \chi &\mapsto \mathbf{x} = \chi(\chi)\end{aligned}\tag{3.1}$$

which is referred to as *configuration*<sup>2</sup>. The motion of a material body is described by a family of configurations parametrized with time  $t$ :

$$\chi_t(\chi) \equiv \chi(\chi, t) .\tag{3.2}$$

The configuration defined by  $\chi_t(\chi)$  or, equivalently, the region  $\mathcal{B}$  occupied by the body, is called *current configuration*. It is convenient to define a fixed reference configuration  $\chi_0$  by

$$\mathbf{X} = \chi_0(\chi)\tag{3.3}$$

---

<sup>1</sup>This mapping is assumed to be invertible and sufficiently continuously differentiable, cf. Sec. 3.3.

<sup>2</sup>The region in  $\mathcal{E}$  which is defined by the image of  $\chi(\mathfrak{B})$  is also commonly called configuration.

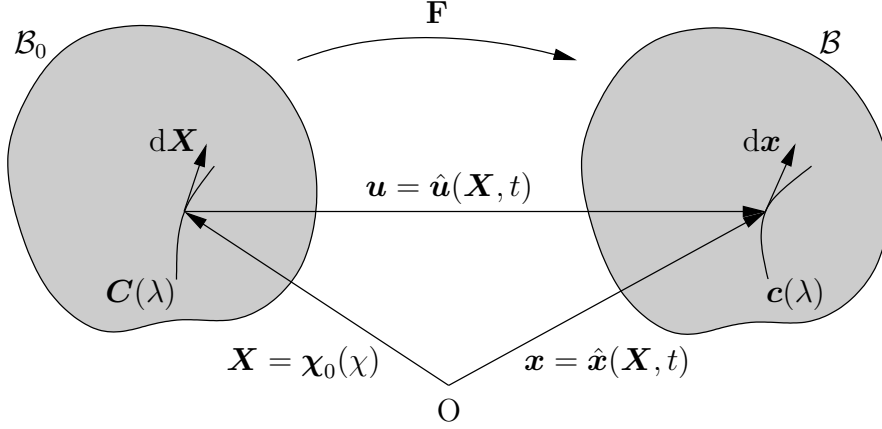


Figure 3.1: Motion and deformation of a body. The deformation gradient  $\mathbf{F}$  maps material line elements  $d\mathbf{X}$  in the reference configuration to material line elements  $d\mathbf{x}$  in the current configuration.

in which the body occupies the region  $\mathcal{B}_0$ . As illustrated in Fig. 3.1, the motion of the body can then be described by

$$\mathbf{x} = \hat{\mathbf{x}}(\mathbf{X}, t) . \quad (3.4)$$

Additionally the set  $\mathbb{E}_0$  is defined by  $\mathbb{E}_0 = \{\mathbf{X} : \mathbf{X} = \chi_0(\chi), \chi \in \mathfrak{B}\}$ .<sup>3</sup>

The deformation at a point  $\mathbf{X}$  is characterized by the *deformation gradient*. Considering a point  $\mathbf{Y}$  in the vicinity of  $\mathbf{X}$  and their respective positions  $\mathbf{y}$  and  $\mathbf{x}$  in the current configuration, one can establish the Taylor expansion of  $\mathbf{y}$  around  $\mathbf{x}$  for fixed time  $t$ :

$$\mathbf{y} - \mathbf{x} = \frac{\partial \hat{\mathbf{x}}(\mathbf{X}, t)}{\partial \mathbf{X}} [\mathbf{Y} - \mathbf{X}] + \dots . \quad (3.5)$$

Thus the deformation gradient

$$\mathbf{F}(\mathbf{X}, t) = \frac{\partial \hat{\mathbf{x}}(\mathbf{X}, t)}{\partial \mathbf{X}} , \quad (3.6)$$

which is the tangential of the point mapping  $\hat{\mathbf{x}}(\mathbf{X}, t)$ , describes the deformation at a point  $\mathbf{X}$ . Taking the differential of (3.4) for fixed  $t$ , one obtains

$$d\mathbf{x} = \frac{\partial \hat{\mathbf{x}}(\mathbf{X}, t)}{\partial \mathbf{X}} d\mathbf{X} = \mathbf{F}(\mathbf{X}, t) d\mathbf{X} , \quad (3.7)$$

i.e.  $\mathbf{F}(\mathbf{X}, t)$  maps material line elements  $d\mathbf{X}$  in  $\mathcal{B}_0$  to material line elements  $d\mathbf{x}$  in  $\mathcal{B}$

---

<sup>3</sup>Generally, physical field quantities of  $\mathfrak{B}$  can be described in terms of  $\chi$  (material description),  $\mathbf{X}$  (Lagrangian description), or  $\mathbf{x}$  (spatial or Eulerian description).

as illustrated in Fig. 3.1.<sup>4</sup> It can be shown<sup>5</sup> that there exists a unique multiplicative decomposition of  $\mathbf{F}$  such that

$$\mathbf{F} = \mathbf{R}\mathbf{U} = \mathbf{V}\mathbf{R} , \quad (3.8)$$

where  $\mathbf{R}$  is a proper orthogonal second-order tensor describing a local rotation of  $d\mathbf{X}$ , and  $\mathbf{U}$  and  $\mathbf{V}$  are the symmetric positive definite *right* and *left stretch tensor*, respectively, which capture the local stretch of  $d\mathbf{X}$ .<sup>6</sup>

The material is considered unstrained if the length of  $d\mathbf{X}$  is unchanged under the deformation. Therefore the difference  $\Delta = |d\mathbf{x}|^2 - |d\mathbf{X}|^2$  is a measure of strain at the point  $\mathbf{X}$ . Making use of Eq. (3.6), one obtains

$$\Delta = d\mathbf{X} \cdot [(\mathbf{F}^T \mathbf{F} - \mathbf{1}) d\mathbf{X}] . \quad (3.9)$$

This gives rise to the definition of the *Green* or *Lagrangian strain tensor*<sup>7</sup>

$$\mathbf{G} = \frac{1}{2} (\mathbf{F}^T \mathbf{F} - \mathbf{1}) = \frac{1}{2} (\mathbf{U}^2 - \mathbf{1}) , \quad (3.10)$$

which implies that  $\Delta = d\mathbf{X} \cdot (2\mathbf{G} d\mathbf{X})$ .

The velocity of a material point is given by the material time derivative of the current configuration:

$$\mathbf{v} = \dot{\mathbf{x}}(t) = \frac{d}{dt} \mathbf{x}_t = \frac{\partial}{\partial t} \hat{\mathbf{x}}(\mathbf{X}, t) = \hat{\mathbf{v}}(\mathbf{X}, t) = \bar{\mathbf{v}}(\mathbf{x}, t) . \quad (3.11)$$

The *spatial velocity gradient* is defined by

$$\mathbf{L} = \frac{\partial}{\partial \mathbf{x}} \bar{\mathbf{v}}(\mathbf{x}, t) = \dot{\mathbf{F}} \mathbf{F}^{-1} \quad (3.12)$$

and has the properties

$$(d\mathbf{x})^\cdot = \mathbf{L} d\mathbf{x} , \quad (d\mathbf{a})^\cdot = [(\operatorname{div} \mathbf{v}) \mathbf{1} - \mathbf{L}^T] d\mathbf{a} , \quad (dv)^\cdot = (\operatorname{tr} \mathbf{L}) dv , \quad (3.13)$$

---

<sup>4</sup>The term *material line element* becomes clear in light of the following geometrical interpretation. Let  $\mathbf{C}(\lambda)$  and  $\mathbf{c}(\lambda)$  be material lines parametrized with  $\lambda$  in the reference and current configuration, respectively. With  $\mathbf{X} = \mathbf{C}(\lambda_0)$  and  $\mathbf{x} = \mathbf{c}(\lambda_0)$ ,  $d\mathbf{X} = \frac{d\mathbf{C}(\lambda_0)}{d\lambda} d\lambda$  and  $d\mathbf{x} = \frac{d\mathbf{c}(\lambda_0)}{d\lambda} d\lambda$ .

<sup>5</sup>See e.g. OGDEN (1984, Ch. 2).

<sup>6</sup>Strictly speaking, Eq. (3.8) should be written as  $\mathbf{F}(\mathbf{X}, t) = \mathbf{R}(\mathbf{X}, t)\mathbf{U}(\mathbf{X}, t)$ . In the following, the arguments  $\mathbf{X}$  and  $t$  are omitted to avoid congestion.

<sup>7</sup>The factor  $\frac{1}{2}$  stems from a more general definition of strain tensors by which the Lagrangian tensors  $\frac{1}{m}(\mathbf{U}^m - \mathbf{1})$  for integer  $m \neq 0$  and  $\ln \mathbf{U}$  for  $m = 0$  are used as measures of strain, cf. OGDEN (1984, Ch. 2).

where  $d\mathbf{a} = d\mathbf{x}_1 \times d\mathbf{x}_2$  and  $dv = (d\mathbf{x}_1 \times d\mathbf{x}_2) \cdot d\mathbf{x}_3$  are material volume and surface elements in the current configuration, respectively.

As shown in Fig. 3.1, the displacement  $\mathbf{u}$  of a material point is defined by

$$\mathbf{u} = \hat{\mathbf{u}}(\mathbf{X}, t) = \hat{\mathbf{x}}(\mathbf{X}, t) - \mathbf{X} = \mathbf{x} - \mathbf{X} , \quad (3.14)$$

and its gradient, the *displacement gradient*, is defined by

$$\mathbf{H} = \frac{\partial \hat{\mathbf{u}}(\mathbf{X}, t)}{\partial \mathbf{X}} = \mathbf{F} - \mathbf{1} . \quad (3.15)$$

The material body is said to undergo small deformations if

$$z(t) = \sup_{\substack{\mathbf{X} \in \mathbb{E}_0 \\ \tilde{t} \in \{\tilde{t}: \tilde{t} \leq t\}}} \|\mathbf{H}(\mathbf{X}, \tilde{t})\| \ll 1 \quad \text{and} \quad \frac{\hat{\mathbf{u}}(\mathbf{X}, t)}{\ell_0} \ll 1 \quad (3.16)$$

holds throughout its motion, whereat  $\ell_0$  represents a characteristic length of the body. The following asymptotic relations, stated in terms of the displacement gradient, are obtained for small deformations:

$$\mathbf{F} = \mathbf{1} + \mathbf{H} = \mathbf{1} + \mathcal{O}(z) , \quad (3.17)$$

$$\mathbf{F}^{-1} = \mathbf{1} - \mathbf{H} + \mathcal{O}(z^2) , \quad (3.18)$$

$$\det \mathbf{F} = 1 + \text{tr} \mathbf{H} + \mathcal{O}(z^2) , \quad (3.19)$$

$$\mathbf{R} = \mathbf{1} + \frac{1}{2} (\mathbf{H} - \mathbf{H}^T) + \mathcal{O}(z^2) , \quad (3.20)$$

$$\mathbf{U} = \mathbf{1} + \frac{1}{2} (\mathbf{H} + \mathbf{H}^T) + \mathcal{O}(z^2) , \quad (3.21)$$

$$\mathbf{V} = \mathbf{1} + \frac{1}{2} (\mathbf{H} + \mathbf{H}^T) + \mathcal{O}(z^2) , \quad (3.22)$$

$$\mathbf{G} = \frac{1}{2} (\mathbf{H} + \mathbf{H}^T) + \mathcal{O}(z^2) , \quad (3.23)$$

$$\mathbf{L} = \dot{\mathbf{H}} + \mathcal{O}(z^2) . \quad (3.24)$$

For the linearization of  $\mathbf{L}$ , small deformation rates have to be assumed, i.e. Eq. (3.16)<sub>1</sub> has to be valid for  $\dot{\mathbf{H}}$  as well. The relation

$$\mathbf{F} = \mathbf{R}\mathbf{U} = \mathbf{1} + \frac{1}{2} (\mathbf{H} - \mathbf{H}^T) + \frac{1}{2} (\mathbf{H} + \mathbf{H}^T) + \mathcal{O}(z^2) \quad (3.25)$$

shows that the polar decomposition can be expressed in terms of the antisymmetric and the symmetric part of  $\mathbf{H}$ . The latter, having already appeared in Eqs. (3.21)–(3.23), is the *linearized strain tensor*

$$\boldsymbol{\varepsilon} = \frac{1}{2} (\mathbf{H} + \mathbf{H}^T) . \quad (3.26)$$

## 3.2 Electrostatics

In this work, electrostatic conditions are assumed *a priori*; magnetic or electrodynamic effects due to moving charges are not considered. Textbooks on classical electrostatics and -dynamics include LANDAU & LIFSHITZ (1980), LANDAU & LIFSHITZ (1984), PURCELL (1965), and JACKSON (1999); a brief summary can be found in MEHLING (2007). The following summarization closely follows FLIESSBACH (2008), who presents these topics from a theoretical physicist's perspective.

### Electric charge

Electric charge is a property of elementary particles. It is quantized in the sense that it can only take values of integer multiples of the elementary charge  $e \approx 1.60217646 \cdot 10^{-19}$  C which is the charge of the positron. Since charge<sup>8</sup> is an additive quantity,  $N$  particles with individual charges  $q_i$  have the net charge

$$q = \sum_{i=1}^N q_i . \quad (3.27)$$

Within a continuum description, discrete charges  $q_i$  are replaced by a charge density. The microscopic charge density  $\rho_{\text{mic}}$  of  $N$  point charges can be expressed with the Dirac delta distribution by

$$\rho_{\text{mic}}(\mathbf{x}) = \sum_{i=1}^N q_i \delta(\mathbf{x} - \mathbf{x}_i) , \quad (3.28)$$

where  $\mathbf{x}_i$  is the position vector of the charge  $q_i$ . A continuous and bounded charge density  $\rho$  can be defined by means of volume averages of Eq. (3.28) over a representative volume  $V^{\text{R}}$  as sketched in Fig. 3.2. The averaging procedure yields

$$\rho(\mathbf{x}) = \frac{1}{V^{\text{R}}} \int_{V^{\text{R}}} \rho_{\text{mic}}(\bar{\mathbf{x}}) d\bar{v} = \frac{1}{V^{\text{R}}} \sum_{i=1}^N q_i . \quad (3.29)$$

The surface charge density  $\omega$  is defined analogously for a representative surface area  $A^{\text{R}}$  containing  $N_{\text{s}}$  charges:

$$\omega(\mathbf{x}) = \frac{1}{A^{\text{R}}} \int_{\partial V^{\text{R}}} \rho_{\text{mic}}(\bar{\mathbf{x}}) d\bar{a} = \frac{1}{A^{\text{R}}} \sum_{i=1}^{N_{\text{s}}} q_i . \quad (3.30)$$

---

<sup>8</sup>Charge is a more general notion in physics and applies not only to electric charge. For the sake of brevity, charge and electric charge are used synonymously in this work.

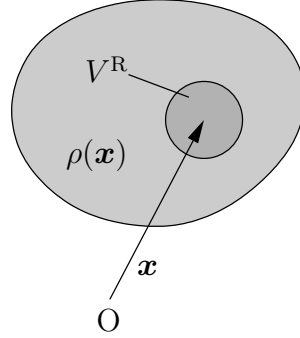


Figure 3.2: The charge density is defined as an average of microscopic point charges in a representative volume element around the point  $\mathbf{x}$ .

### Coulomb's law

Point charges interact with each other via the electrostatic force. The force exerted by a charge  $q_1$  on another charge  $q_2$  (Fig. 3.3 a) is given by

$$\mathbf{F}_{12} = \frac{q_1 q_2}{4\pi\epsilon_0} \frac{\mathbf{x}_2 - \mathbf{x}_1}{|\mathbf{x}_2 - \mathbf{x}_1|^3} . \quad (3.31)$$

The constant  $\epsilon_0 \approx 8.854 \cdot 10^{-12} \text{ C}/(\text{Vm})$  is called *electric constant*. The electrostatic force obeys the *actio = reactio* principle in that  $\mathbf{F}_{12} = -\mathbf{F}_{21}$ .

The force exerted by  $N$  charges with position vectors  $\mathbf{x}_i$  on a test charge  $q_0$  located at position  $\mathbf{x}$  (Fig. 3.3 b) is given by

$$\mathbf{F}_0(\mathbf{x}) = \sum_{i=1}^N \frac{q_i q_0}{4\pi\epsilon_0} \frac{\mathbf{x} - \mathbf{x}_i}{|\mathbf{x} - \mathbf{x}_i|^3} . \quad (3.32)$$

If the system of point charges is replaced with a charge density  $\rho$  (see Fig. 3.3 c), the force exerted on a test charge  $q_0$  is given by

$$\mathbf{F}_0(\mathbf{x}) = q_0 \int_V \frac{\rho}{4\pi\epsilon_0} \frac{\mathbf{x} - \bar{\mathbf{x}}}{|\mathbf{x} - \bar{\mathbf{x}}|^3} d\bar{v} . \quad (3.33)$$

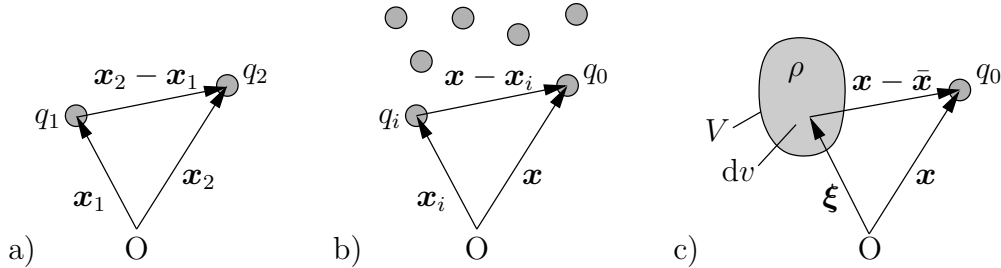


Figure 3.3: Coulomb's law is formulated for point charges and charge densities.

Equations (3.32) and (3.33) give rise to the definition of the *electric field strength*<sup>9</sup>  $\mathbf{E}$  which is defined as the ratio of  $\mathbf{F}_0/q_0$ :

$$\mathbf{E}(\mathbf{x}) = \sum_{i=1}^N \frac{q_i}{4\pi\epsilon_0} \frac{\mathbf{x} - \mathbf{x}_i}{|\mathbf{x} - \mathbf{x}_i|^3} \quad \text{and} \quad \mathbf{E}(\mathbf{x}) = \int_V \frac{\rho}{4\pi\epsilon_0} \frac{\mathbf{x} - \bar{\mathbf{x}}}{|\mathbf{x} - \bar{\mathbf{x}}|^3} d\bar{v} . \quad (3.34)$$

### Work and electric potential

The work required to move a test charge  $q_0$  from an arbitrary point  $A$  with position vector  $\mathbf{x}_A$  to another arbitrary point  $B$  with position vector  $\mathbf{x}_B$  along an arbitrary<sup>10</sup> path  $\Gamma$  is given by

$$W_A^B = - \int_{\Gamma} \mathbf{F}_0 \cdot d\mathbf{s} = -q_0 \int_{\Gamma} \mathbf{E} \cdot d\mathbf{s} . \quad (3.35)$$

It can be shown<sup>11</sup> that the electric field (3.34)<sub>2</sub> is a conservative vector field<sup>12</sup>, which implies that the integrals in Eq. (3.35) are path independent and that there exists a scalar potential  $\varphi(\mathbf{x})$  so that Eq. (3.35) can be written as

$$W_A^B = q_0 (\varphi(\mathbf{x}_B) - \varphi(\mathbf{x}_A)) . \quad (3.36)$$

It also follows that the electric field is the negative gradient of  $\varphi$ :

$$\mathbf{E}(\mathbf{x}) = -\text{grad } \varphi(\mathbf{x}) . \quad (3.37)$$

The scalar field  $\varphi$  is called *electric potential* and is unique up to a constant which is often set to zero.

The electric potential for the system of point charges and the charge distributions in Figs. 3.3 b) and c) are given by

$$\varphi(\mathbf{x}) = \sum_{i=1}^N \frac{q_i}{4\pi\epsilon_0 |\mathbf{x} - \mathbf{x}_i|} \quad \text{and} \quad \varphi(\mathbf{x}) = \int_V \frac{\rho(\bar{\mathbf{x}})}{4\pi\epsilon_0 |\mathbf{x} - \bar{\mathbf{x}}|} d\bar{v} , \quad (3.38)$$

respectively. Inserting Eq. (3.38)<sub>2</sub> in (3.37), multiplying with  $-\epsilon_0$ , and taking the divergence, one obtains

$$\epsilon_0 \Delta \varphi(\mathbf{x}) = \int_V \rho(\bar{\mathbf{x}}) \Delta \frac{1}{4\pi |\mathbf{x} - \bar{\mathbf{x}}|} d\bar{v} = - \int_V \rho(\bar{\mathbf{x}}) \delta(\mathbf{x} - \bar{\mathbf{x}}) d\bar{v} = -\rho(\mathbf{x}) . \quad (3.39)$$

<sup>9</sup>Or simply the *electric field*.

<sup>10</sup> $\mathbf{\Gamma}$  is assumed piecewise continuously differentiable and  $\mathbf{F}_0(\mathbf{\Gamma})$  piecewise continuous.

<sup>11</sup>See e.g. JACKSON (1999, Ch. 1).

<sup>12</sup>Cf. MARSDEN & TROMBA (2003, Ch. 8).

In terms of the electric field, Eq. (3.39) reads

$$\epsilon_0 \operatorname{div} \mathbf{E}(\mathbf{x}) = \rho(\mathbf{x}) \quad (3.40)$$

which is known as Gauss's law. It follows from Eq. (3.37) that  $\mathbf{E}$  is curl free:

$$\operatorname{curl} \mathbf{E}(\mathbf{x}) = \mathbf{0} . \quad (3.41)$$

Equations (3.40) and (3.41) or, in terms of the electric potential, (3.39) and (3.37), are the field equations of electrostatics.

The *potential energy* of the aforementioned system of point charges due to *their own* electric fields can be calculated by consecutively adding the energies required to move each point charge successively into the system from infinity. The potential energy of a continuous charge distribution is derived analogously by discretizing the charge distribution in  $N$  partial charges, each occupying a volume  $\Delta V_i$ , and, subsequently, taking the limit  $N \rightarrow \infty$  and  $\Delta V_i \rightarrow 0$ . The resulting potential energies are then given by

$$U = \frac{1}{2} \sum_{\substack{i,j=1 \\ i \neq j}}^N \frac{q_i q_j}{4\pi\epsilon_0 |\mathbf{x}_i - \mathbf{x}_j|} \quad \text{and} \quad U = \frac{1}{2} \int_V \int_V \frac{\rho(\tilde{\mathbf{x}})\rho(\bar{\mathbf{x}})}{4\pi\epsilon_0 |\tilde{\mathbf{x}} - \bar{\mathbf{x}}|} d\tilde{V} d\bar{V} . \quad (3.42)$$

With Eqs. (3.38)<sub>1</sub> and (3.38)<sub>2</sub>, this reduces to

$$U = \frac{1}{2} \sum_{i=1}^N q_i \varphi(\mathbf{x}_i) \quad \text{and} \quad U = \frac{1}{2} \int_V \varphi(\bar{\mathbf{x}}) \rho(\bar{\mathbf{x}}) d\bar{v} . \quad (3.43)$$

The potential energy of a system of point charges and a charge distribution in an *external* field  $\varphi_{\text{ext}}$ , *excluding* the fields due to the charges  $q_i$  or the charge distribution  $\rho$ , is given by

$$U = \sum_{i=1}^N q_i \varphi_{\text{ext}}(\mathbf{x}_i) \quad \text{and} \quad U = \int_V \rho(\bar{\mathbf{x}}) \varphi_{\text{ext}}(\bar{\mathbf{x}}) d\bar{v} , \quad (3.44)$$

respectively.

### Multipole expansion and electric polarization

Figure 3.4 shows a charge distribution  $\rho$  occupying a volume  $V$ . The positions in  $V$  are denoted by  $\boldsymbol{\xi}$ ;  $\mathbf{a}$  is a fixed position in  $V$ , and  $\mathbf{x}$  is a position far away from  $V$ . Furthermore, the vectors  $\mathbf{r} = \mathbf{x} - \mathbf{a} = r\mathbf{n}$  and  $\tilde{\mathbf{r}} = \mathbf{a} - \boldsymbol{\xi} = \tilde{r}\tilde{\mathbf{n}}$  are defined so



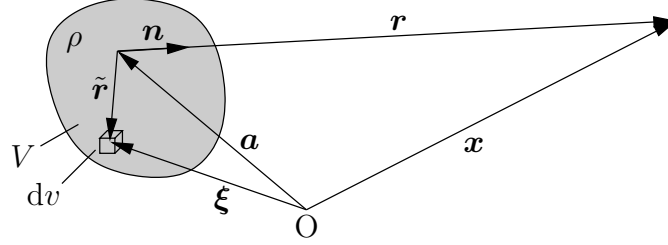


Figure 3.4: Multipole expansion.

that  $\mathbf{x} - \boldsymbol{\xi} = \mathbf{r} - \tilde{\mathbf{r}}$ . The electric potential of the charge distribution is given by Eq. (3.38)<sub>2</sub> and reads

$$\varphi(\mathbf{x}) = \int_V \frac{\rho(\tilde{\mathbf{r}})}{4\pi\epsilon_0} \frac{1}{|\mathbf{r} - \tilde{\mathbf{r}}|} d\tilde{v} = \frac{1}{4\pi\epsilon_0 r} \int_V \rho(1 + \alpha)^{-\frac{1}{2}} d\tilde{v}, \quad (3.45)$$

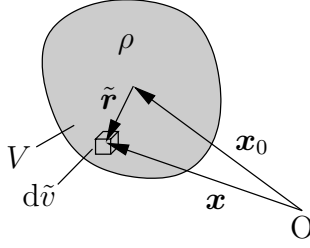
where  $\alpha := r^{-2}(\tilde{r}^2 - 2\mathbf{r} \cdot \tilde{\mathbf{r}}) \ll 1$ . The Taylor expansion of  $(1 + \alpha)^{-\frac{1}{2}}$  with respect to  $\alpha = 0$  gives  $(1 + \alpha)^{-\frac{1}{2}} = 1 - \frac{1}{2}\alpha + \frac{3}{8}\alpha^2 - \frac{5}{16}\alpha^3 + \dots$ . Substitution in Eq. (3.45) yields the multipole expansion of  $\varphi$ :

$$\begin{aligned} \varphi(\mathbf{x}) = \frac{1}{4\pi\epsilon_0} & \left[ \frac{1}{r} \int_V \rho(\tilde{\mathbf{r}}) d\tilde{v} + \frac{\mathbf{n}}{r^2} \cdot \int_V \rho(\tilde{\mathbf{r}}) \tilde{\mathbf{r}} d\tilde{v} \right. \\ & \left. + \frac{\mathbf{n} \otimes \mathbf{n}}{2r^3} \cdot \int_V \rho(\tilde{\mathbf{r}}) (3\tilde{\mathbf{r}} \otimes \tilde{\mathbf{r}} - \tilde{r}^2 \mathbf{1}) d\tilde{v} + \dots \right]. \end{aligned} \quad (3.46)$$

The integrals in (3.46) are called the *moments of the charge distribution*. The first integral is the *monopole moment* or simply the net charge  $q$  of the system, the second integral is the *dipole moment*  $\mathbf{p}$ , and the third integral is the *quadrupole moment*. Except for the net charge, the multipole moments in (3.46) generally depend on  $\mathbf{a}$ . In fact, only the first non-vanishing term of the expansion is independent of  $\mathbf{a}$ . Within this work, only charges and dipole moments are taken into account, while moments of higher order are neglected.

### Charge distribution in an external field

The charge distribution  $\rho$  sketched in Fig. 3.5 is subjected to an *external* electric field  $\mathbf{E}_{\text{ext}} = -\text{grad } \varphi_{\text{ext}}$ , i.e. the field due to the charge distribution itself is not included in  $\mathbf{E}_{\text{ext}}$ . By the assumption that  $\rho$  does not change under the external field and that  $\mathbf{E}_{\text{ext}}$  varies only slightly in  $V$ , the following Taylor expansions of  $\varphi_{\text{ext}}(\mathbf{x})$

Figure 3.5: Taylor expansion of  $\varphi_{\text{ext}}$  around  $\mathbf{x}_0$ .

and  $\mathbf{E}_{\text{ext}}(\mathbf{x})$  around the center of the distribution  $\mathbf{x}_0$  can be established:

$$\varphi_{\text{ext}}(\mathbf{x}) = \tilde{\varphi}_{\text{ext}}(\tilde{\mathbf{r}}) = \varphi_{\text{ext}}(\mathbf{x}_0) + \left. \frac{\partial \varphi_{\text{ext}}}{\partial \mathbf{x}} \right|_{\mathbf{x}_0} \cdot \tilde{\mathbf{r}} + \dots, \quad (3.47)$$

$$\mathbf{E}_{\text{ext}}(\mathbf{x}) = \tilde{\mathbf{E}}_{\text{ext}}(\tilde{\mathbf{r}}) = \mathbf{E}_{\text{ext}}(\mathbf{x}_0) + \left[ \left. \frac{\partial \mathbf{E}_{\text{ext}}}{\partial \mathbf{x}} \right|_{\mathbf{x}_0} \right]^T \tilde{\mathbf{r}} + \dots. \quad (3.48)$$

With Eqs. (3.44)<sub>2</sub> and (3.37), the potential energy of the charge distribution in the external field  $\mathbf{E}_{\text{ext}}$  is

$$\begin{aligned} U(\mathbf{x}_0) &= \int_V \rho \varphi_{\text{ext}} d\tilde{v} = \int_V \tilde{\rho}(\tilde{\mathbf{r}}) \tilde{\varphi}_{\text{ext}}(\tilde{\mathbf{r}}) d\tilde{v} \\ &= \varphi_{\text{ext}}(\mathbf{x}_0) \int_V \tilde{\rho}(\tilde{\mathbf{r}}) d\tilde{v} - \mathbf{E}_{\text{ext}}(\mathbf{x}_0) \cdot \int_V \tilde{\rho}(\tilde{\mathbf{r}}) \tilde{\mathbf{r}} d\tilde{v} + \dots \\ &= q \varphi_{\text{ext}}(\mathbf{x}_0) - \mathbf{p} \cdot \mathbf{E}_{\text{ext}}(\mathbf{x}_0) + \dots, \end{aligned} \quad (3.49)$$

where  $q$  and  $\mathbf{p}$  are the monopole and dipole moment, respectively, which were calculated in (3.46).

The resulting force acting on the charge distribution is then given by the negative gradient of  $U$  with respect to  $\mathbf{x}_0$ :

$$\begin{aligned} \mathbf{F}^e(\mathbf{x}_0) &= -\nabla_{\mathbf{x}_0} U(\mathbf{x}_0) \\ &= \mathbf{E}_{\text{ext}}(\mathbf{x}_0) \int_V \tilde{\rho}(\tilde{\mathbf{r}}) d\tilde{v} + [\nabla_{\mathbf{x}_0} \mathbf{E}_{\text{ext}}(\mathbf{x}_0)]^T \int_V \tilde{\rho}(\tilde{\mathbf{r}}) \tilde{\mathbf{r}} d\tilde{v} + \dots \\ &= q \mathbf{E}_{\text{ext}}(\mathbf{x}_0) + [\nabla_{\mathbf{x}_0} \mathbf{E}_{\text{ext}}(\mathbf{x}_0)]^T \mathbf{p} + \dots, \end{aligned} \quad (3.50)$$

and the resulting angular momentum is given by

$$\begin{aligned} \mathbf{M}^e(\mathbf{x}_0) &= \int_V (\mathbf{x}_0 + \tilde{\mathbf{r}}) \times \tilde{\mathbf{E}}_{\text{ext}}(\tilde{\mathbf{r}}) \tilde{\rho}(\tilde{\mathbf{r}}) d\tilde{v} \\ &= \mathbf{x}_0 \times \left( \mathbf{E}_{\text{ext}}(\mathbf{x}_0) \int_V \tilde{\rho}(\tilde{\mathbf{r}}) d\tilde{v} + [\nabla_{\mathbf{x}_0} \mathbf{E}_{\text{ext}}(\mathbf{x}_0)]^T \int_V \tilde{\rho}(\tilde{\mathbf{r}}) \tilde{\mathbf{r}} d\tilde{v} \right) \\ &\quad + \int_V \tilde{\rho}(\tilde{\mathbf{r}}) \tilde{\mathbf{r}} d\tilde{v} \times \mathbf{E}_{\text{ext}}(\mathbf{x}_0) + \dots \\ &= \mathbf{x}_0 \times \mathbf{F}^e(\mathbf{x}_0) + \mathbf{p} \times \mathbf{E}_{\text{ext}}(\mathbf{x}_0) + \dots. \end{aligned} \quad (3.51)$$

### Electrostatics in matter

Up to now, this section was concerned with systems of point charges and charge densities in a vacuum. However, the electrostatic field equations (3.40) and (3.41) are also valid in matter. On the microscopic scale, the total charge density  $\rho_{\text{tot}}$  and the associated electric field  $\mathbf{E}_{\text{tot}}$  can be split additively in the fields of the undisturbed matter (index “0”), *extra* fields (index “ext”), and the *induced* fields (index “ind”):

$$\rho_{\text{tot}} = \rho_0 + \rho_{\text{ext}} + \rho_{\text{ind}} , \quad (3.52)$$

$$\mathbf{E}_{\text{tot}} = \mathbf{E}_0 + \mathbf{E}_{\text{ext}} + \mathbf{E}_{\text{ind}} . \quad (3.53)$$

From another point of view, one can distinguish between *free* and *bound* charges. Free charges can move through the material and contribute to an electric current when an external electric field is present, whereas bound charges can only move to a limited extent and remain fixed to the material in the presence of an external field. With a change in notation, the following decomposition is chosen:

$$\rho_{\text{tot}} = \rho_0 + \rho^{\text{free}} + \rho_{\text{ind}}^{\text{bound}} =: \rho_0 + \rho , \quad (3.54)$$

$$\mathbf{E}_{\text{tot}} = \mathbf{E}_0 + \mathbf{E}^{\text{free}} + \mathbf{E}_{\text{ind}}^{\text{bound}} =: \mathbf{E}_0 + \mathbf{E} , \quad (3.55)$$

where  $\rho^{\text{free}}$  includes the extra charges in (3.52) and free induced charges. Then the electrostatic field equations (3.40) and (3.41) become

$$\epsilon_0 \operatorname{div}(\mathbf{E}_0 + \mathbf{E}) = \rho_0 + \rho \quad \text{and} \quad \operatorname{curl}(\mathbf{E}_0 + \mathbf{E}) = \mathbf{0} . \quad (3.56)$$

Since these field equations are linear, one obtains

$$\epsilon_0 \operatorname{div} \mathbf{E} = \rho \quad \text{and} \quad \operatorname{curl} \mathbf{E} = \mathbf{0} . \quad (3.57)$$

These are the *microscopic* electrostatic field equations.

While extra charges are assumed to be macroscopic, induced charges vary strongly on the length scale of an elementary cell. Within a continuum description, the microscopic electrostatic field equations are replaced with the *macroscopic* electrostatic field equations. The latter are obtained by means of a spatial average procedure which has the form of a convolution. The spatial average of a field  $A(\mathbf{x}, t)$  with respect to a test function  $f$  is expressed by

$$\langle A \rangle(\mathbf{x}, t) = \int_V A(\bar{\mathbf{x}}, t) f(\mathbf{x} - \bar{\mathbf{x}}) d\bar{V} \quad \text{with} \quad \int_V f(\mathbf{x} - \bar{\mathbf{x}}) d\bar{V} = 1 . \quad (3.58)$$

With the decomposition  $\rho = \rho^{\text{free}} + \rho_{\text{ind}}^{\text{bound}}$ , the averaged microscopic electrostatic field equations read

$$\epsilon_0 \operatorname{div} \langle \mathbf{E} \rangle = \langle \rho^{\text{free}} \rangle + \langle \rho_{\text{ind}}^{\text{bound}} \rangle \quad \text{and} \quad \operatorname{curl} \langle \mathbf{E} \rangle = \mathbf{0} , \quad (3.59)$$

where the identities  $\langle \operatorname{div} A \rangle = \operatorname{div} \langle A \rangle$  and  $\langle \operatorname{curl} A \rangle = \operatorname{curl} \langle A \rangle$  were used. The induced charge  $\rho_{\text{ind}}^{\text{bound}}$  is due to a shifting of charges within a neutral microscopic unit, in our case a unit cell. If the material is made of different unit cells,  $\rho_{\text{ind}}^{\text{bound}}$  is represented by the sum of the charge changes  $\Delta\rho_i$ :

$$\rho_{\text{ind}}^{\text{bound}}(\mathbf{x}, t) = \sum_i \Delta\rho_i(\mathbf{x} - \mathbf{x}_i, t) , \quad (3.60)$$

where  $\mathbf{x}_i$  is the center of the  $i$ -th unit cell. Since the net charge remains unchanged, the average of the induced charge yields

$$\begin{aligned} \langle \rho_{\text{ind}}^{\text{bound}} \rangle(\mathbf{x}, t) &= \sum_i \int_V \Delta\rho_i(\tilde{\mathbf{x}} - \mathbf{x}_i, t) f(\mathbf{x} - \tilde{\mathbf{x}}) d\tilde{V} \\ &= \sum_i f(\mathbf{x} - \mathbf{x}_i) \underbrace{\int_V \Delta\rho_i(\tilde{\mathbf{x}}, t) d\tilde{V}}_{=0} \\ &\quad - \sum_i \operatorname{grad} f(\mathbf{x} - \mathbf{x}_i) \cdot \underbrace{\int_V \tilde{\mathbf{x}} \Delta\rho_i(\tilde{\mathbf{x}}, t) d\tilde{V}}_{=\mathbf{p}_i} + \dots \end{aligned} \quad (3.61)$$

In Eq. (3.61), the function  $f(\mathbf{x} - \mathbf{x}_i - \tilde{\mathbf{x}})$  with  $\tilde{\mathbf{x}} = \tilde{\mathbf{x}} - \mathbf{x}_i$  was expanded in a Taylor series with respect to  $\tilde{\mathbf{x}}$ . The last integral in (3.61) is identified with the dipole moment of the unit cells over which the average procedure was carried out. Neglecting higher-order multipole moments, one obtains

$$\begin{aligned} \langle \rho_{\text{ind}}^{\text{bound}} \rangle(\mathbf{x}, t) &= -\operatorname{div} \left( \sum_i \mathbf{p}_i(t) f(\mathbf{x} - \mathbf{x}_i) \right) \\ &= -\operatorname{div} \left\langle \sum_i \mathbf{p}_i \delta(\tilde{\mathbf{x}} - \mathbf{x}_i) \right\rangle(\mathbf{x}, t) . \end{aligned} \quad (3.62)$$

The volume average of the dipole moments  $\mathbf{p}_i$  is the *material polarization*

$$\mathbf{P}^{\text{mat}}(\mathbf{x}, t) = \left\langle \sum_i \mathbf{p}_i \delta(\tilde{\mathbf{x}} - \mathbf{x}_i) \right\rangle(\mathbf{x}, t) . \quad (3.63)$$

It follows from Eq. (3.62) that

$$\operatorname{div} \mathbf{P}^{\text{mat}} = -\langle \rho_{\text{ind}}^{\text{bound}} \rangle . \quad (3.64)$$

Inserting Eq. (3.64) in (3.59) gives

$$\operatorname{div} (\langle \epsilon_0 \mathbf{E} \rangle + \mathbf{P}^{\text{mat}}) = \langle \rho^{\text{free}} \rangle . \quad (3.65)$$

With the definition of the *electric displacement*

$$\mathbf{D} = \langle \epsilon_0 \mathbf{E} \rangle + \mathbf{P}^{\text{mat}} \quad (3.66)$$

and the simplified notation  $\mathbf{E} := \langle \mathbf{E} \rangle$  and  $\rho := \langle \rho^{\text{free}} \rangle$ , Eq. (3.59) yields the *macroscopic* electrostatic field equations,

$$\operatorname{div} \mathbf{D} = \rho \quad \text{and} \quad \operatorname{curl} \mathbf{E} = \mathbf{0} . \quad (3.67)$$

At the boundary of a material body, the dielectric displacement exhibits a jump in the normal direction equal to the density of free surface charges:

$$[[\mathbf{D}]] \cdot \mathbf{n} = \omega , \quad (3.68)$$

where  $\mathbf{n}$  denotes the outer unit normal to  $\partial \mathcal{B}$ . The definition of the jump operator  $[[\cdot]]$  in Sec. 3.3 applies to the boundary of the body in an analogous way.

### 3.3 Discontinuities

The previous sections dealt with quantities which were assumed to be continuous within the region  $\mathcal{B}$ . In this section, the body is assumed to be divided into two parts,  $\mathcal{B}^+$  and  $\mathcal{B}^-$ , by an immaterial singular surface  $\mathcal{S}(t)$ , across which some given quantity  $\Lambda(\mathbf{x}, t)$  is allowed to be discontinuous, see Fig. 3.6. With reference to WILMANSKI (2008, Ch. 3), the singular surface can be described in the reference and current configuration by the implicit representations

$$\Sigma(\mathbf{X}, t) = 0 \quad \text{and} \quad \sigma(\mathbf{x}, t) = 0 , \quad (3.69)$$

respectively, so that  $\Sigma(\mathbf{X}, t) = \sigma(\hat{\mathbf{x}}(\mathbf{X}, t), t)$ . Equivalently, a Gaussian parametrization can be used, i.e.

$$\mathbf{X} = \tilde{\mathbf{X}}(\Xi^1, \Xi^2, t) \quad \text{and} \quad \mathbf{x} = \tilde{\mathbf{x}}(\xi^1, \xi^2, t) . \quad (3.70)$$

The unit normal vectors on the surface are defined by

$$\mathbf{N}_S(\mathbf{X}, t) = \frac{\operatorname{Grad} \Sigma}{|\operatorname{Grad} \Sigma|} \quad \text{and} \quad \mathbf{n}_S(\mathbf{x}, t) = \frac{\operatorname{grad} \sigma}{|\operatorname{grad} \sigma|} , \quad (3.71)$$

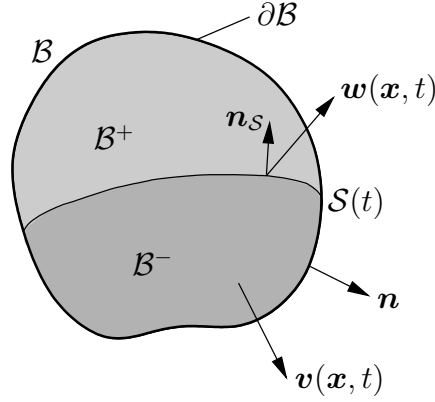


Figure 3.6: The material body  $\mathcal{B}$  with boundary  $\partial\mathcal{B}$  and outer surface normal  $\mathbf{n}$  is separated into  $\mathcal{B}^+$  and  $\mathcal{B}^-$  by the moving singular surface  $\mathcal{S}(t)$  with surface normal  $\mathbf{n}_S$  pointing from  $(-)$  to  $(+)$ . Surface points move with the velocity  $\mathbf{w}(\mathbf{x}, t)$ ; the material velocity is denoted by  $\mathbf{v}(\mathbf{x}, t)$ .

and the tangential vectors of the surface are

$$\mathbf{T}_A = \frac{\partial \check{\mathbf{X}}(\Xi^1, \Xi^2, t)}{\partial \Xi^A} \quad \text{and} \quad \mathbf{t}_\alpha = \frac{\partial \check{\mathbf{x}}(\xi^1, \xi^2, t)}{\partial \xi^\alpha} \quad (3.72)$$

for  $A = 1, 2$  and  $\alpha = 1, 2$ .

The velocity of points on  $\mathcal{S}$  is denoted by  $\mathbf{w}(\mathbf{x}, t)$ . In principle,  $\mathcal{S}$  is allowed to move through the material independently of the material velocity  $\mathbf{v}$ . The normal speeds of the interface are defined by

$$W_N = -\frac{\partial \Sigma}{\partial t} |\text{Grad } \Sigma|^{-1} \quad \text{and} \quad w_n = -\frac{\partial \sigma}{\partial t} |\text{grad } \sigma|^{-1}, \quad (3.73)$$

where  $W_N$  is the *speed of propagation* in the reference configuration and  $w_n$  is the *speed of displacement* in the current configuration. The velocities  $\mathbf{W}$  and  $\mathbf{w}$  can be formulated in terms of their normal and tangential components by

$$\mathbf{W} = W_N \mathbf{N}_S + W^A \frac{\mathbf{T}_A}{|\mathbf{T}_A|} \quad \text{and} \quad \mathbf{w} = w_n \mathbf{n}_S + w^\alpha \frac{\mathbf{t}_\alpha}{|\mathbf{t}_\alpha|} \quad (3.74)$$

with summation over  $A$  and  $\alpha$ . The tangential velocity  $w_{\text{tan}}$  is then given by

$$w_{\text{tan}} = \left| \sum_{\alpha=1}^2 w^\alpha \frac{\mathbf{t}_\alpha}{|\mathbf{t}_\alpha|} \right|. \quad (3.75)$$

The jump of a quantity  $\Lambda$  at a point  $\mathbf{x} \in \mathcal{S}(t)$ , denoted by  $[[\Lambda]](\mathbf{x}, t)$ , is defined as

$$[[\Lambda]] = \Lambda^+ - \Lambda^- \quad (3.76)$$

with

$$\Lambda^{+/-}(\mathbf{x}) = \lim_{\delta \rightarrow 0} \Lambda(\mathbf{x} \pm \delta \mathbf{n}_{\mathcal{S}}) . \quad (3.77)$$

When the jump of  $\Lambda$  vanishes, the Maxwell theorem states that its gradient jump is in the normal direction, i.e.<sup>13</sup>

$$[[\Lambda]] = 0 \quad \implies \quad [[\text{grad } \Lambda]] = b \mathbf{n}_{\mathcal{S}} , \quad b = \mathbf{n}_{\mathcal{S}} \cdot [[\text{grad } \Lambda]] . \quad (3.78)$$

In the following, the displacement field and the electric potential are assumed to be continuous across  $\mathcal{S}$ , i.e.

$$[[\mathbf{u}]] = \mathbf{0} , \quad [[\varphi]] = 0 \quad \text{on } \mathcal{S} . \quad (3.79)$$

The displacement jump condition ensures a coherent interface, thereby excluding the possibility of cracks, interpenetration, and tangential sliding. A continuous electric potential can be assumed without loss of generality.<sup>14</sup>

## 3.4 Balance equations

### Transport theorems

In this section, the balance equations for the electromechanical and thermodynamical quantities are stated. The primary sources for this section are HAUPT (2000, Ch. 2–3) and WILMANSKI (2008, Ch. 4).

Generally, a balanced bulk quantity  $\Phi$  is assumed to have a volume density  $\phi$  in the current configuration:

$$\Phi(t) = \int_{\mathcal{B}} \phi(\mathbf{x}, t) \, dv = \int_{\mathcal{B}^{+/-}} \phi(\mathbf{x}, t) \, dv , \quad (3.80)$$

where  $\int_{\mathcal{B}^{+/-}} (\cdot) \, dv = \int_{\mathcal{B}^+} (\cdot) \, dv + \int_{\mathcal{B}^-} (\cdot) \, dv$ . The density  $\phi$  is assumed to be continuous except for points which belong to the discontinuity surface  $\mathcal{S}$ . The balance equation for such an additive quantity  $\Phi$  has the general form

$$\frac{d}{dt} \int_{\mathcal{B}^{+/-}} \phi(\mathbf{x}, t) \, dv = \int_{\mathcal{B}^{+/-}} (\pi + \varsigma) \, dv + \int_{\partial \mathcal{B}} \boldsymbol{\Xi} \mathbf{n} \, da + \int_{\mathcal{S}} \varpi \, da , \quad (3.81)$$

in which  $\pi(\mathbf{x}, t)$  and  $\varsigma(\mathbf{x}, t)$  are the production and the supply of  $\Phi$  in  $\mathcal{B}^{+/-}$ , respectively,  $\boldsymbol{\Xi}(\mathbf{x}, t)$  is the flux of  $\Phi$  across the boundary  $\partial \mathcal{B}$ , and  $\varpi(\mathbf{x}, t)$  is the

<sup>13</sup>Cf. WILMANSKI (2008, Ch. 2).

<sup>14</sup>See e.g. TOUPIN (1956).

production of  $\Phi$  on  $\mathcal{S}$ . This balance equation also applies for all sub-volumes. Applying Gauss's theorem and contracting the integrals in Eq. (3.81) to a point not belonging to  $\mathcal{S}$ , one obtains the local form of the general balance equation:

$$\dot{\phi} + \phi \operatorname{div} \mathbf{v} - \operatorname{div} \mathbf{\Xi} - \varsigma = \pi \quad \text{in } \mathcal{B}^{+/-} . \quad (3.82)$$

Contraction of the integrals in Eq. (3.81) to a point on the surface  $\mathcal{S}(t)$  yields the jump condition

$$[[\phi(\mathbf{v} - \mathbf{w}) \cdot \mathbf{n}_{\mathcal{S}} - \mathbf{\Xi} \mathbf{n}_{\mathcal{S}}]] = \varpi \quad \text{on } \mathcal{S} . \quad (3.83)$$

When a quantity  $\phi_{\mathcal{S}} = \check{\phi}_{\mathcal{S}}(\xi^1, \xi^2, t) = \check{\phi}_{\mathcal{S}}(\check{\mathbf{x}}(\xi^1, \xi^2, t), t)$  exclusively defined on  $\mathcal{S}$  has to be considered, Eq. (3.80) becomes

$$\Phi(t) = \int_{\mathcal{B}^{+/-}} \phi(\mathbf{x}, t) \, dv + \int_{\mathcal{S}} \check{\phi}_{\mathcal{S}}(\mathbf{x}, t) \, da . \quad (3.84)$$

The time derivative of the second integral in this equation is given by<sup>15</sup>

$$\frac{d}{dt} \int_{\mathcal{S}} \check{\phi}_{\mathcal{S}}(\mathbf{x}, t) \, da = \int_{\mathcal{S}} \left( \mathring{\phi}_{\mathcal{S}} - \phi_{\mathcal{S}} \varkappa w_n \right) \, da + \int_{\partial \mathcal{S}} \phi_{\mathcal{S}} w_{\tan} \, ds \quad (3.85)$$

where  $\varkappa$  is the trace of the curvature tensor on  $\mathcal{S}$ . The time derivative  $\mathring{\phi}_{\mathcal{S}}$  as seen by an observer moving in the normal direction of  $\mathcal{S}$  is defined by

$$\mathring{\phi}_{\mathcal{S}} = \frac{\partial \check{\phi}_{\mathcal{S}}}{\partial t} + \operatorname{grad} \check{\phi}_{\mathcal{S}} \cdot \mathbf{n}_{\mathcal{S}} w_n . \quad (3.86)$$

In the presence of such a quantity  $\phi_{\mathcal{S}}$ , the jump condition (3.83) becomes

$$[[\phi(\mathbf{v} - \mathbf{w}) \cdot \mathbf{n}_{\mathcal{S}} - \mathbf{\Xi} \mathbf{n}_{\mathcal{S}}]] + \mathring{\phi}_{\mathcal{S}} - \phi_{\mathcal{S}} \varkappa w_n = \varpi \quad \text{on } \mathcal{S} . \quad (3.87)$$

For a thorough account of the thermodynamics of interfaces, the reader is referred to GURTIN & STRUTHERS (1990), SCHMIDT (1997), and WILMANSKI (2008).

### Conservation of mass

The total mass of the body is assumed to be constant. With  $\phi = \varrho$ , the mass density, the conservation laws read<sup>16</sup>

$$\begin{aligned} \dot{\varrho} + \varrho \operatorname{div} \mathbf{v} &= 0 \quad \text{in } \mathcal{B}^{+/-} , \\ [[\varrho(\mathbf{v} - \mathbf{w})]] \cdot \mathbf{n}_{\mathcal{S}} &= 0 \quad \text{on } \mathcal{S} . \end{aligned} \quad (3.88)$$

<sup>15</sup>See SCHMIDT (1997) and WILMANSKI (2008, Ch. 4).

<sup>16</sup>Interfacial mass is not considered.



### Conservation of charge

The density of free charges  $\rho$  is balanced with the electric current  $\mathbf{I}$ , and with  $\phi = \rho$  and  $\Xi = \mathbf{I}$  one obtains

$$\begin{aligned} \dot{\rho} + \rho \operatorname{div} \mathbf{v} + \operatorname{div} \mathbf{I} &= 0 \quad \text{in } \mathcal{B}^{+/-}, \\ [[\rho(\mathbf{v} - \mathbf{w})]] \cdot \mathbf{n}_S - [[\mathbf{I}]] \cdot \mathbf{n}_S &= 0 \quad \text{on } \mathcal{S}. \end{aligned} \quad (3.89)$$

### Conservation of linear momentum

The global balance of linear momentum reads

$$\frac{d}{dt} \int_{\mathcal{B}} \varrho \mathbf{v} \, dv = \int_{\mathcal{B}} (\mathbf{f} + \mathbf{f}^e) \, dv + \int_{\partial \mathcal{B}} (\mathbf{t} + \mathbf{t}^e) \, da, \quad (3.90)$$

where  $\mathbf{f}$  and  $\mathbf{f}^e$  are the mechanical and electrical volume force, respectively, and  $\mathbf{t}$  and  $\mathbf{t}^e$  are the mechanical and electrical surface traction vector, respectively. The electrical volume force and surface traction arise from electrical fields acting on the charges in the material. It is assumed<sup>17</sup> that the electrical volume force can be derived from the *Maxwell stress tensor*  $\boldsymbol{\sigma}^M$  such that

$$\mathbf{f}^e = \operatorname{div} \boldsymbol{\sigma}^M \quad (3.91)$$

and hence

$$\mathbf{t}^e = [[\boldsymbol{\sigma}^M]] \mathbf{n}. \quad (3.92)$$

The Cauchy stress balances the total traction of a surface element, i.e.

$$\mathbf{t} + \mathbf{t}^e = -[[\boldsymbol{\sigma}]] \mathbf{n}, \quad (3.93)$$

so that, with Eq. (3.92),

$$\mathbf{t} = -[[\boldsymbol{\sigma} + \boldsymbol{\sigma}^M]] \mathbf{n}. \quad (3.94)$$

Thus the volume density of linear momentum given by  $\phi = \varrho \mathbf{v}$  is balanced with the Cauchy stress, i.e.  $\Xi = \boldsymbol{\sigma}$ , and with the mechanical and electrical volume forces. With  $\varsigma = \mathbf{f} + \mathbf{f}^e$  and on use of Eqs. (3.88)<sub>1</sub> and (3.91), the conservation laws read<sup>18</sup>

$$\begin{aligned} \varrho \dot{\mathbf{v}} - \operatorname{div} (\boldsymbol{\sigma} + \boldsymbol{\sigma}^M) - \mathbf{f} &= \mathbf{0} \quad \text{in } \mathcal{B}^{+/-}, \\ [[\varrho \mathbf{v}(\mathbf{v} - \mathbf{w}) \cdot \mathbf{n}_S - \boldsymbol{\sigma} \mathbf{n}_S]] &= \mathbf{0} \quad \text{on } \mathcal{S}. \end{aligned} \quad (3.95)$$

<sup>17</sup>See e.g. McMEEKING & LANDIS (2005).

<sup>18</sup>Interfacial momentum and surface stress are not considered.

### Conservation of angular momentum

The global balance of angular momentum has the form

$$\frac{d}{dt} \int_{\mathcal{B}} \rho \mathbf{x} \times \mathbf{v} \, dv = \int_{\mathcal{B}} (\mathbf{x} \times (\mathbf{f} + \mathbf{f}^e) + \mathbf{m}^e) \, dv + \int_{\partial \mathcal{B}} \mathbf{x} \times (\mathbf{t} + \mathbf{t}^e) \, da, \quad (3.96)$$

where  $\mathbf{m}^e$  is the *electric body couple* which is derived from the Maxwell stress by

$$\mathbf{m}^e = \text{axl} \left( 2\boldsymbol{\sigma}_{\text{skew}}^M \right), \quad \text{i.e.} \quad m_i^e = \epsilon_{ijk} \sigma_{kj}^M. \quad (3.97)$$

With  $\phi = \mathbf{x} \times (\rho \mathbf{v})$ ,  $\boldsymbol{\Xi} = \mathbf{x} \times \boldsymbol{\sigma}$ , and  $\varsigma = \mathbf{x} \times (\mathbf{f} + \mathbf{f}^e) + \mathbf{m}^e$  and the application of Eqs. (3.88)<sub>1</sub>, (3.91), and (3.95)<sub>1</sub>, the conservation law yields

$$\epsilon_{ijk} (\sigma_{kj} + \sigma_{kj}^M) = 0 \quad \implies \quad \boldsymbol{\sigma} + \boldsymbol{\sigma}^M = (\boldsymbol{\sigma} + \boldsymbol{\sigma}^M)^T, \quad (3.98)$$

which means that the total stress  $\boldsymbol{\sigma} + \boldsymbol{\sigma}^M$  is symmetric. Given the jump relation (3.95)<sub>2</sub>, the resulting condition for points on  $\mathcal{S}$  is identically fulfilled.

### Conservation of energy

The conservation of energy results from the first law of thermodynamics which states that the rate of stored internal and kinetic energy is equal to the work rate of external sources plus the heat supply. By adopting the representation given in McMEEKING & LANDIS (2005), the global form of the balance of energy is stated as

$$\begin{aligned} \frac{d}{dt} \int_{\mathcal{B}} \left( \rho e + \frac{1}{2} \rho \mathbf{v} \cdot \mathbf{v} \right) dv + \frac{d}{dt} \int_{\mathcal{S}} \gamma \, da &= \int_{\mathcal{B}} (\mathbf{f} \cdot \mathbf{v} + \rho r) \, dv \\ &+ \int_{\partial \mathcal{B}} (\mathbf{t} \cdot \mathbf{v} - \mathbf{q}^h \cdot \mathbf{n}) \, da + \int_{\mathcal{B}} \varphi \frac{d}{dt} (\rho \, dv) + \int_{\partial \mathcal{B}} \varphi \frac{d}{dt} (\omega \, da), \end{aligned} \quad (3.99)$$

which introduces the specific internal energy per unit mass  $e$ , the specific energy of the interface  $\gamma$ , the heat supply per unit volume  $r$ , and the heat flux  $\mathbf{q}^h$ . The energy stored in the electric field outside the material body also contributes to the balance of energy; this is however ignored in the following. In contrast to the formulation in McMEEKING & LANDIS (2005), the vacuum electric energy inside the material body is included in the internal energy  $e$ .

The local form is obtained by evaluating the terms on the right hand side of Eq. (3.99), the external work rate. With (3.13), one obtains

$$\frac{d}{dt} (\rho \, dv) = (\dot{\rho} + \rho \, \text{div} \, \mathbf{v}) \, dv \quad (3.100)$$

and, with Eq. (3.68),

$$\frac{d}{dt}(\omega \, da) = \frac{d}{dt}([\mathbf{D} \cdot \mathbf{n}] \, da) = \left( \left[ \left[ \dot{\mathbf{D}} + \mathbf{D} \operatorname{div} \mathbf{v} - \mathbf{L} \mathbf{D} \right] \cdot \mathbf{n} \right) da . \quad (3.101)$$

When the vacuum Maxwell stress is neglected,  $\mathbf{t} = (\boldsymbol{\sigma} + \boldsymbol{\sigma}^M) \mathbf{n}$ , and the resulting flux term is then easily identified with  $\boldsymbol{\Xi} = (\boldsymbol{\sigma} + \boldsymbol{\sigma}^M)^T \mathbf{v} - \mathbf{q}^h - \varphi \dot{\mathbf{D}} + \varphi [(\mathbf{1} - \mathbf{1} \otimes \mathbf{1}) \mathbf{L}] \mathbf{D}$ . The balanced quantity is  $\phi = \varrho e + \frac{1}{2} \varrho \mathbf{v} \cdot \mathbf{v}$ , its volume supply  $\varsigma = \mathbf{f} \cdot \mathbf{v} + \varrho r + \varphi(\dot{\rho} + \rho \operatorname{div} \mathbf{v})$ . With  $\phi_S = \gamma$ , the conservation laws read

$$\varrho \dot{e} = [\boldsymbol{\sigma} + \boldsymbol{\sigma}^M + (\mathbf{E} \cdot \mathbf{D}) \mathbf{1} - \mathbf{E} \otimes \mathbf{D}] \cdot \mathbf{L} + \mathbf{E} \cdot \dot{\mathbf{D}} - \operatorname{div} \mathbf{q}^h + \varrho r \quad \text{in } \mathcal{B}^{+/-} \quad (3.102)$$

and, with Eq. (3.79)<sub>2</sub>,

$$\begin{aligned} & \left[ \left[ \varrho \left( e + \frac{1}{2} \mathbf{v} \cdot \mathbf{v} \right) (\mathbf{v} - \mathbf{w}) \right] \right] \cdot \mathbf{n}_S + \dot{\gamma} - \gamma \kappa w_n + [[\mathbf{q}^h]] \cdot \mathbf{n}_S \\ & - [[[(\boldsymbol{\sigma} + \boldsymbol{\sigma}^M) \mathbf{n}_S] \cdot \mathbf{v}]] + \varphi \left[ \left[ \dot{\mathbf{D}} \right] \right] \cdot \mathbf{n}_S - \varphi [[(\mathbf{1} - \mathbf{1} \otimes \mathbf{1}) \mathbf{L}] \mathbf{D}] \cdot \mathbf{n}_S = 0 \end{aligned} \quad (3.103)$$

on  $\mathcal{S}$ .

### Balance of entropy

With the entropy density  $s$ , the absolute temperature  $\theta$ , the entropy productions  $\pi_s$  and  $\varpi_s$  in  $\mathcal{B}^{+/-}$  and on  $\mathcal{S}$ , respectively, and with  $\phi = \varrho s$ ,  $\boldsymbol{\Xi} = -\frac{1}{\theta} \mathbf{q}^h$ ,  $\pi = \pi_s$ ,  $\varpi = \varpi_s$ , and the assumption that the specific surface entropy vanishes, i.e.  $\Phi_S = 0$ , the balance laws read

$$\begin{aligned} & \varrho \dot{s} + \operatorname{div} \frac{\mathbf{q}^h}{\theta} - \varrho \frac{r}{\theta} = \pi_s \quad \text{in } \mathcal{B}^{+/-} , \\ & [[\varrho s(\mathbf{v} - \mathbf{w})]] \cdot \mathbf{n}_S + \left[ \left[ \frac{\mathbf{q}^h}{\theta} \right] \right] \cdot \mathbf{n}_S = \varpi_s \quad \text{on } \mathcal{S} . \end{aligned} \quad (3.104)$$

According to the second law of thermodynamics, the entropy production must be non-negative:

$$\pi_s \geq 0 \quad \text{in } \mathcal{B}^{+/-} \quad \text{and} \quad \varpi_s \geq 0 \quad \text{on } \mathcal{S} . \quad (3.105)$$

### Clausius-Duhem inequality

In order to eliminate the specific internal energy, the Helmholtz free energy  $\psi$  is introduced with the Legendre transformation

$$\dot{\psi} = \dot{e} - \dot{\theta} s - \theta \dot{s} . \quad (3.106)$$

The combination of Eqs. (3.102) and (3.104)<sub>1</sub> with (3.105)<sub>1</sub> gives the Clausius-Duhem inequality

$$\varrho \dot{\psi} + \varrho s \dot{\theta} - [\boldsymbol{\sigma} + \boldsymbol{\sigma}^M + (\mathbf{E} \cdot \mathbf{D})\mathbf{1} - \mathbf{E} \otimes \mathbf{D}] \cdot \mathbf{L} - \mathbf{E} \cdot \dot{\mathbf{D}} + \frac{\mathbf{q}^h}{\theta} \cdot \text{grad } \theta \leq 0 . \quad (3.107)$$

By introducing the electric enthalpy  $H$  with the Legendre transformation

$$\dot{H} = \varrho \dot{\psi} - \dot{\mathbf{E}} \cdot \mathbf{D} - \mathbf{E} \cdot \dot{\mathbf{D}} , \quad (3.108)$$

the Clausius-Duhem inequality (3.107) becomes

$$\dot{H} + \varrho s \dot{\theta} - [(\boldsymbol{\sigma} + \boldsymbol{\sigma}^M + (\mathbf{E} \cdot \mathbf{D})\mathbf{1} - \mathbf{E} \otimes \mathbf{D}) \mathbf{F}^{-T}] \cdot \dot{\mathbf{F}} + \mathbf{D} \cdot \dot{\mathbf{E}} + \frac{\mathbf{q}^h}{\theta} \cdot \text{grad } \theta \leq 0 . \quad (3.109)$$

For points on  $\mathcal{S}$  one obtains

$$\begin{aligned} & - \left[ \left[ \left( H + \frac{1}{2} \varrho \mathbf{v} \cdot \mathbf{v} \right) (\mathbf{v} - \mathbf{w}) \right] \right] \cdot \mathbf{n}_S - [[\mathbf{n}_S \cdot (\mathbf{E} \otimes \mathbf{D}) \mathbf{n}_S (\mathbf{v} - \mathbf{w}) \cdot \mathbf{n}_S]] - \dot{\gamma} \\ & + \gamma \kappa w_n + \left[ [(\boldsymbol{\sigma} + \boldsymbol{\sigma}^M)^T \mathbf{v}] \right] \cdot \mathbf{n}_S - \varphi \left[ [\dot{\mathbf{D}} - [(\mathbf{1} - \mathbf{1} \otimes \mathbf{1}) \mathbf{L}] \mathbf{D}] \right] \cdot \mathbf{n}_S \geq 0 . \end{aligned} \quad (3.110)$$

The electric enthalpy is assumed to depend on the deformation gradient, the electric field, the temperature, and a set of internal variables  $\mathbf{q}$ , i.e.

$$H = \hat{H}(\mathbf{F}, \mathbf{E}, \theta, \mathbf{q}) . \quad (3.111)$$

Insertion in (3.109) yields

$$\begin{aligned} & \left( \frac{\partial \hat{H}}{\partial \theta} + \varrho s \right) \dot{\theta} + \left[ \frac{\partial \hat{H}}{\partial \mathbf{F}} - (\boldsymbol{\sigma} + \boldsymbol{\sigma}^M + (\mathbf{E} \cdot \mathbf{D})\mathbf{1} - \mathbf{E} \otimes \mathbf{D}) \mathbf{F}^{-T} \right] \cdot \dot{\mathbf{F}} \\ & + \left( \frac{\partial \hat{H}}{\partial \mathbf{E}} + \mathbf{D} \right) \cdot \dot{\mathbf{E}} + \frac{\mathbf{q}^h}{\theta} \cdot \text{grad } \theta + \frac{\partial \hat{H}}{\partial \mathbf{q}} \cdot \dot{\mathbf{q}} \leq 0 , \end{aligned} \quad (3.112)$$

which implies the constitutive relations<sup>19</sup>

$$\varrho s = - \frac{\partial \hat{H}}{\partial \theta} , \quad (3.113)$$

$$\boldsymbol{\sigma} = \frac{\partial \hat{H}}{\partial \mathbf{F}} \mathbf{F}^T - \boldsymbol{\sigma}^M - (\mathbf{E} \cdot \mathbf{D})\mathbf{1} + \mathbf{E} \otimes \mathbf{D} , \quad (3.114)$$

$$\mathbf{D} = - \frac{\partial \hat{H}}{\partial \mathbf{E}} , \quad (3.115)$$

---

<sup>19</sup>Cf. COLEMAN & NOLL (1963).

and leaves the residual inequality

$$-\frac{\mathbf{q}^h}{\theta} \cdot \text{grad } \theta - \frac{\partial \hat{H}}{\partial \mathbf{q}} \cdot \dot{\mathbf{q}} \geq 0 . \quad (3.116)$$

Assuming that  $\mathbf{q}^h$  is independent of  $\mathbf{q}$  and that  $\dot{\mathbf{q}}$  is independent of  $\text{grad } \theta$ , one may separate the inequalities to obtain the heat conduction inequality

$$-\frac{\mathbf{q}^h}{\theta} \cdot \text{grad } \theta \geq 0 \quad (3.117)$$

and the internal dissipation inequality

$$-\frac{\partial \hat{H}}{\partial \mathbf{q}} \cdot \dot{\mathbf{q}} \geq 0 . \quad (3.118)$$

The heat conduction inequality can be satisfied e.g. by the linear law of heat conduction  $\mathbf{q}^h = -\boldsymbol{\kappa}_q \text{grad } \theta$  with the positive definite heat conduction tensor  $\boldsymbol{\kappa}_q$ . The internal dissipation inequality is satisfied by a proper choice of the evolution law for the internal variables represented by  $\mathbf{q}$ ; this will be addressed in Ch. 4 and Ch. 5 in the context of modeling domain walls.

The debate on the correct choice of the Maxwell stress in Eq. (3.114) has been carried out for some time, see e.g. the contributions by TOUPIN (1956), ERINGEN (1963), McMEEKING & LANDIS (2005), VU ET AL. (2006), and McMEEKING ET AL. (2007), and is still ongoing. As shown in McMEEKING & LANDIS (2005), an additive decomposition of the total stress into the Cauchy- and Maxwell-stress is not unambiguous, rather only the total stress can be uniquely identified. With reference to TOUPIN (1956), McMEEKING & LANDIS (2005), MEHLING (2007), and Eqs. (3.50) and (3.51), the choice

$$\boldsymbol{\sigma}^M = \mathbf{E} \otimes \mathbf{D} - \frac{1}{2} \epsilon_0 (\mathbf{E} \cdot \mathbf{E}) \mathbf{1} \quad (3.119)$$

gives

$$\mathbf{f}^e = \rho \mathbf{E} + (\text{grad } \mathbf{E})^T \mathbf{P}^{\text{mat}} , \quad (3.120)$$

$$\mathbf{m}^e = \mathbf{x} \times \mathbf{F}^e + \mathbf{P}^{\text{mat}} \times \mathbf{E} , \quad (3.121)$$

where Eqs. (3.91) and (3.97) have been made use of.

### Material objectivity

The principle of material objectivity states that the material equations should be independent of the Euclidean transformation

$$\mathbf{x}^* = \mathbf{Q}(t) \mathbf{x} + \mathbf{c}(t) , \quad t^* = t - a \quad (3.122)$$

with  $\mathbf{Q}^{-1} = \mathbf{Q}^T$ ,  $\det \mathbf{Q} = 1$ . This is the case if the arguments of the electric enthalpy are objective quantities, which can be achieved by choosing the strain tensor  $\mathbf{G}$  and the objective electric field  $\mathbf{E}' = \mathbf{R}^T \mathbf{E}$  along with objective internal variables  $\mathbf{q}'$ . With the transformations  $\mathbf{F}^* = \mathbf{Q}\mathbf{F}$  and  $\mathbf{R}^* = \mathbf{Q}\mathbf{R}$ , one obtains

$$\mathbf{G}^* = \frac{1}{2} (\mathbf{F}^{*\top} \mathbf{F}^* - \mathbf{1}) = \mathbf{G} , \quad (3.123)$$

$$\mathbf{E}'^* = \mathbf{R}^{*\top} \mathbf{E}^* = \mathbf{R}^T \mathbf{E} = \mathbf{E}' . \quad (3.124)$$

Since, additionally, the temperature is (as any scalar quantity) objective, the electric enthalpy is objective, i.e.

$$H = \bar{\bar{H}}(\mathbf{G}^*, \mathbf{E}'^*, \theta^*, \mathbf{q}'^*) = \bar{\bar{H}}(\mathbf{G}, \mathbf{E}', \theta, \mathbf{q}') \quad (3.125)$$

which guarantees objective constitutive equations.

### Further assumptions and simplifications

- The material undergoes only small deformations. This is a reasonable assumption for ceramic ferroelectrics, for which the strain is usually below 1%. The distinction between current and reference configuration is dropped, and one obtains

$$\begin{aligned} \mathbf{G} &\approx \boldsymbol{\varepsilon} , \quad \mathbf{L}_{\text{sym}} \approx \dot{\boldsymbol{\varepsilon}} , \quad \det \mathbf{F} \approx 1 , \quad \mathbf{E}' \approx \mathbf{E} , \\ \nabla(\cdot) &= \text{grad}(\cdot) \approx \text{Grad}(\cdot) , \quad \partial_{\mathbf{x}}(\cdot) \approx \partial_{\mathbf{X}}(\cdot) . \end{aligned} \quad (3.126)$$

- Ferroelectrics have a high specific electrical resistance and are considered as non-conductive.<sup>20</sup> Therefore the current of free charges is assumed to vanish:

$$\mathbf{I} = \mathbf{0} . \quad (3.127)$$

- There are no free charges in the bulk or on any interface within the body, i.e.

$$\rho = 0 \quad \text{and} \quad [[\mathbf{D}]] \cdot \mathbf{n}_S = 0 . \quad (3.128)$$

These assumptions neglect the fact that free charges may be required to compensate for domain wall configurations which are not charge free by virtue

---

<sup>20</sup>See e.g. KAMLAH (2001).

of their geometrical arrangement<sup>21,22</sup>

- Isothermal conditions and a uniform temperature distribution are assumed, i.e.

$$\text{grad } \theta = \mathbf{0} , \quad \mathbf{q}^h = \mathbf{0} . \quad (3.129)$$

This is a very common assumption, cf. the cited literature on sharp interface and phase field modeling.

- Quasi-static conditions are assumed with respect to the velocity and acceleration of material points:

$$\mathbf{v} \approx \mathbf{0} , \quad \dot{\mathbf{v}} \approx \mathbf{0} . \quad (3.130)$$

- Electrostatic forces are neglected. This is a common assumption as the Maxwell stress is small compared to the Cauchy stress; an estimate is given in KAMLAH & WANG (2003). The simplifications

$$\boldsymbol{\sigma}^M = \mathbf{0} , \quad \mathbf{f}^e = \mathbf{0} , \quad \mathbf{m}^e = \mathbf{0} , \quad \mathbf{t}^e = \mathbf{0} \quad (3.131)$$

lead to a symmetric Cauchy stress tensor since the last two terms in (3.114) are of the same order as  $\boldsymbol{\sigma}^M$ .

- The movement of bound charges during poling processes as well as charges moving onto or away from electrodes lead to electric currents. It is a common assumption to neglect the associated magnetic phenomena and to assume electrostatic conditions.
- The electric displacement of the space surrounding the material body is small compared to the electric displacement of the body. Therefore the boundary condition (3.68) is reduced to

$$\mathbf{D} \cdot \mathbf{n} = -\omega . \quad (3.132)$$

---

<sup>21</sup>Such configurations cause strong electric fields required to satisfy electrostatic equilibrium and can cause difficulties e.g. in phase field simulations of domain switching in polycrystalline settings (therefore *not* presented in Ch. 5).

<sup>22</sup>See XU (1991, p. 4) and MOKRÝ ET AL. (2007).

For points in  $\mathcal{B}^{+/-}$ , the simplified set of equations then reads<sup>23</sup>

$$\operatorname{div} \boldsymbol{\sigma} + \mathbf{f} = \mathbf{0} , \quad (3.133)$$

$$\boldsymbol{\sigma} - \boldsymbol{\sigma}^T = \mathbf{0} , \quad (3.134)$$

$$\operatorname{div} \mathbf{D} - \rho = 0 , \quad (3.135)$$

$$\boldsymbol{\sigma} = \partial_{\boldsymbol{\varepsilon}} \bar{H} , \quad (3.136)$$

$$\mathbf{D} = -\partial_{\mathbf{E}} \bar{H} , \quad (3.137)$$

$$\boldsymbol{\varepsilon} = \frac{1}{2} (\mathbf{H} + \mathbf{H}^T) , \quad (3.138)$$

$$\mathbf{E} = -\nabla \varphi , \quad (3.139)$$

$$-\partial_q \bar{H} \cdot \dot{\mathbf{q}} \geq 0 . \quad (3.140)$$

For points on  $\mathcal{S}$ , the mechanical equilibrium condition becomes

$$[[\boldsymbol{\sigma}]] \mathbf{n}_{\mathcal{S}} = \mathbf{0} , \quad (3.141)$$

and, on use of Eqs. (3.78) and (3.128)<sub>2</sub>, the dissipation inequality reduces to

$$([H]) + \gamma \varkappa - \mathbf{n}_{\mathcal{S}} \cdot ([[\nabla \mathbf{u}]]^T \boldsymbol{\sigma} \mathbf{n}_{\mathcal{S}}) + \mathbf{n}_{\mathcal{S}} \cdot [[\mathbf{E} \otimes \mathbf{D}]] \mathbf{n}_{\mathcal{S}} w_n - \dot{\gamma} \geq 0 . \quad (3.142)$$

Within this work, only Dirichlet and Neumann boundary conditions are used:

$$\begin{aligned} \mathbf{u} - \mathbf{u}^* &= \mathbf{0} && \text{on } \partial \mathcal{B}_u , \\ \boldsymbol{\sigma} \cdot \mathbf{n} - \mathbf{t}^* &= \mathbf{0} && \text{on } \partial \mathcal{B}_t , \\ \varphi - \varphi^* &= 0 && \text{on } \partial \mathcal{B}_{\varphi} , \\ \mathbf{D} \cdot \mathbf{n} + \omega^* &= 0 && \text{on } \partial \mathcal{B}_{\omega} . \end{aligned} \quad (3.143)$$

### 3.5 Piezoelectric constitutive law

The induced charges in (3.60) are often assumed to be proportional to the macroscopic electric field. A non-conducting material for which this assumption is suitable is called *dielectric*. The material polarization is then given by  $\mathbf{P}^{\text{mat}} = \boldsymbol{\kappa} \mathbf{E}$ , so that Eq. (3.66) becomes

$$\mathbf{D} = (\epsilon_0 \mathbf{1} + \boldsymbol{\kappa}) \mathbf{E} = \boldsymbol{\epsilon} \mathbf{E} . \quad (3.144)$$

The second-order tensors  $\boldsymbol{\epsilon}$  and  $\boldsymbol{\kappa}$  are called permittivity and susceptibility, respectively, and are related by  $\boldsymbol{\epsilon} = \epsilon_0 \mathbf{1} + \boldsymbol{\kappa}$ .

<sup>23</sup>Although the density of free charges  $\rho$  has already been dismissed by Eq. (3.128)<sub>1</sub> and volume forces  $\mathbf{f}$  will not be used in the simulations, these quantities will continue to appear in the equations because of their usefulness in other contexts, cf. e.g. MUELLER ET AL. (2006).



Depending on the choice of free variables, the linear equations of piezoelectricity take different forms, see IKEDA (1990) or MEHLING (2007) for details. In terms of the electric enthalpy, these equations read

$$\boldsymbol{\sigma} = \mathbb{C}\boldsymbol{\varepsilon} - \mathbf{e}^T \mathbf{E} , \quad (3.145)$$

$$\mathbf{D} = \mathbf{e}\boldsymbol{\varepsilon} + \boldsymbol{\epsilon}\mathbf{E} , \quad (3.146)$$

which means that  $\mathbf{P}^{\text{mat}} = \boldsymbol{\kappa}\mathbf{E} + \mathbf{e}\boldsymbol{\varepsilon}$ . The material constants  $\mathbb{C}$  and  $\mathbf{e}$  are the mechanical stiffness and the third-order piezoelectric tensor, respectively.

Near the spontaneously polarized states, the electromechanical behavior of the ferroelectric bulk material can *locally* be described with the linear piezoelectric constitutive equations. However, the constitutive equations depend on the local poling state, because the material polarization, the spontaneous strain (relative to the cubic high temperature phase), and the material constants depend on the variant of spontaneous polarization at each material point. Thus the piezoelectric equations become

$$\boldsymbol{\sigma} = \mathbb{C}(\boldsymbol{\varepsilon} - \boldsymbol{\varepsilon}^0) - \mathbf{e}^T \mathbf{E} , \quad (3.147)$$

$$\mathbf{D} = \mathbf{e}(\boldsymbol{\varepsilon} - \boldsymbol{\varepsilon}^0) + \boldsymbol{\epsilon}\mathbf{E} + \mathbf{P}^0 , \quad (3.148)$$

where the material parameters  $\mathbb{C}$ ,  $\mathbf{e}$ ,  $\boldsymbol{\epsilon}$ , the spontaneous polarization  $\mathbf{P}^0$ , and the spontaneous strain  $\boldsymbol{\varepsilon}^0$  depend on the objective internal variable  $\mathbf{q}'$  which can now be identified with the state of spontaneous polarization. With reference to XU (1991) and Eq. (3.49), the electric enthalpy  $H$  takes the form

$$\begin{aligned} \bar{H}(\boldsymbol{\varepsilon}, \mathbf{E}, \mathbf{q}') &= \frac{1}{2} (\boldsymbol{\varepsilon} - \boldsymbol{\varepsilon}^0) \cdot [\mathbb{C}(\boldsymbol{\varepsilon} - \boldsymbol{\varepsilon}^0)] - (\boldsymbol{\varepsilon} - \boldsymbol{\varepsilon}^0) \cdot (\mathbf{e}^T \mathbf{E}) \\ &\quad - \frac{1}{2} \mathbf{E} \cdot (\boldsymbol{\epsilon}\mathbf{E}) - \mathbf{P}^0 \cdot \mathbf{E} . \end{aligned} \quad (3.149)$$

Evaluating Eqs. (3.136) and (3.137) with this electric enthalpy, one obtains the constitutive equations (3.147) and (3.148).

In the next chapter, a ferroelectric domain wall is treated as a sharp interface, and the set of position vectors  $\check{\mathbf{x}}(t)$  that define the surface is interpreted as the internal variable. Then dissipation takes place only on the interface, not in the bulk. In Ch. 5 the internal variables are chosen as the spontaneous polarization and its gradient.



# Chapter 4

## Sharp interface approach

As pointed out in Ch. 2, ferroelectric domain walls typically have a width of a few lattice constants. This gives rise to the treatment of a domain wall as an immaterial sharp interface or singular surface. The introduction of interfaces implies the presence of material inhomogeneities as certain material properties exhibit a jump across the interface. Thus the theory of configurational forces is applicable to the current problem. Textbooks on configurational forces written from a continuum-mechanical view include e.g. MAUGIN (1993), GURTIN (2000), KIENZLER & HERRMANN (2000); a review on the topic, which includes an electromechanical setting, is given in GROSS ET AL. (2003).

In order to fulfill the second law (3.142) on the interface  $\mathcal{S}$ , a kinetic law for the normal velocity  $w_n$  has to be specified. If a body contains multiple interfaces, the kinetics of the interfaces becomes quite involved, see SIMHA & BHATTACHARYA (1998), SIMHA & BHATTACHARYA (2000), GURTIN (1991), and GURTIN & VOORHEES (1993). These difficulties are circumvented here in that only single interfaces, which will later be assumed to be planar, are considered. The body is then divided into two domains, and the interface indicates a jump in the spontaneous polarization.

There seem to be not too many publications on ferroelectric domain wall motion based the notion of sharp interfaces. The work by LOGE & SUO (1996) introduces a set of generalized coordinates to capture the geometry of the domain state, and a linear kinetic law, based on a variational principle, relates the rates of these coordinates to the conjugate driving force; examples include spike-like domain growth and sideways interface motion. In the consecutive publications KESSLER & BALKE (2006a) and KESSLER & BALKE (2006b), the driving force is derived within a thermodynamic framework emphasizing the bending of domain walls; numerical

examples are given for a bending  $90^\circ$  interface due to surface charges and for a circular domain in equilibrium.

The subsequent sections of this chapter are based on the procedures outlined in MUELLER ET AL. (2006) where a variational principle is used, and on SCHRADE ET AL. (2007a) in which a thermodynamic approach is taken. In the following section, a kinetic law for domain wall movement is postulated on the basis of the driving force on the interface. The resulting equations are then discretized with regard to a finite element implementation. Numerical simulations show the effect of different kinds of defects on the mobility of a  $180^\circ$  domain wall. The results are compared with experiments on single crystal gadolinium molybdate (GMO),  $\text{Gd}_2(\text{MoO}_4)_3$ .

## 4.1 Driving force and interface kinetics

The sharp interface approach is based on the assumption that each ferroelectric domain is a materially homogeneous region and that material properties may exhibit a jump across an interface. Thus the internal variable of the electric enthalpy in Eq. (3.149) can be seen as the position of the interface  $\mathcal{S}$ . The dissipation inequality (3.140) is then trivially fulfilled for points within the bulk, and dissipation only takes place on the interface according to Eq. (3.142). In the presence of just one interface, the explicit spatial dependency of the electric enthalpy can be formulated by

$$\begin{aligned} \bar{H}(\boldsymbol{\varepsilon}, \mathbf{E}, \mathbf{x}; \mathcal{S}) = & \frac{1}{2} (\boldsymbol{\varepsilon} - \boldsymbol{\varepsilon}_\pm^0) \cdot [\mathbb{C}_\pm (\boldsymbol{\varepsilon} - \boldsymbol{\varepsilon}_\pm^0)] - (\boldsymbol{\varepsilon} - \boldsymbol{\varepsilon}_\pm^0) \cdot (\boldsymbol{\varepsilon}_\pm^T \mathbf{E}) \\ & - \frac{1}{2} \mathbf{E} \cdot (\boldsymbol{\varepsilon}_\pm \mathbf{E}) - \mathbf{P}_\pm^0 \cdot \mathbf{E} , \end{aligned} \quad (4.1)$$

where the material parameter  $(\cdot)_+$  is used if  $\mathbf{x} \in \mathcal{B}^+$  and  $(\cdot)_-$  is used if  $\mathbf{x} \in \mathcal{B}^-$  (cf. Fig. 3.6).

For the evaluation of the dissipation inequality (3.142), the configurational stress tensor is introduced as<sup>1</sup>

$$\boldsymbol{\Sigma} = H\mathbf{1} - (\nabla \mathbf{u})^T \boldsymbol{\sigma} + \mathbf{E} \otimes \mathbf{D} . \quad (4.2)$$

With the definition of the (scalar) driving force  $\tau_n$  as

$$\tau_n = \mathbf{n}_\mathcal{S} \cdot ([[\boldsymbol{\Sigma}]] \mathbf{n}_\mathcal{S}) + \gamma \varkappa , \quad (4.3)$$

---

<sup>1</sup>Cf. GROSS ET AL. (2003).

the second law (3.142) then reads

$$\tau_n w_n - \dot{\gamma} \geq 0 \quad \text{on } \mathcal{S} . \quad (4.4)$$

In view of the numerical examples in Sec. 4.3 and the experimental studies on GMO (FLIPPEN 1975, UTSCHIG 2005), it is additionally assumed that the specific interface energy  $\gamma$  is constant on  $\mathcal{S}$  and in time  $t$  and that the interface  $\mathcal{S}$  is planar at all times. The dissipation inequality then reduces to

$$\tau_n w_n \geq 0 \quad \text{on } \mathcal{S} \quad (4.5)$$

with the driving force

$$\tau_n = \mathbf{n}_\mathcal{S} \cdot ([[\boldsymbol{\Sigma}]] \mathbf{n}_\mathcal{S}) . \quad (4.6)$$

This result does not imply a specific kinetic law for the interface normal velocity  $w_n$ . For the formulation of such a relationship, experimental studies on GMO by FLIPPEN (1975) are taken into account. In these experiments, the domain wall dynamics of an individual  $180^\circ$  domain wall in single crystal GMO was studied in that a domain wall was moved through the material by the application of a homogeneous electric field  $E$  perpendicular to the interface normal. The measurements suggest a linear relationship between the interface velocity  $w_n$  and the applied field  $E$ . The kinetic law can be stated in terms of the applied electric field by

$$w_n = \bar{\mu}(E - E_0) . \quad (4.7)$$

The parameter  $\bar{\mu}$  defines the domain wall mobility, and  $E_0$  is an offset field at which interface movement sets in. However, this simple relation only holds for a homogeneous electric field. For the case of inhomogeneous fields, which is of interest here, and in view of the second law (4.5), the kinetic law needs to be formulated in terms of the driving force  $\tau_n$ . Intending to do so, the average resulting driving force  $T_n$  acting on the interface is introduced as

$$T_n(\tau_n) = \frac{1}{A_\mathcal{S}} \int_\mathcal{S} \tau_n \, da , \quad (4.8)$$

where  $A_\mathcal{S} = \int_\mathcal{S} da$  is the surface area of  $\mathcal{S}$ . Since only plane interfaces are considered here, the normal velocity  $w_n$  is homogeneous on  $\mathcal{S}$ . This allows for the formulation of a kinetic law for the interface normal velocity  $w_n$  as a function of  $T_n$ , i.e. the dependency on the surface points of  $\mathcal{S}$  is dropped. Figure 4.1 shows three particular thermodynamically admissible constitutive relations. The kinetic law postulated here has the form

$$w_n = \begin{cases} \mu(T_n - T_0) & \text{if } T_n \geq T_0 , \\ 0 & \text{if } |T_n| < T_0 , \\ \mu(T_n + T_0) & \text{if } T_n \leq -T_0 . \end{cases} \quad (4.9)$$

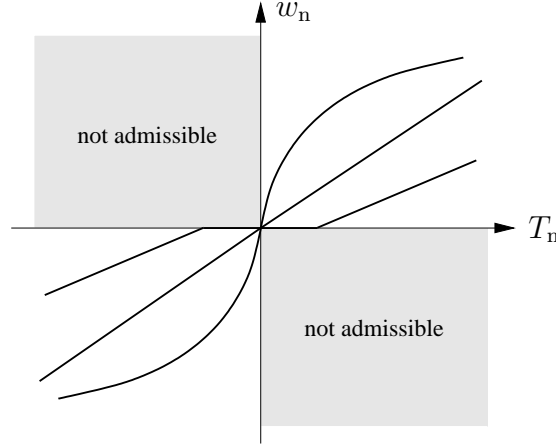


Figure 4.1: Sketch of admissible kinetic relations for domain wall movement.

The parameters  $\mu$  and  $T_0$  are the interface mobility and the offset average driving force, respectively. It is noted that this relationship implies the assumption that the interface kinetics is independent of the dimensions of the interface. More recent studies on the dynamics of domain walls in gadolinium molybdate can be found in SHUR ET AL. (1990), SHUR ET AL. (1992), and SHUR ET AL. (1999).

The driving force on a  $180^\circ$  domain wall in the presence of an electric field  $E$  parallel to the interface can be obtained from Eq. (4.6). As shown in App. A.1, this driving force can be approximated by<sup>2</sup>

$$\tau_n \approx [[\mathbf{P}^0 \cdot \mathbf{E}]] = 2P^0 E \quad (4.10)$$

with  $P^0 = |\mathbf{P}^0|$ . The value of  $T_0$  is obtained from Eqs. (4.8) and (4.10) for  $E = E_0$ :

$$T_0 = \frac{1}{A_S} \int_S \tau_n(E_0) da = \tau_n(E_0) = 2P^0 E_0 . \quad (4.11)$$

For  $E = 2E_0$ , and hence  $T_n = 2T_0$ , the combination of Eq. (4.7) with (4.9) gives

$$w_n = \mu(T_n - T_0) = \mu T_0 = 2\mu P^0 E_0 = \bar{\mu} E_0 , \quad (4.12)$$

so that

$$\mu = \frac{\bar{\mu}}{2P^0} . \quad (4.13)$$

The values for  $\bar{\mu}$  and  $E_0$  can be obtained from FLIPPEN (1975), see Sec. 4.3 for details.

---

<sup>2</sup>Cf. LOGE & SUO (1996).

## 4.2 Numerical aspects

The electromechanical problem consists of the partial differential equations (3.133) and (3.135) in context with Eqs. (3.134), (3.136)–(3.139), and (4.1), furthermore of the associated jump conditions (3.141) and (3.128) and the boundary conditions (3.143). Moreover, the stated problem is inherently time dependent due to the movement of interfaces as described by the kinetic law (4.9). The underlying concept for the solution process is to solve the electromechanical field equations for fixed domain wall positions in a quasi-static manner. Initially, the field equations are solved for the (prescribed) initial interface position. With that solution, the resulting driving force on the interface is computed as a matter of post-processing. The domain wall position can then be obtained by numerical integration of Eq. (4.9).

The finite element implementation is straightforward and not explained in detail here. For standard textbooks on that subject, the reader is referred to ZIENKIEWICZ & TAYLOR (2000), HUGHES (2000), and WRIGGERS (2009). In the context of piezoelectrics, the early work by ALLIK & HUGHES (1970) is worth mentioning; in LANDIS (2002), a vector potential is used to derive the components of the electric field. A detailed account of the finite element formulation of the current electromechanical problem can be found in MUELLER ET AL. (2006).

### Driving force

Once the boundary value problem is solved, it is possible to calculate the driving force on the interface. This is a non-trivial task as the configurational stress defined in Eq. (4.2) contains nodal as well as Gauss point quantities. Though it is possible to project Gauss point values onto element nodes, this method is not preferable due to its conceptual inconsistency. A more sophisticated approach utilizes the concept of configurational forces. The configurational stress tensor satisfies the balance equation<sup>3</sup>

$$\operatorname{div} \boldsymbol{\Sigma} + \mathbf{g} = \mathbf{0} \quad \text{in } \mathcal{B}^{+/-} , \quad (4.14)$$

where  $\mathbf{g}$  is the configurational force vector. Multiplication with a test function  $\boldsymbol{\eta}$  and subsequent integration by parts yields

$$- \int_{\mathcal{B}^{+/-}} \boldsymbol{\Sigma} \cdot \nabla \boldsymbol{\eta} \, dv + \int_{\mathcal{B}^{+/-}} \mathbf{g} \cdot \boldsymbol{\eta} \, dv = 0 , \quad (4.15)$$

---

<sup>3</sup>See GURTIN (2000, Ch. 5) and MUELLER ET AL. (2002) for details.

where the test function is assumed to vanish on  $\partial\mathcal{B}$ . The test function and its gradient are then approximated on the element level by

$$\boldsymbol{\eta} = \sum_I N^I \boldsymbol{\eta}^I \quad \text{and} \quad \nabla \boldsymbol{\eta} = \sum_I \boldsymbol{\eta}^I \otimes \nabla N^I, \quad (4.16)$$

where  $N^I$  are the shape functions and  $\boldsymbol{\eta}^I$  the nodal values of the shape function at node  $I$ . Inserting these approximations in Eq. (4.15) gives

$$\sum_I \left[ \int_{\mathcal{B}^e} (\boldsymbol{\Sigma} \nabla N^I - \mathbf{g} N^I) dv \right] \cdot \boldsymbol{\eta}^I = 0, \quad (4.17)$$

where the summation is over all finite elements  $\mathcal{B}^e$ . As the term in the brackets must vanish for arbitrary test functions, the configurational force at node  $I$  in element  $\mathcal{B}^e$  is identified as

$$\mathbf{G}_e^I = \int_{\mathcal{B}^e} \mathbf{g} N^I dv = \int_{\mathcal{B}^e} \boldsymbol{\Sigma} \nabla N^I dv. \quad (4.18)$$

The resulting configurational force at node  $K$  is obtained by assembling all  $n_e$  elements adjacent to node  $I$ :

$$\mathbf{G}^K = \bigcup_{e=1}^{n_e} \mathbf{G}_e^I. \quad (4.19)$$

For the interface  $\mathcal{S}$ , the normal configurational force  $G_n$  is defined by

$$G_n = \sum_K \mathbf{G}_S^K \cdot \mathbf{n}_S, \quad (4.20)$$

where the summation is over all nodes lying on  $\mathcal{S}$ . On the other hand, the balance law (4.14) for points on  $\mathcal{S}$  reduces to<sup>4</sup>

$$[[\boldsymbol{\Sigma}]] \mathbf{n}_S + \mathbf{G}_S = \mathbf{0}, \quad (4.21)$$

$\mathbf{G}_S$  denoting the surface configurational force acting on  $\mathcal{S}$ . Scalar multiplication with  $-\mathbf{n}_S/A_S$  and integration over  $\mathcal{S}$  yields

$$-\frac{1}{A_S} \int_S \mathbf{G}_S \cdot \mathbf{n}_S da = \frac{1}{A_S} \int_S \tau_n da = T_n. \quad (4.22)$$

With the finite element approximation (4.18), the average driving force on  $\mathcal{S}$  can be obtained from

$$T_n = -\frac{1}{A_S} \int_S \mathbf{G}_S \cdot \mathbf{n}_S da = -\frac{1}{A_S} \sum_K \mathbf{G}_S^K \cdot \mathbf{n}_S = -\frac{1}{A_S} G_n. \quad (4.23)$$

---

<sup>4</sup>Cf. GROSS ET AL. (2003).



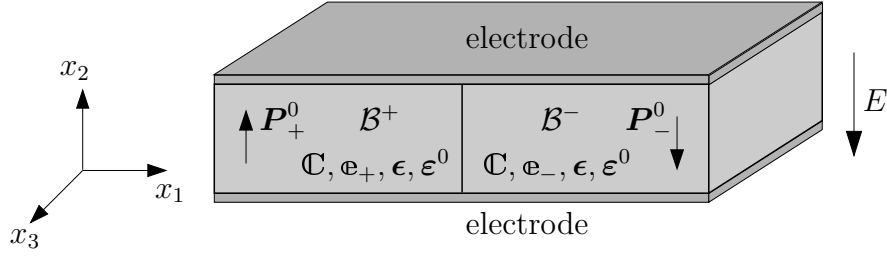


Figure 4.2: Sample with two domains separated by an  $180^\circ$  domain wall with electrodes attached at the top and bottom providing an applied external electric field  $E$ .

### Time integration

The kinetic law (4.9) is discretized in time by means of an explicit time integration of first order. The continuous interface position  $x_S(t)$  then becomes

$$x_S^{n+1} = x_S^n + w_n^n \Delta t, \quad (4.24)$$

where the indices  $n$  and  $n + 1$  denote the current time step  $t_n$  and the next time step  $t_{n+1}$  after the time interval  $\Delta t$ , which is taken to be constant, respectively.

The interface position  $x_S^{n+1}$  of the next time step does not necessarily coincide with element boundaries. Instead of creating a new mesh at every time step, a discrete interface position is defined by means of the closest available surface definable with the element boundaries of the constant mesh. This method requires a sufficiently refined mesh to guarantee an acceptable error in the time integration. The time integration itself is performed with the continuous interface position defined in Eq. (4.24). Once the discrete interface position is found for time step  $t_{n+1}$ , the boundary value problem for  $t_{n+1}$  can be solved.

## 4.3 Examples

The numerical examples given in this section are based on gadolinium molybdate (GMO) single crystals experiments in which single  $180^\circ$  domain walls were driven over certain kinds of defects by the application of an electric field perpendicular to the interface normal.<sup>5</sup> The defect-free setting, consisting of the electroded sample with two domains and the applied electric field, is sketched in Fig. 4.2. In this setup the field quantities do not depend on  $x_3$ , so that it is reasonable to restrict

<sup>5</sup>See SCHRADE ET AL. (2007a) and UTSCHIG (2005) for a detailed description as well as the publication by LUPASCU ET AL. (2002).

modeling to the  $(x_1, x_2)$ -plane. This is achieved by assuming plane strain conditions and a vanishing electric field component  $E_3$  for the mechanical and the electrical problem, respectively.

The material parameters for the mechanical stiffness can be found in HÖCHLI (1972); the dielectric constants are given in XU (1991, p. 310). Due to the lack of availability, the piezoelectric constants are assumed to be 1/100 of typical values for PZT. The spontaneous polarization  $P^0$  is stated in COLDREN ET AL. (1977) and XU (1991, p. 309), and the components of the spontaneous strain are calculated from the cell parameters of the pseudo-tetragonal system given in KEVE ET AL. (1971) and NEWNHAM ET AL. (1969). With respect to the Voigt notation  $\underline{\epsilon} = [\epsilon_{11} \ \epsilon_{22} \ 2\epsilon_{12}]^T$  and  $\underline{E} = [E_1 \ E_2]^T$ , the following material parameters for  $\mathcal{B}^+$  and  $\mathcal{B}^-$  (cf. Fig. 4.2) are used:<sup>6</sup>

$$\begin{aligned} \underline{\mathbb{C}} &= \begin{bmatrix} 6.82 & 2.0 & 0 \\ 2.0 & 9.82 & 0 \\ 0 & 0 & 2.55 \end{bmatrix} \cdot 10^{10} \frac{\text{N}}{\text{m}^2}, \quad \underline{\epsilon} = \begin{bmatrix} 8.41 & 0 \\ 0 & 9.29 \end{bmatrix} \cdot 10^{-11} \frac{\text{C}}{\text{Vm}}, \\ \underline{\mathfrak{e}}_{\pm} &= \begin{bmatrix} 0 & 0 & \pm 17.0 \\ \mp 6.5 & \pm 23.3 & 0 \end{bmatrix} \cdot 10^{-2} \frac{\text{C}}{\text{m}^2}. \end{aligned} \quad (4.25)$$

For the spontaneous polarization and spontaneous strain, the values

$$\underline{P}_{\pm}^0 = \begin{bmatrix} 0 & \pm 0.002 \end{bmatrix}^T \frac{\text{C}}{\text{m}^2} \quad \text{and} \quad \underline{\epsilon}^0 = \begin{bmatrix} -0.004 & 0.024 & 0 \end{bmatrix}^T \quad (4.26)$$

are chosen. Values for the interface mobility  $\bar{\mu}$  in (4.13), and thereby for  $\mu$  in (4.9), can be found in FLIPPEN (1975), TODA ET AL. (1973), and SHUR ET AL. (1990); here

$$\mu = \frac{\bar{\mu}}{2P^0} = \frac{2.1 \cdot 10^{-6} \text{ m}^2/(\text{Vs})}{2 \cdot 0.002 \text{ C m}^{-2}} = 5.25 \cdot 10^{-4} \frac{\text{m}^4}{\text{Js}} \quad (4.27)$$

is chosen. The value for the threshold field  $E_0$  in Eq. (4.7) varies in the literature just cited; the simulations are performed with

$$E_0 = 10^5 \frac{\text{V}}{\text{m}} \implies T_0 = 400 \frac{\text{J}}{\text{m}^3}. \quad (4.28)$$

The finite element model consists of plane 4-noded elements with bilinear shape functions. Although being part of the samples, the electrodes are not modeled with elements, but are incorporated by prescribing a difference in the electric potential

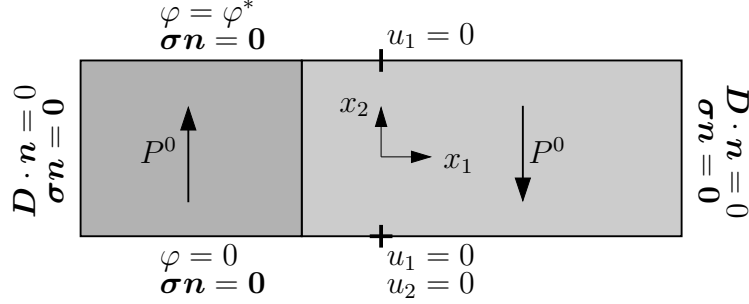


Figure 4.3: Boundary conditions for the 2d problem, side view.

by means of Dirichlet boundary conditions, see Fig. 4.3. The boundary is assumed to be traction free, and the electric displacement component  $D_1$  is presumed to vanish at the sides. Three mechanical displacement components at the top and bottom are fixed to rule out rigid body motions. The displacement conditions do not exactly reflect the experimental setting but are acceptable for the current purposes. Volume forces are not used in the simulations, i.e.  $\mathbf{f} = \mathbf{0}$  in (3.133); also recall that  $\rho = 0$ .

### 4.3.1 Electrode defect

In the experiments presented in UTSCHIG (2005), artificial defects were induced in the top electrode of GMO samples by laser ablation. These defects had a circular shape with diameters ranging from 0.04 mm–0.2 mm. Single domain walls were then driven toward a defect by an external electric field. Figure 4.4 shows a situation in which a domain wall, moved from the right to the left, has stopped in front of an electrode defect.

Since the damage inflicted on the electrode is difficult to estimate, the defect is modeled in two different ways: with the Neumann condition  $\mathbf{D} \cdot \mathbf{n} = 0$  and with the Dirichlet condition  $\varphi^* = 0$ , each applied over a length of 0.2 mm. Within the 2d description, this corresponds to regions which extend over the whole width of a sample in the  $x_3$ -direction. The dimensions of the mesh used in the simulations are 6 mm  $\times$  0.8 mm.

#### Interface approaching the electrode defect

In a first simulation, a domain wall is moved from right to left by the application of a voltage difference of 400 V, which gives an electric field of 0.5 MV/m in regions

<sup>6</sup>Note that second-order tensors are invariant to rotations by  $180^\circ$  ( $\rightsquigarrow Q_{ij} = -\delta_{ij}$ ).

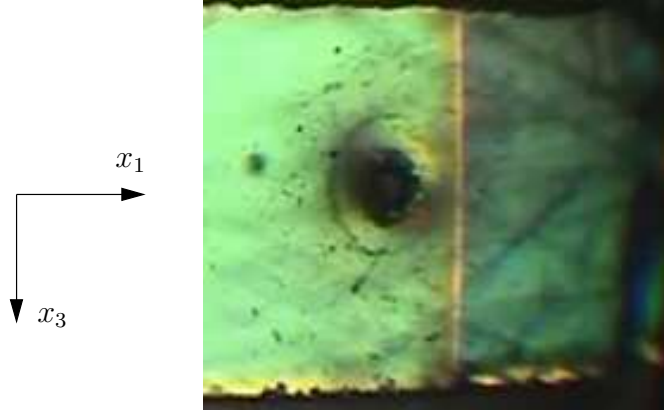


Figure 4.4: Domain wall stopped in front of an electrode defect, top view. Reprinted from SCHRADE ET AL. (2007a).

sufficiently far away from the defect. Figures 4.5 and 4.6 show plots of the resulting distributions of the driving force  $\tau_n$  for different distances of the interface from the beginning of the defect. For comparison,  $\tau_n$  is also plotted for the defect-free case. The defect condition  $\mathbf{D} \cdot \mathbf{n} = 0$  (Fig. 4.5) causes a strong electric field directed in the negative  $x_2$ -direction to compensate for the spontaneous polarization at the boundary. This leads to an increased driving force in the lower part of the interface. Toward the upper part near the defect,  $\tau_n$  changes its sign and points away from the defect. The defect condition  $\varphi^* = 0$  (Fig. 4.6) causes a weakened electric field in the area around the bottom part of the interface which leads to a decreased driving force in that region. Near the defect in the upper part of the domain wall,  $\tau_n$  has large negative values caused by the strong electric field due to the effect of the defect boundary condition. While in the second scenario the driving force always points in the direction of the defect, the first shows “repulsive” driving forces pointing in the opposite direction.

The kinetics of the interface is determined by the total average driving force  $T_n$  which is plotted in Figs. 4.7 and 4.8 against the distance of the interface to the defect for the two defect conditions under consideration. In both plots,  $T_n$  is nearly constant for positions in front of the defect. Its value coincides with that of the defect-free case in which  $T_n = 2P^0E_2 = -2\text{kJ/m}^3$ . Thus the domain wall approaches the defect in the same way as it would in the absence of the defect. The situation changes when the interface reaches the beginning of the defect. Under the first defect condition,  $T_n$  exceeds the threshold value  $T_0 = 400\text{J/m}^3$  by far, which implies that the domain wall is driven into the region under the defect. For the second defect,  $T_n$  falls below  $T_0$  which results in domain wall pinning at the beginning of the defect.

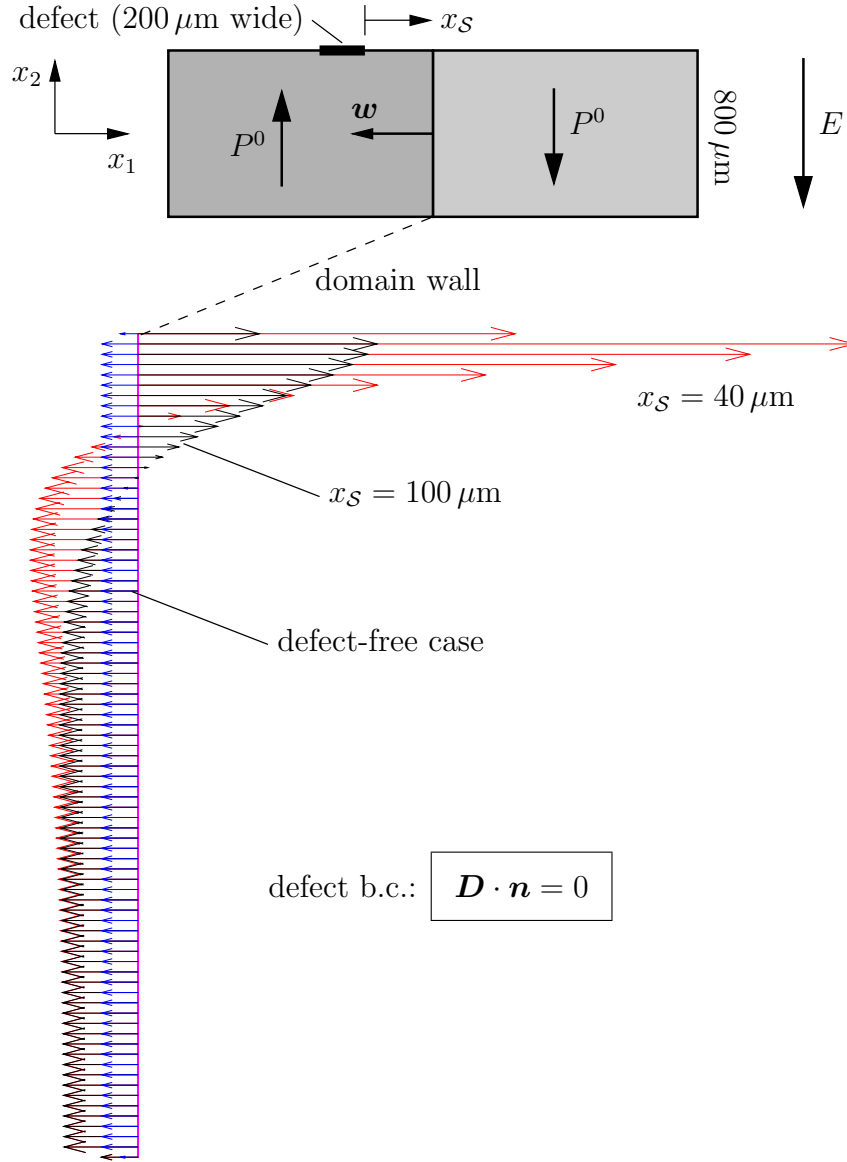


Figure 4.5: Distribution of  $\tau_n$  for different interface positions in comparison to the defect-free case. The positive driving force at the top has an impeding influence on further domain wall movement in the negative  $x_1$ -direction; the negative driving force at the bottom supports movement in that direction. Averaged driving forces as a function of  $x_S$  are shown in Fig. 4.7.

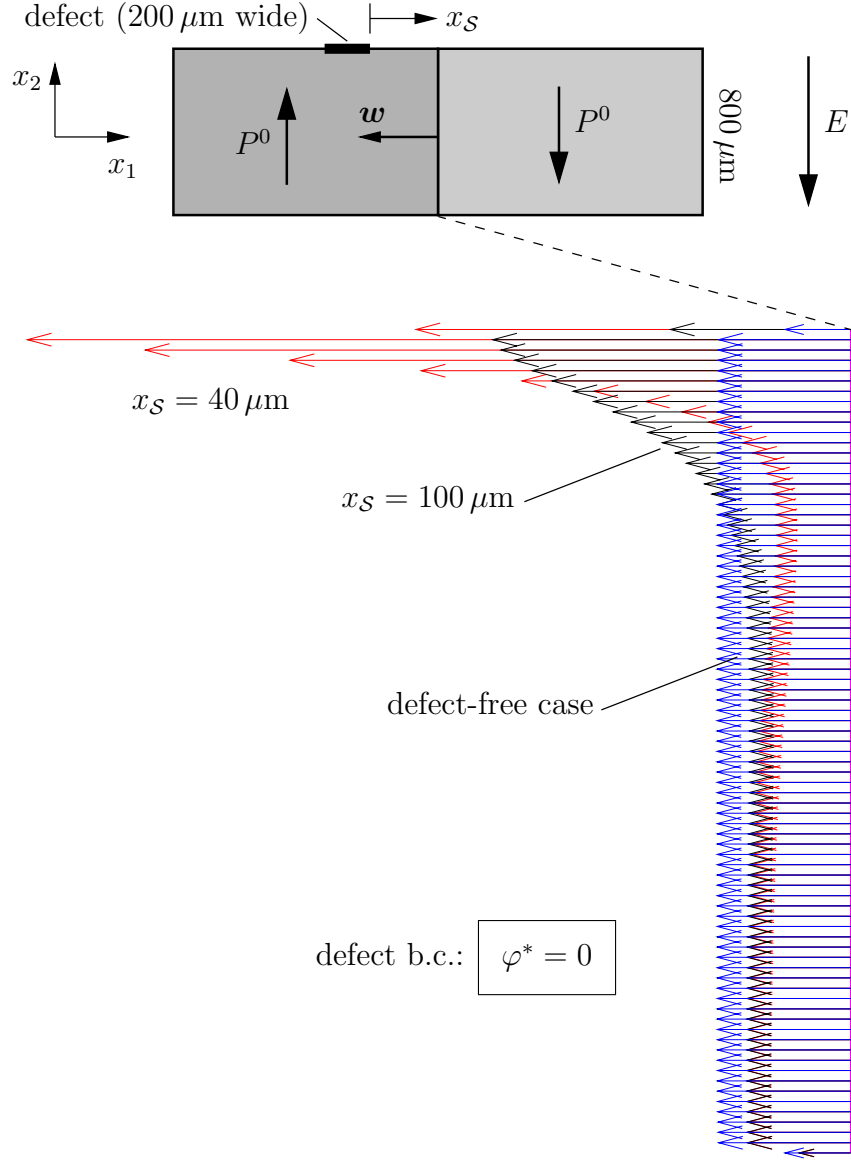


Figure 4.6: Distribution of  $\tau_n$  for different interface positions in comparison to the defect-free case. The driving force is reduced in the lower part of the interface compared to the defect-free case; the top part is strongly attracted to the defect. Averaged driving forces as a function of  $x_S$  are shown in Fig. 4.8.

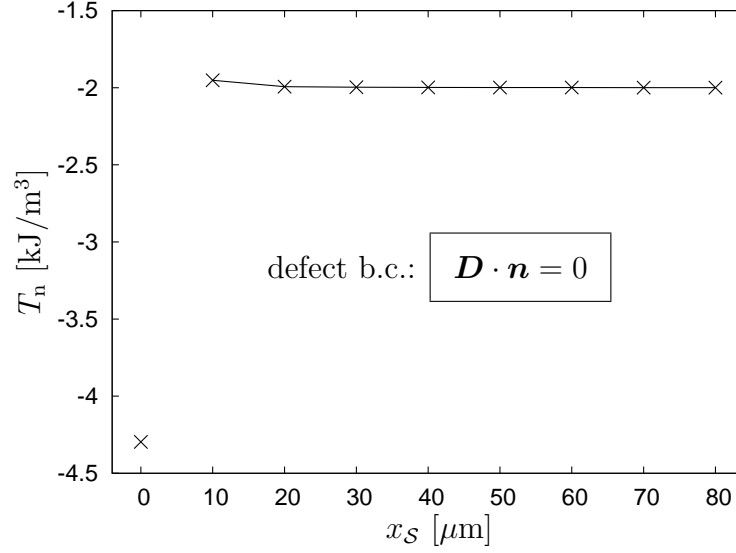


Figure 4.7:  $T_n$  as a function of the interface position  $x_S$  (cf. Fig. 4.5). The domain wall movement is unaffected by the defect as  $T_n$  has the same value as for the defect-free setting. The graph is continued in Fig. 4.11 for interface positions under the defect.

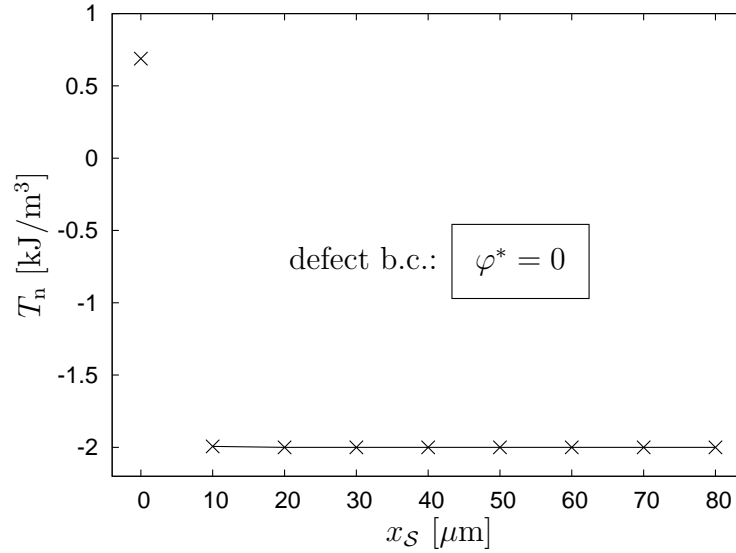


Figure 4.8:  $T_n$  as a function of the interface position  $x_S$  (cf. Fig. 4.6). As in Fig. 4.7, the domain wall movement is unaffected by the defect. The positive value of  $T_n$  for  $x_S = 0$  indicates domain wall pinning wall just in front of the defect, cf. the continued graph in Fig. 4.12.

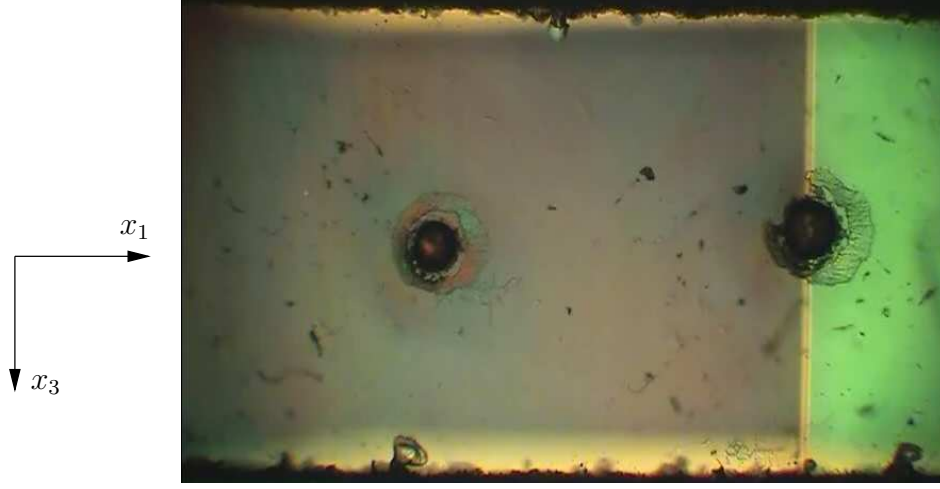


Figure 4.9: Domain wall trapped inside the electrode defect, top view. Reprinted from SCHRADE ET AL. (2007a).

### Interface under the electrode defect

In another experiment, a domain wall was moved under an electrode defect, where it was pinned in the middle of the defect (see Fig. 4.9). This scenario is simulated by placing a domain wall under the electrode defect; the geometrical and loading parameters are the same as in the previous simulations.

To begin with, the defect condition  $\mathbf{D} \cdot \mathbf{n} = 0$  is studied. Figure 4.10 shows the driving force for domain wall positions  $50 \mu\text{m}$  and  $70 \mu\text{m}$  to the right and left of the center of the defect, respectively. The distribution of  $\tau_n$  for  $x_S = 50 \mu\text{m}$  implies that the domain wall is strongly attracted to the center of the defect. The average driving force  $T_n$  is plotted against the domain wall position in Fig. 4.11. As shown in the previous simulations, the interface is driven into the defect area as it reaches the defect at  $x_S = 100 \mu\text{m}$ . Near that position, the absolute value of  $T_n$  stays well above  $T_0$ ; however, the domain wall is pinned at approximately  $x_S = -20 \mu\text{m}$  just left of the center of the defect.

The situation changes when the defect condition  $\varphi^* = 0$  is considered. Again  $T_n$  is evaluated for interface positions under the defect. The results, shown in Fig. 4.12, imply that the interface does not pass the beginning of the defect at  $x_S = 100 \mu\text{m}$ . A domain wall trapped in this kind of defect cannot be moved outside the defect area since  $T_n \approx 0$ .



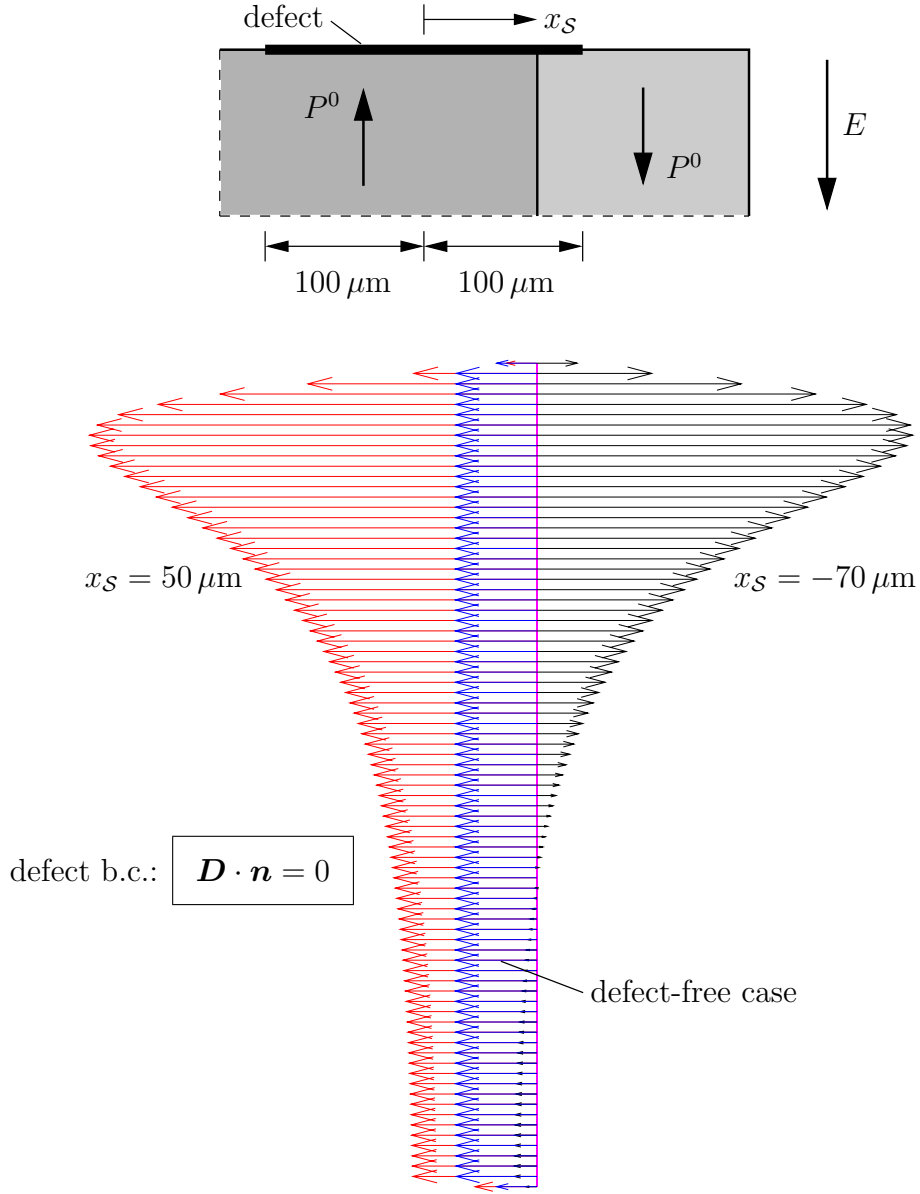


Figure 4.10: Distribution of  $\tau_n$  for different interface positions under the defect in comparison to the defect-free case;  $x_S = 0$  marks the center of the defect. The change in sign of  $\tau_n$ , and hence in  $T_n$ , indicates that the domain wall is pinned somewhere in between the two evaluated positions. This can be seen in Fig. 4.11, where  $T_n$  is plotted against the interface position.

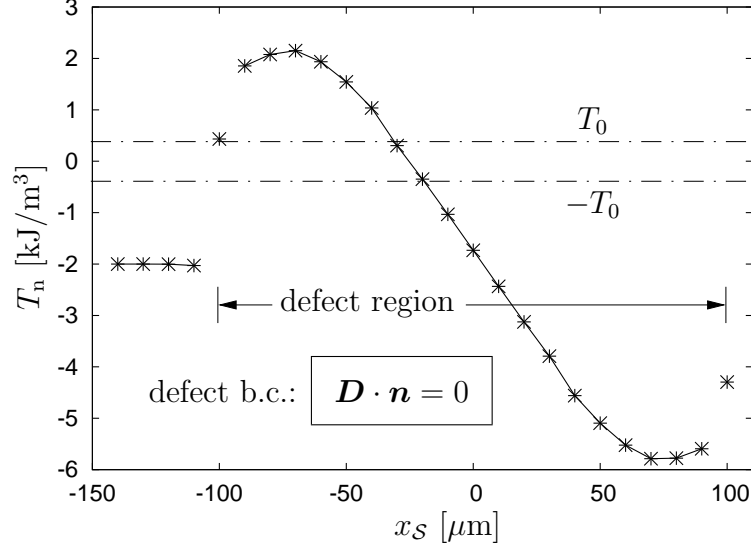


Figure 4.11:  $T_n$  as a function of the interface position  $x_S$ . As the domain walls reaches the defect from the right, it is driven further toward the defect center at  $x_S = 0$ . Pinning takes place at  $x_S = -20 \mu\text{m}$  where  $T_n = -T_0$ .

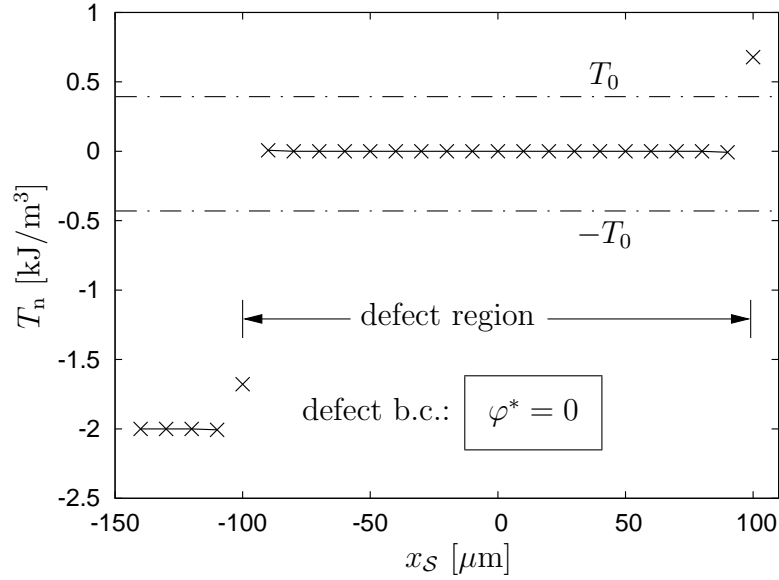


Figure 4.12:  $T_n$  as a function of the interface position  $x_S$ . The domain wall is pinned at the beginning of the defect and cannot be moved further to the left as  $T_n \approx 0$ .

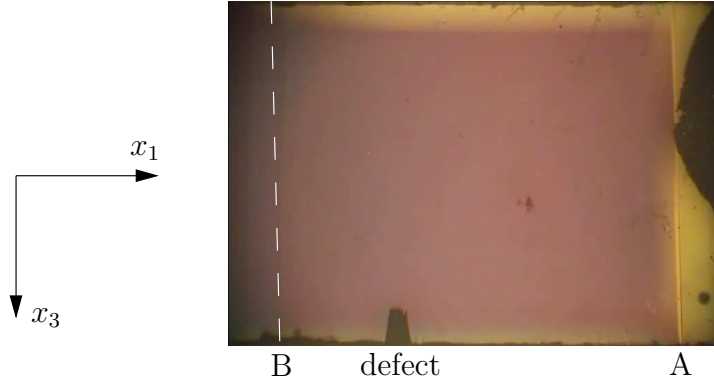


Figure 4.13: Domain wall is moved over a side defect, top view. The dashed line indicates the equilibrium interface position after it was moved over the defect. Reprinted from UTSCHIG (2005) and SCHRADE ET AL. (2007a).

#### 4.3.2 Side defect

Another set of experiments in UTSCHIG (2005) involves samples with holes which were burned into one of the side faces. Figure 4.13 shows a top view of a sample with such a side defect (bottom of the image); the electrodes at the top and bottom remained completely intact. The domain wall, which was initially located on the right side, was moved over the defect until it reached an equilibrium position at the left end of the sample (cf. Fig. 4.13). It was then moved back to its initial position. From optical observations, the defect had no effect on the domain wall motion — in contrast to the observed pinning effect of the electrode defect (cf. Sec. 4.3.1).

A better time resolution was achieved by measuring the switching current  $I_p$  for the domain wall motion from position A to position B in Fig. 4.13. The resulting graph (see Fig. 4.14 a) exhibits a sharp peak near 30.05 ms, which indicates that the domain wall was slowed down within a short time interval. The peak occurs at approximately 2/3 of the interval in which domain wall movement took place. As one can see in Fig. 4.13, this corresponds to the moment when the domain wall was passing the defect. For the way back to its initial position, there is only a slight change in  $I_p$  shortly after 20 ms, see Fig. 4.14 b). The switching current indicates that the domain wall motion was virtually unaffected by the defect.

The numerical simulations show a similar behavior. The defect is assumed to be quadratic with an edge length of  $120\ \mu\text{m}$ , and it is placed in the center of the mesh; this approximates the geometry for a specific defect treated in UTSCHIG (2005). The defect is modeled as a region filled with air, which is achieved by using the permittivity of air and a set of mechanical stiffness constants five orders

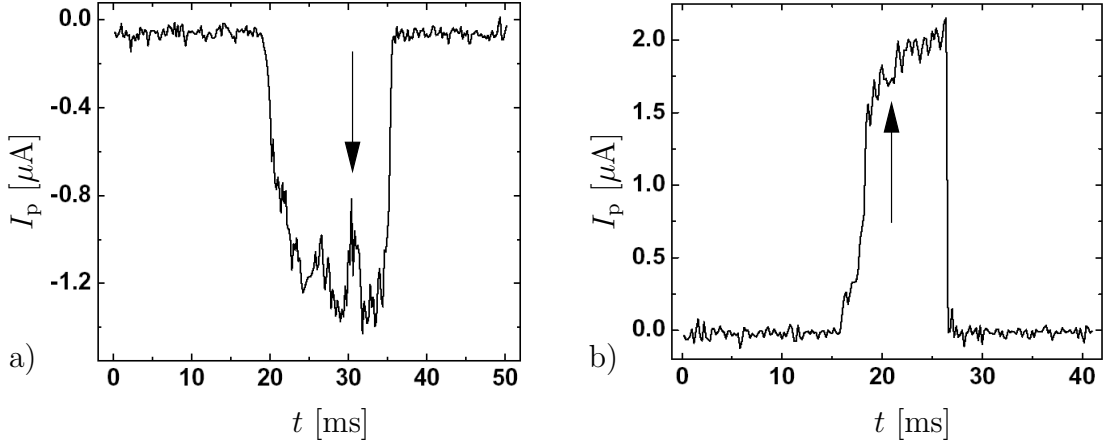


Figure 4.14: Switching current  $I_p$  for domain wall movement from the starting position to the dashed line in Fig. 4.13. Reprinted from UTSCHIG (2005) and SCHRADE ET AL. (2007a).

of magnitude smaller than that of the material (the parameters  $\mathbf{e}$ ,  $\boldsymbol{\varepsilon}^0$ , and  $\mathbf{P}^0$  vanish). Otherwise, the problem data is the same as in the previous simulations.

Fig. 4.15 shows two plots of the driving force  $\tau_n$  acting on a domain wall which approaches the defect from the right. In the central region, where the defect is located, the driving force opposes further domain wall movement. Near its boundaries, the interface is strongly attracted toward the defect compared to the defect-free case. The average resulting driving force for interface positions in front of the defect is almost identical to the one shown in Fig. 4.7, excluding  $x_S = 0$ ;  $T_n$  is equal to the value which is obtained for the defect-free case.

When the interface reaches the defect, it is split into an upper and a lower part. Since the problem is symmetric with respect to the central horizontal axis, these parts can be treated as one single entity. Figure 4.16 shows the driving force for interface positions to the right and to the left of the center of the defect. Once the domain wall enters the defect region, it is driven further to the left due to the high values of  $\tau_n$ ; further movement leads to opposing contributions in  $\tau_n$ . The corresponding values for  $T_n$  are shown in Fig. 4.17. Given the threshold  $T_0$ , the domain wall comes to a halt at approximately  $x_S = -30 \mu\text{m}$ . This result seems to contradict the experimental result of an almost undisturbed domain wall motion. However, the modeled defect extends fully in the  $x_3$ -direction, which increases its effect on the interface movement. A simulation with a more realistic defect geometry could reveal that the domain wall can pass a side effect without being pinned.

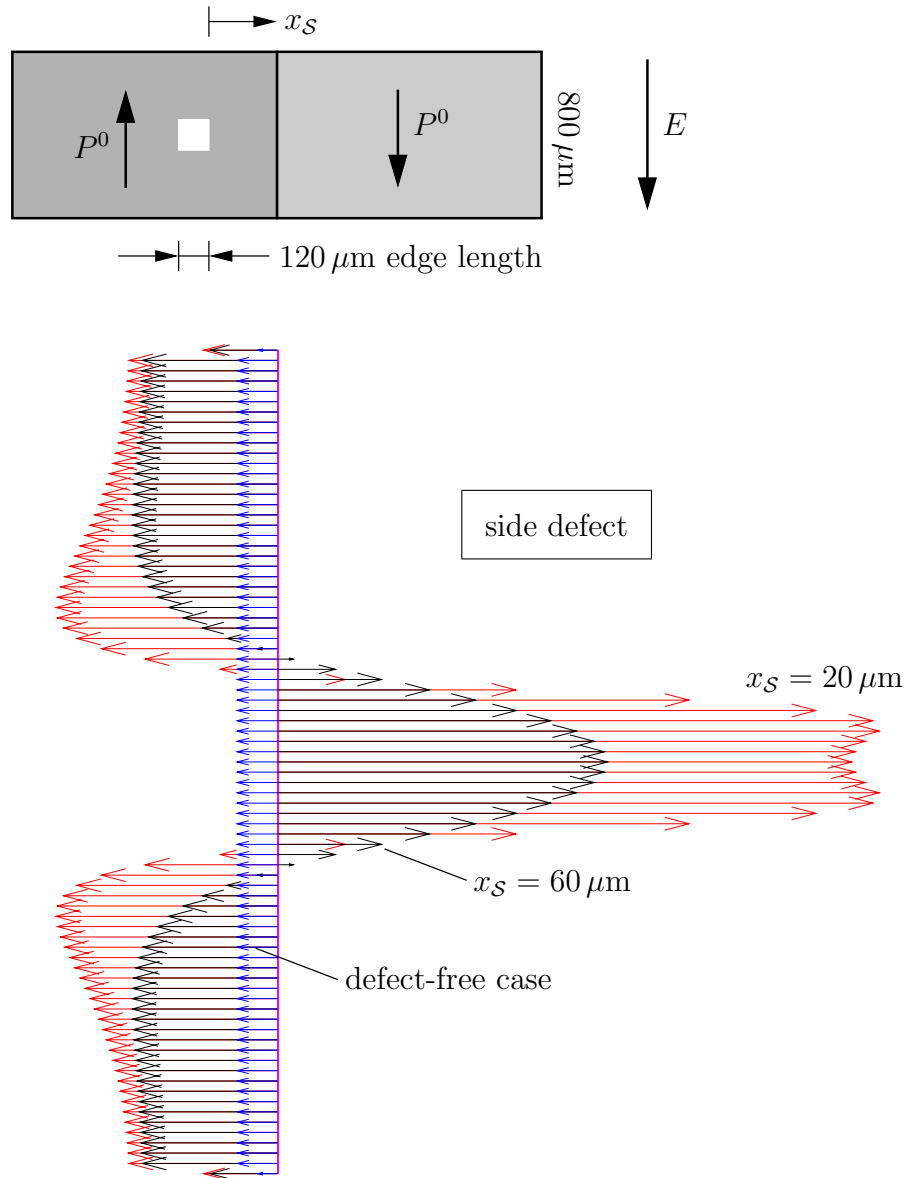


Figure 4.15: Distribution of  $\tau_n$  for interface positions in front of the side defect in comparison to the defect-free case. Although  $\tau_n$  varies strongly over the domain wall, the resulting values for  $T_n$  are the same as for the defect-free case.

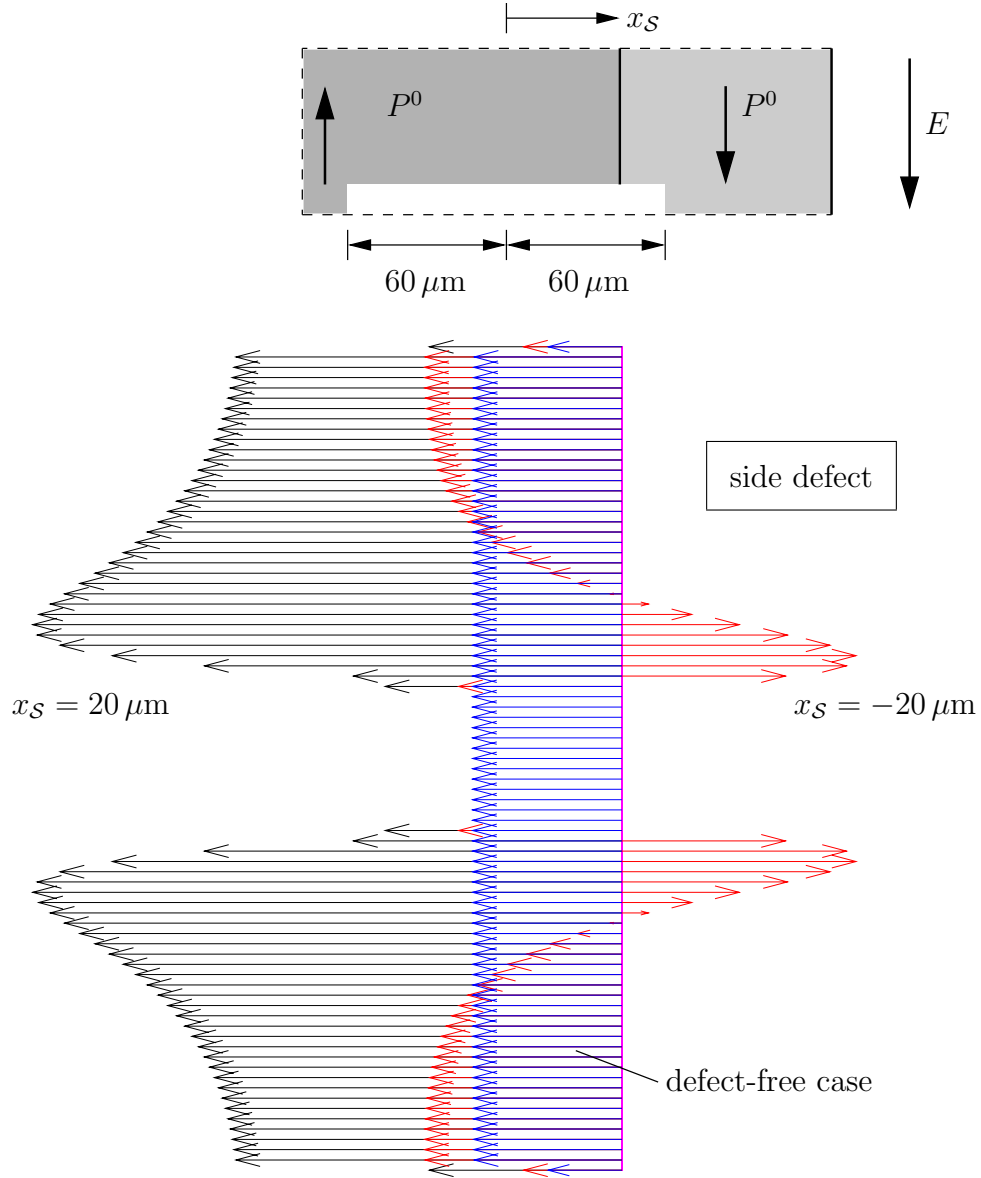


Figure 4.16: Distribution of  $\tau_n$  for interface positions located in the region of the side defect; comparison to the defect-free case. As the domain wall travels past the center of the defect, the driving force gains partly repulsive contributions; the values for  $T_n$  are plotted in Fig. 4.17.

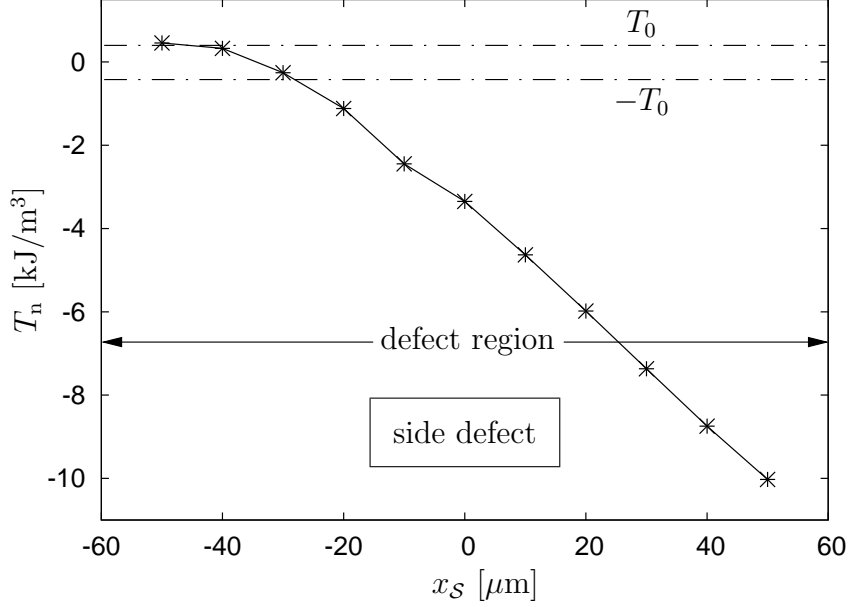


Figure 4.17:  $T_n$  as a function of the interface position  $x_S$ , cf. Fig. 4.16. Contrary to experimental observations, the domain wall is pinned in the 2d simulation before it can escape the defect region.

### 4.3.3 Polarization defect

A polarization defect is characterized by a region of “frozen” spontaneous polarization in which switching is impossible; this has been observed in PZT thin films in the context of electrical fatigue (cf. GRUVERMAN ET AL. 1996, COLLA ET AL. 1998). In this section, the effect of a polarization defect on a moving domain wall is investigated. The defect is assumed to have the same spontaneous strain as the surrounding material and the isotropic permittivity  $\epsilon^{\text{def}} = \epsilon_{11}\mathbf{1}$ , cf. Eq. (4.25)<sub>2</sub>. Except for the defect, the same simulation parameters as in the previous simulations are used.

Figure 4.18 shows the driving force on a defect with the defect polarization  $\mathbf{P}^{\text{def}} = \mathbf{0}$ . The defect has a significant influence on the values of  $\tau_n$  in the central region of the interface. However, the contributions of  $\tau_n$  driving the interface toward the defect are stronger as compared with the defect-free case. In Fig. 4.19, the driving force  $\tau_n$  is plotted for two domain wall positions in the defect region. The interface is strongly driven further to the left for  $x_S = 20 \mu\text{m}$ . Continued movement in that direction leads to increasing opposing contributions in  $\tau_n$ , which eventually leads to domain wall pinning before the end of the defect is reached. This is illustrated in Fig. 4.20, where  $T_n$  is plotted against the interface position

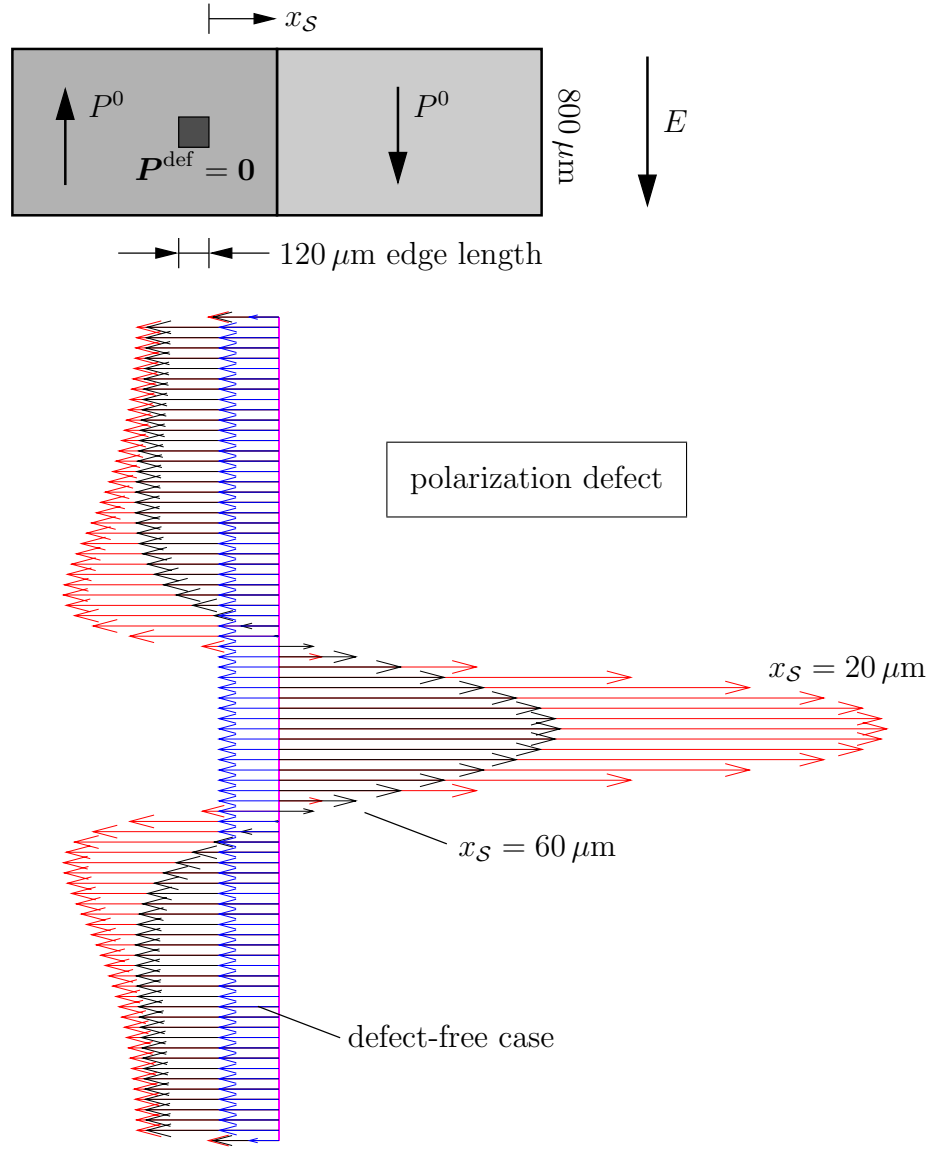


Figure 4.18: Distribution of  $\tau_n$  for interface positions in front of the polarization defect in comparison to the defect-free case. The central part of the domain wall is repelled by the defect while outer portions are attracted. Yet the values for  $T_n$  are the same as for the defect-free case.



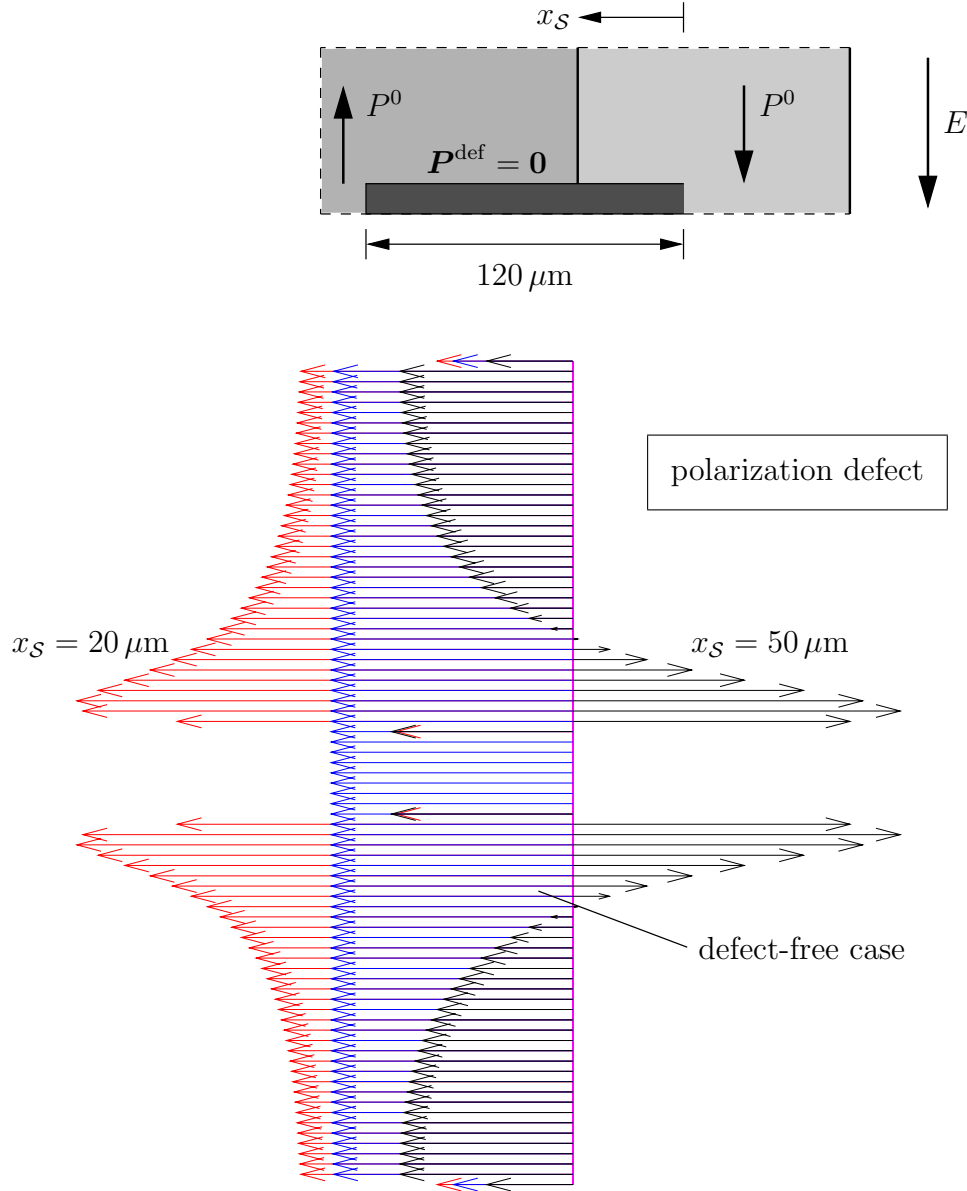


Figure 4.19: Distribution of  $\tau_n$  for interface positions “inside” the polarization defect in comparison to the defect-free case. Upon entering the defect area, the domain wall is driven further to the left; for  $x_S = 50 \mu\text{m}$ ,  $\tau_n$  exhibits repelling contributions. Averaged driving forces are shown in Fig. 4.20.

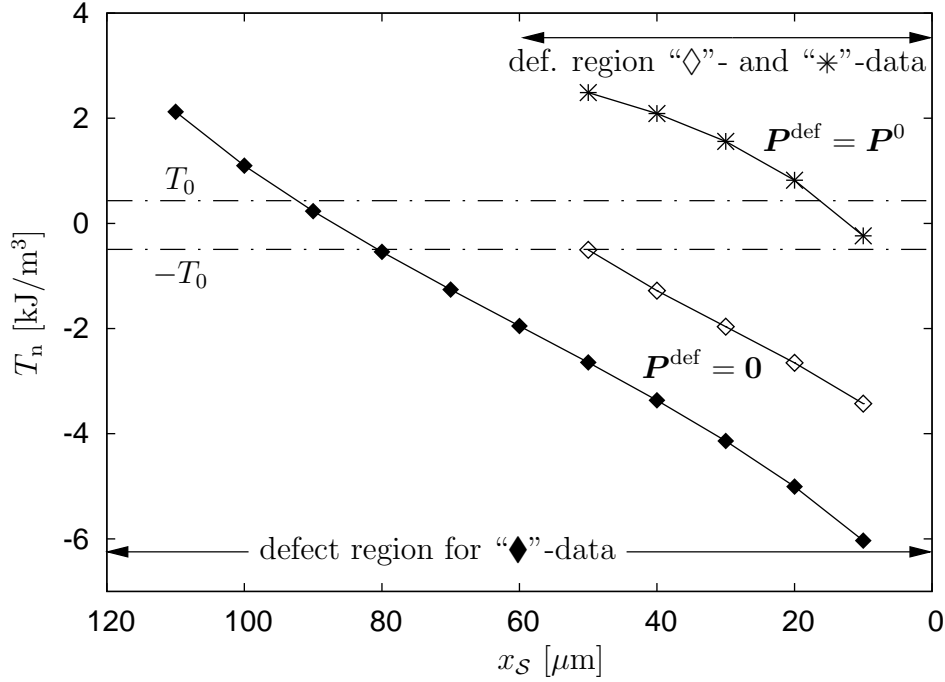


Figure 4.20:  $T_n$  as a function of the interface position  $x_S$  for polarization defect with dimensions  $120 \mu\text{m} \times 120 \mu\text{m}$  (“ $\blacklozenge$ ”-data) and  $60 \mu\text{m} \times 60 \mu\text{m}$  (“ $\diamond$ ”- and “ $*$ ”-data). For the defects with  $P^{\text{def}} = 0$ , the domain wall is pinned before it reaches the end of the defect; the smaller defect has a considerably lower influence to the domain wall movement. The defect with non-switchable polarization also has a pinning effect which sets in just as the domain wall reaches the defect.

for differently parametrized defects. The large defect corresponds to the plots in Figs. 4.18 and 4.19. Given the threshold value  $T_0$ , the domain wall comes to a stop after it has passed  $2/3$  of the width of the defect. The central curve in Fig. 4.20 refers to a defect with the same properties but half the edge length, i.e.  $60 \mu\text{m} \times 60 \mu\text{m}$ . Just before the end of the defect is reached,  $T_n$  reaches the threshold field, and thus the domain wall halts at that position. Yet the effect of the smaller defect is considerably weaker as opposed to that of the large defect. The upper curve in Fig. 4.20 results for a defect with the non-switchable polarization  $P^{\text{def}} = P^0$ , which coincides with the spontaneous polarization of the surrounding bulk material. The data points show that the domain wall is pinned just upon reaching the defect area.

# Chapter 5

## Phase field approach

While the singular surface model introduced in Ch. 4 relies on the physically sound and well-established theory of linear piezoelectricity and can be implemented with standard numerical techniques, there are conceptual and practical concerns regarding its general applicability to microstructure evolution. First, the tracking of (curved) interfaces can become objectionably cumbersome, especially given that changing interfaces may require continuous remeshing. Second, the development of a physically motivated and methodologically solid and systematic concept defining rules regarding changes in the topology of the microstructure such as merging, separating, spawning, or vanishing interfaces is not easily achieved if at all possible.

These difficulties can be circumvented by employing an order parameter or phase field concept in which discontinuities are regularized by introducing a (twice continuously) differentiable order parameter. The order parameter is homogeneous within “pure” phases and changes rapidly in interfacial regions. Its temporal evolution is derived from thermodynamic considerations and leads to a time-dependent generalized Ginzburg-Landau equation. Thus changes in the topology are the result of the evolution of an order parameter, and no explicit interface tracking or remeshing is required. On the other hand, a continuously changing order parameter necessitates the formulation of material constants continuously varying from one phase to another. This means that one has to make assumptions about the electromechanical properties *inside* a domain wall. Given that ferroelectric domain walls are typically the size of a few unit cell lengths, continuously changing material parameters cannot capture the situation on that length scale, and the specification of the parameters in the interface is somewhat ambiguous.

## 5.1 Theory

A considerable number of publications on the subject of Ginzburg-Landau type phase field models for ferroelectric phase transitions have accumulated over the past decades. The proposed models vary in many respects, e.g. regarding the choice of order parameter, the number of free variables in the free energy, the type of electromechanical coupling, the numerical implementation, and other details in the model formulation. In CAO & BARSCH (1990) and CAO ET AL. (1990), the order parameter is taken to be the rotation angle of  $BX_6$  octahedra in  $ABX_3$  perovskite structures; CAO & CROSS (1991) use the material polarization as the order parameter. These models are based on a free energy function which comprises the Landau-Devonshire free energy<sup>1</sup>, the order parameter gradient energy, a quadratic elastic potential, and a coupling energy accounting for the electrostrictive effect. Since the electric field problem is not solved and the strain is expressed in terms of the order parameter, the order parameter appears as the only free variable. These publications present quasi-1d analytic solutions for the order parameter profile and for the strain distribution in context with static 180° and 90° ferroelectric twin boundaries. An extension of this model formulation for 2d and 3d domain structure evolution is presented in HU & CHEN (1997), WANG ET AL. (2004), and HU & CHEN (1998) where, by adding another term to the free energy, the dipole-dipole interaction for inhomogeneous polarization states is considered. The mechanical equilibrium and Ginzburg-Landau equation are solved with a semi-implicit Fourier spectral method. The same approach is taken in AHLUWALJA & CAO (2000) and AHLUWALJA & CAO (2003), where the free energy is extended to allow for an applied external electric field.

In AHLUWALJA ET AL. (2005), CHOUDHURY ET AL. (2005), ZHANG & BHATTACHARYA (2005), and CHOUDHURY ET AL. (2007), the electric field problem is incorporated, and the equations are solved numerically with Fourier methods. Finite element implementations of the complete set of equations have been published in SU & LANDIS (2007) and WANG & KAMLAH (2008).

In contrast to the phase field models in ZHANG & BHATTACHARYA (2005) and SU & LANDIS (2007), where the *material* polarization is used as the order parameter, the present theory is based on the *spontaneous* polarization as the order parameter.<sup>2</sup> This primary difference in the model formulation implicates constitu-

---

<sup>1</sup>Cf. DEVONSHIRE (1949) and DEVONSHIRE (1954).

<sup>2</sup>The term *spontaneous polarization* usually refers to the polarization of the spontaneously polarized phase in the absence of external loading. Within the order parameter concept, the spontaneous polarization is allowed to vary continuously in space.

tive assumptions regarding the form of electromechanical coupling. If the material polarization is used as the order parameter, the necessary inclusion of the dielectric and piezoelectric behavior in the order parameter thwarts any attempt to formulate explicitly a linear dielectric or piezoelectric constitutive relation. Consequently, the thermodynamic potential can only approximate these properties near the polarized states. As another consequence, the mechanical and electrical field equations, i.e. the mechanical and electric equilibrium conditions, remain uncoupled in the strain and the electric field; coupling is achieved only through the order parameter. The present choice of order parameter, however, allows for a fully electromechanically coupled model formulation. The conceptual differences between the present model and the models presented in ZHANG & BHATTACHARYA (2005) and SU & LANDIS (2007) are discussed in App. A.2. Phase field models based on the spontaneous polarization as the order parameter can be found e.g. in SCHRADE ET AL. (2007b), SCHRADE ET AL. (2009), and SCHRADE ET AL. (2008).

### 5.1.1 Thermodynamics

Within the order parameter approach, the electric enthalpy or *phase field potential* is assumed to depend on the spontaneous polarization and its gradient, i.e.

$$H = \tilde{H}(\boldsymbol{\varepsilon}, \mathbf{E}, \mathbf{P}, \nabla \mathbf{P}) , \quad (5.1)$$

where the spontaneous polarization is now denoted by  $\mathbf{P}$ . The Ginzburg-Landau evolution law for  $\mathbf{P}$  can be derived directly from the internal dissipation inequality (3.140), see App. A.3 for details. A more general thermodynamic framework, which is adopted here, can be found in FRIED & GURTIN (1993), FRIED & GURTIN (1994), and GURTIN (1996). In these publications, the introduction of a new independent field variable, i.e. the order parameter, is accompanied by the postulate that there exists a second order micro-force stress tensor  $\tilde{\boldsymbol{\Sigma}}$  which is thermodynamically conjugate to the rate of change of the order parameter. Furthermore, an *external* volume micro-force  $\boldsymbol{\zeta}$  is introduced. Then the integral form of the second law reads

$$\begin{aligned} \int_{\partial \mathcal{B}} \left( (\boldsymbol{\sigma} \mathbf{n}) \cdot \dot{\mathbf{u}} - (\mathbf{D} \cdot \mathbf{n}) \dot{\varphi} + (\tilde{\boldsymbol{\Sigma}} \mathbf{n}) \cdot \dot{\mathbf{P}} \right) da + \int_{\mathcal{B}} \left( \mathbf{f} \cdot \dot{\mathbf{u}} - \rho \dot{\varphi} + \boldsymbol{\zeta} \cdot \dot{\mathbf{P}} \right) dv \\ - \frac{d}{dt} \int_{\mathcal{B}} \tilde{H}(\boldsymbol{\varepsilon}, \mathbf{E}, \mathbf{P}, \nabla \mathbf{P}) dv \geq 0 . \end{aligned} \quad (5.2)$$

The second underlying assumption is the balance of micro-forces

$$\int_{\partial \mathcal{B}} \tilde{\boldsymbol{\Sigma}} \mathbf{n} da + \int_{\mathcal{B}} (\boldsymbol{\zeta} + \tilde{\mathbf{g}}) dv = \mathbf{0} , \quad (5.3)$$

where  $\tilde{\mathbf{g}}$  is the *internal* micro-force, which does not enter the inequality (5.2). Since Eq. (5.3) must hold for any sub-volume of  $\mathcal{B}$ , one obtains

$$\operatorname{div} \tilde{\Sigma} + \zeta + \tilde{\mathbf{g}} = \mathbf{0} . \quad (5.4)$$

With (3.133), (3.135) and (5.4), the local form of the second law reads

$$\boldsymbol{\sigma} \cdot \dot{\boldsymbol{\varepsilon}} - \mathbf{D} \cdot \dot{\mathbf{E}} + \tilde{\Sigma} \cdot \dot{\overline{\nabla \mathbf{P}}} - \tilde{\mathbf{g}} \cdot \dot{\mathbf{P}} - \dot{\tilde{H}}(\boldsymbol{\varepsilon}, \mathbf{E}, \mathbf{P}, \nabla \mathbf{P}) \geq 0 \quad (5.5)$$

or, equivalently,

$$\left( \boldsymbol{\sigma} - \frac{\partial \tilde{H}}{\partial \boldsymbol{\varepsilon}} \right) \cdot \dot{\boldsymbol{\varepsilon}} - \left( \mathbf{D} + \frac{\partial \tilde{H}}{\partial \mathbf{E}} \right) \cdot \dot{\mathbf{E}} + \left( \tilde{\Sigma} - \frac{\partial \tilde{H}}{\partial \nabla \mathbf{P}} \right) \cdot \dot{\overline{\nabla \mathbf{P}}} - \left( \tilde{\mathbf{g}} + \frac{\partial \tilde{H}}{\partial \mathbf{P}} \right) \cdot \dot{\mathbf{P}} \geq 0 . \quad (5.6)$$

The following constitutive equations are derived from this inequality:<sup>3</sup>

$$\boldsymbol{\sigma} = \frac{\partial \tilde{H}}{\partial \boldsymbol{\varepsilon}} , \quad \mathbf{D} = - \frac{\partial \tilde{H}}{\partial \mathbf{E}} , \quad \tilde{\Sigma} = \frac{\partial \tilde{H}}{\partial \nabla \mathbf{P}} . \quad (5.7)$$

The remaining dissipation inequality then reads

$$- \underbrace{\left( \tilde{\mathbf{g}} + \frac{\partial \tilde{H}}{\partial \mathbf{P}} \right)}_{\tilde{\mathbf{g}}_{\text{dis}}} \cdot \dot{\mathbf{P}} \geq 0 . \quad (5.8)$$

It can be shown<sup>4</sup> that the most general solution for  $\tilde{\mathbf{g}}_{\text{dis}}$  is given by

$$\tilde{\mathbf{g}}_{\text{dis}} = -\boldsymbol{\beta} \dot{\mathbf{P}} , \quad (5.9)$$

where  $\boldsymbol{\beta}$  is a constitutive positive semi-definite second order *inverse mobility tensor*. The dissipation can then be expressed by

$$\mathcal{D} = -\tilde{\mathbf{g}}_{\text{dis}} \cdot \dot{\mathbf{P}} = \dot{\mathbf{P}} \cdot (\boldsymbol{\beta} \dot{\mathbf{P}}) . \quad (5.10)$$

The evolution law for the order parameter is obtained from Eq. (5.9) by making use of the balance law (5.4):

$$\boldsymbol{\beta} \dot{\mathbf{P}} = \operatorname{div} \tilde{\Sigma} + \zeta - \frac{\partial \tilde{H}}{\partial \mathbf{P}} . \quad (5.11)$$

With the assumption that  $\zeta = \mathbf{0}$  and on use of Eq. (5.7)<sub>3</sub>, this gives a time-dependent Ginzburg-Landau type evolution law:

$$\boldsymbol{\beta} \dot{\mathbf{P}} = \operatorname{div} \frac{\partial \tilde{H}}{\partial \nabla \mathbf{P}} - \frac{\partial \tilde{H}}{\partial \mathbf{P}} . \quad (5.12)$$

---

<sup>3</sup>Cf. COLEMAN & NOLL (1963).

<sup>4</sup>See GURTIN (1996).

### 5.1.2 Phase field potential

The phase field potential  $\tilde{H}$  is additively split into three parts:<sup>5</sup> a modified electric enthalpy  $\tilde{H}^{\text{ent}}$ , the phase separation potential  $\tilde{H}^{\text{sep}}$ , and the interface gradient energy  $\tilde{H}^{\text{int}}$ , i.e.

$$H = \tilde{H}^{\text{ent}}(\boldsymbol{\varepsilon}, \mathbf{E}, \mathbf{P}) + \tilde{H}^{\text{sep}}(\mathbf{P}) + \tilde{H}^{\text{int}}(\nabla \mathbf{P}) \quad (5.13)$$

with

$$\tilde{H}^{\text{ent}} = \frac{1}{2} (\boldsymbol{\varepsilon} - \boldsymbol{\varepsilon}^0) \cdot [\mathbb{C} (\boldsymbol{\varepsilon} - \boldsymbol{\varepsilon}^0)] - (\boldsymbol{\varepsilon} - \boldsymbol{\varepsilon}^0) \cdot \mathfrak{e}^T \mathbf{E} - \frac{1}{2} \mathbf{E} \cdot \boldsymbol{\epsilon} \mathbf{E} - \mathbf{P} \cdot \mathbf{E} , \quad (5.14)$$

$$\tilde{H}^{\text{sep}} = \kappa_s \frac{\gamma}{\epsilon} \tilde{\psi}(\mathbf{P}) , \quad (5.15)$$

$$\tilde{H}^{\text{int}} = \frac{1}{2} \kappa_i \frac{\gamma \epsilon}{P_0^2} \|\nabla \mathbf{P}\|^2 . \quad (5.16)$$

The material tensors  $\mathbb{C}$ ,  $\mathfrak{e}$ , and  $\boldsymbol{\epsilon}$  denote the elastic stiffness, the piezoelectric coupling constants, and the dielectric tensor, respectively. These material parameters generally depend on the polarization state, i.e. on the order parameter. In Sec. 5.1.3, the constants  $\gamma$  and  $\epsilon$  are identified as the characteristic energy density and the characteristic length of an interface, respectively. The constant  $P_0$  designates the spontaneous polarization of the unloaded ferroelectric phase and defines the minima of the phase separation potential (see below). The parameters  $\kappa_s$  and  $\kappa_i$  are dimensionless calibration constants (see Sec. 5.1.3).

In this work, only tetragonal unit cells are considered. This poses a restriction insofar as ferroelectric materials can also be e.g. of orthorhombic (e.g. lead zirconate) or rhombohedral (e.g. PZT with high Zr content) structure. Ferroelectrics with tetragonal structure include barium titanate, lead titanate, and PZT with high Ti content. These materials exhibit anisotropy and phase dependence in the elastic stiffness and the dielectric constants.<sup>6</sup> By the assumption that the mechanical and the dielectric anisotropy are of minor importance for the phase transition, the elastic stiffness and the dielectric tensor are assumed to be isotropic and thus independent of  $\mathbf{P}$ , i.e.

$$\mathbb{C} = \text{const.} \quad \text{and} \quad \boldsymbol{\epsilon} = \epsilon_{11} \mathbf{1} . \quad (5.17)$$

An extension to anisotropic elastic or dielectric behavior can be implemented in the model in a straightforward way.

The piezoelectric tensor  $\mathfrak{e}$ , however, strongly depends on the poling state and is of great importance in the phase transitions. With reference to KAMLAH (2001),

<sup>5</sup>Cf. SCHRADE ET AL. (2007b).

<sup>6</sup>See e.g. XU (1991).

transversely isotropic piezoelectric conditions are assumed; the axis of anisotropy coincides with the direction of poling. With respect to Cartesian coordinates, the following representation is used:

$$\begin{aligned} \mathbb{E}_{kij}(\mathbf{P}) = \left( \frac{|\mathbf{P}|}{P_0} \right)^\nu & \left\{ b_{\parallel} e_i e_j e_k + b_{\perp} (\delta_{ij} - e_i e_j) e_k \right. \\ & \left. + b_{=} \frac{1}{2} [(\delta_{ki} - e_k e_i) e_j + (\delta_{kj} - e_k e_j) e_i] \right\}, \end{aligned} \quad (5.18)$$

where  $\mathbf{e} = \mathbf{P}/|\mathbf{P}|$  is the direction of poling and  $b_{\parallel}$ ,  $b_{\perp}$ , and  $b_{=}$  are independent scalar material constants. The exponent  $\nu$  determines the smoothness of  $\tilde{H}^{\text{ent}}$  at the point  $\mathbf{P} = \mathbf{0}$ . With  $\nu = 3$ , which is used in the simulations, the second partial derivatives of  $\tilde{H}^{\text{ent}}$  with respect to  $\mathbf{P}$  exist and are continuous at every point.<sup>7</sup>

The spontaneous strain  $\boldsymbol{\varepsilon}^0$  is constructed to be purely deviatoric. This is justified by the observation that domain switching processes are volume preserving on the macroscopic level.<sup>8</sup> The spontaneous strain is thus expressed by

$$\boldsymbol{\varepsilon}^0(\mathbf{P}) = \frac{3}{2} \varepsilon^0 \left( \frac{|\mathbf{P}|}{P_0} \right)^2 \left\{ \mathbf{e} \otimes \mathbf{e} - \frac{1}{3} \mathbf{1} \right\}, \quad (5.19)$$

where  $\varepsilon^0$  is the spontaneous strain of the unloaded ferroelectric phase. The value of  $\varepsilon^0$  is to be determined with respect to the paraelectric cubic phase.<sup>9</sup>

In the 1d case, the phase separation potential has the form of a double-well potential, allowing for two minima which correspond to the two distinct states of the ferroelectric phase. The general 3d case has to account for the six variants of spontaneous polarization of the tetragonal unit cell. Since the six states are energetically indistinguishable, the energy landscape  $\tilde{\psi}$  has to be invariant in  $\pm P_i$ ,  $i = 1, 2, 3$ .<sup>10</sup> This is commonly achieved with a fourth- or higher-order polynomial in  $P_i$ . For the 2d case, which is considered here, the following eighth-order polynomial allows for a flexible adjustment of the energy landscape:

$$\begin{aligned} \tilde{\psi} = 1 & + \frac{a_1}{P_0^2} (P_1^2 + P_2^2) + \frac{a_2}{P_0^4} (P_1^4 + P_2^4) + \frac{a_3}{P_0^4} P_1^2 P_2^2 \\ & + \frac{a_4}{P_0^6} (P_1^6 + P_2^6) + \frac{a_5}{P_0^6} (P_1^4 P_2^2 + P_2^4 P_1^2) \\ & + \frac{a_6}{P_0^8} (P_1^8 + P_2^8) + \frac{a_7}{P_0^8} P_1^4 P_2^4 \\ & + \frac{a_8}{P_0^8} (P_1^6 P_2^2 + P_2^6 P_1^2). \end{aligned} \quad (5.20)$$

<sup>7</sup>Lower values for  $\nu$  lead to numerical intricacies regarding the positive definiteness of the global tangent matrix and should thus be avoided.

<sup>8</sup>Cf. KAMLAH (2001).

<sup>9</sup>See Sec. 5.3.

<sup>10</sup>Cf. BHATTACHARYA & RAVICHANDRAN (2003).



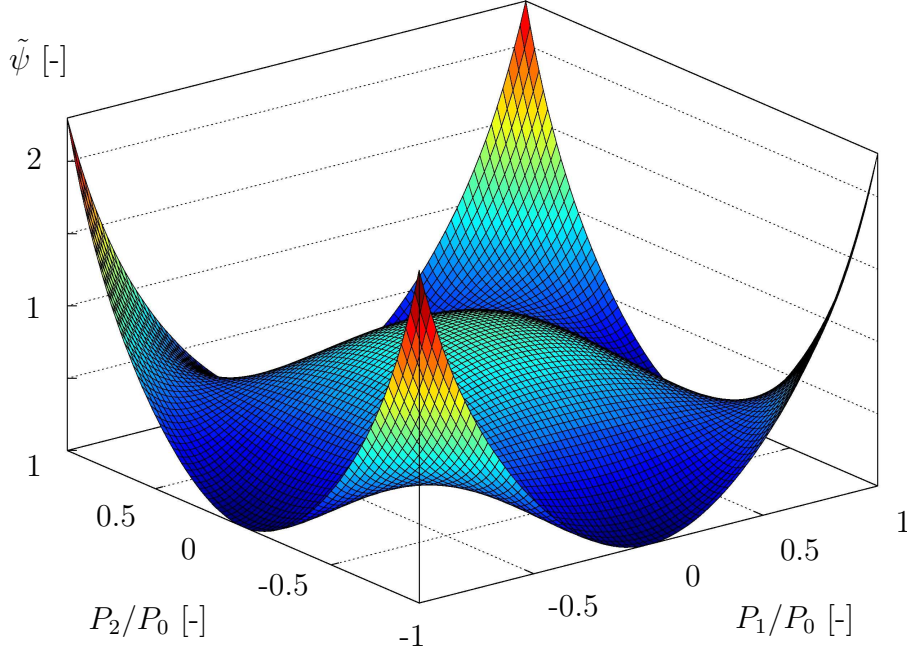


Figure 5.1: Phase separation potential with minima at  $\mathbf{P} = (\pm P_0, 0)$  and  $\mathbf{P} = (0, \pm P_0)$  corresponding to the four spontaneously polarized states of the tetragonal unit cell in 2d.

This energy is normalized in the way that  $\tilde{\psi}(0,0) = 1$ ,  $\partial_{P_i}\tilde{\psi}(\pm P_0, 0) = 0$ , and  $\partial_{P_i}\tilde{\psi}(0, \pm P_0) = 0$  for  $i = 1, 2$ . The coefficients  $a_i$  are dimensionless and define the shape of  $\tilde{\psi}$ , which is illustrated in Figure 5.1. For a detailed account on the calculation of the coefficients  $a_i$ , see App. A.4.

### Constitutive equations

The specification of  $\tilde{H}$  allows for a statement of the constitutive equations. Evaluation of Eq. (5.7) yields

$$\boldsymbol{\sigma} = \mathbb{C} (\boldsymbol{\varepsilon} - \boldsymbol{\varepsilon}^0) - \mathbf{e}^T \mathbf{E} , \quad (5.21)$$

$$\mathbf{D} = \mathbf{e} (\boldsymbol{\varepsilon} - \boldsymbol{\varepsilon}^0) + \boldsymbol{\epsilon} \mathbf{E} + \mathbf{P} , \quad (5.22)$$

$$\tilde{\boldsymbol{\Sigma}} = \kappa_i \frac{\gamma \epsilon}{P_0^2} \nabla \mathbf{P} . \quad (5.23)$$

Further evaluation of Eq. (5.12) yields the evolution equation for  $\mathbf{P}$ :

$$\beta \dot{\mathbf{P}} = \kappa_i \frac{\gamma \epsilon}{P_0^2} \Delta \mathbf{P} - \kappa_s \frac{\gamma}{\epsilon} \frac{\partial \tilde{\psi}}{\partial \mathbf{P}} - \frac{\partial \tilde{H}^{\text{ent}}}{\partial \mathbf{P}} . \quad (5.24)$$

Finally, the boundary conditions (3.143) are to be completed with

$$\begin{aligned} \mathbf{P} - \mathbf{P}^* &= \mathbf{0} \quad \text{on } \partial\mathcal{B}_P, \\ \tilde{\Sigma}\mathbf{n} - \boldsymbol{\pi}^* &= \mathbf{0} \quad \text{on } \partial\mathcal{B}_\pi. \end{aligned} \quad (5.25)$$

The determination of the boundary conditions for the order parameter is not a trivial task. While the physical interpretation of (5.25)<sub>1</sub> is straightforward, the Neumann type condition (5.25)<sub>2</sub> should be discussed in more detail. With Eq. (5.23) the condition states that

$$\nabla \mathbf{P} \mathbf{n} = \frac{P_0^2}{\kappa_i \gamma \epsilon} \boldsymbol{\pi}^* \quad \text{on } \partial\mathcal{B}_\pi, \quad (5.26)$$

which means that the gradient of  $\mathbf{P}$  in the normal direction is prescribed by the right hand side of (5.26). In the following the condition

$$\boldsymbol{\pi}^* = \mathbf{0} \quad \text{on } \partial\mathcal{B} \quad (5.27)$$

is used, forcing domain walls to be normal to the boundary  $\partial\mathcal{B}$ . This choice is appropriate for the geometries of the 180° and 90° domain wall settings simulated in Secs. 5.3.2–5.3.3 as well as the microstructures examined in Secs. 5.3.5–5.3.6. The effect of this boundary condition can be seen quite clearly in Fig. 5.24 where all domain walls remain normal to the boundary.

### 5.1.3 Phase field parameters

This section provides a motivation for the introduction of the material parameters  $\gamma$  and  $\epsilon$  first introduced in Eqs. (5.15) and (5.16); cf. the parameter  $\gamma$  in the context of sharp interface models in Sec. 3.4 and 4.1.

#### Interface energy and width

Employing a simplified 1d model, one can show that  $\gamma$  and  $\epsilon$  are the characteristic specific energy and the characteristic width of the interface, respectively. Specifically, the calibration constants  $\kappa_s$  and  $\kappa_i$  are used to identify  $\gamma$  with the specific energy of a 180° domain wall and  $\epsilon$  with its width.

The starting point of the 1d model is a region with two domains separated by a 180° domain wall under load-free conditions as depicted in Fig. 4.3. By neglecting the  $x_2$ -direction and naming  $x = x_1$ , the order parameter profile for this configuration has the form shown in Fig. 5.2. Furthermore, it is assumed that the

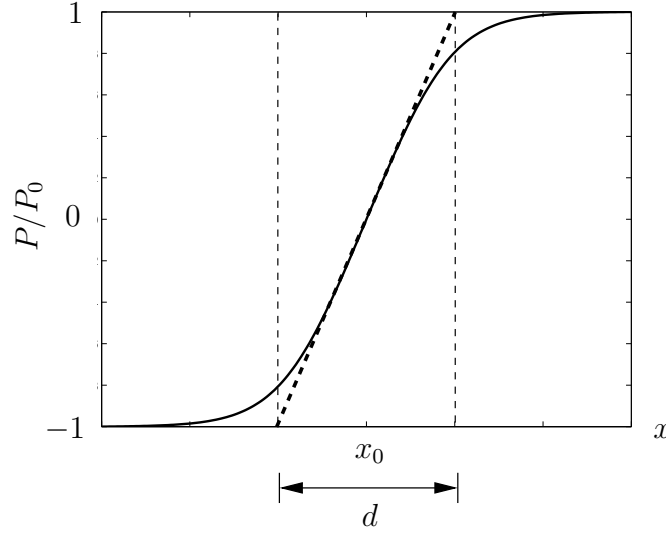


Figure 5.2: Order parameter profile for a  $180^\circ$  interface in the 1d model. The domain wall width  $d$  is defined via the slope of  $P(x)$  at the point where  $P(x_0) = 0$ .

energy  $\tilde{H}^{\text{sep}} + \tilde{H}^{\text{int}}$  outweighs  $\tilde{H}^{\text{ent}}$  in the interface region. Thus, by neglecting the contribution from  $\tilde{H}^{\text{ent}}$ , the model reduces to

$$\tilde{h}(P, P') = \kappa_s \frac{\gamma}{\epsilon} \tilde{\Psi}(P) + \frac{1}{2} \kappa_i \frac{\gamma \epsilon}{P_0^2} (P')^2 = \tilde{h}^s(P) + \tilde{h}^i(P'), \quad (5.28)$$

where  $\tilde{\Psi}(P) = \tilde{\psi}(P, 0)$  and  $(\cdot)' = \frac{d}{dx}(\cdot)$ . Figure 5.3 shows the typical double well potential for the 1d separation potential  $\tilde{\Psi}$  with minima at  $P = \pm P_0$ . The total energy of the system, which is minimal in equilibrium states, is given by

$$W = \int_{-\infty}^{+\infty} \tilde{h}(P, P') dx \stackrel{!}{=} \min. \quad (5.29)$$

For the boundary conditions  $\lim_{x \rightarrow \pm\infty} P(x) = \pm P_0$ , the solution of this optimization problem yields a configuration with just one interface, i.e. the domain configuration under consideration. With reference to the approach in CAHN & HILLIARD (1958), the Euler-Lagrange equation is applied to Eq. (5.29):

$$\frac{\partial \tilde{h}}{\partial P} - \frac{d}{dx} \frac{\partial \tilde{h}}{\partial P'} = 0. \quad (5.30)$$

Separation of variables and subsequent integration gives

$$\tilde{h}^s = \tilde{h}^i = \frac{1}{2} \kappa_i \frac{\gamma \epsilon}{P_0^2} (P')^2. \quad (5.31)$$

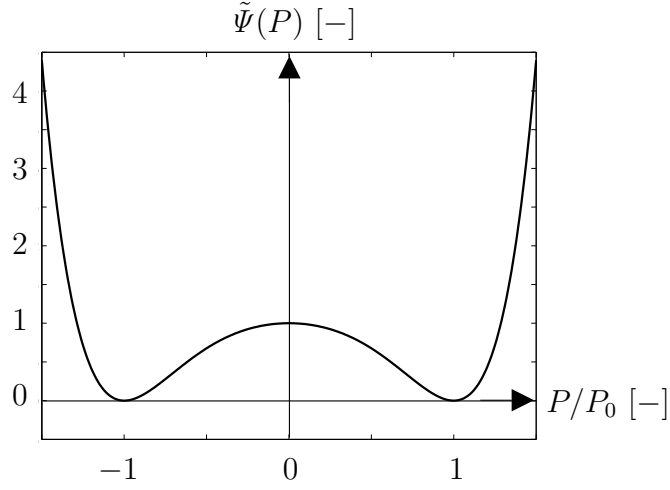


Figure 5.3: 1d phase separation potential  $\tilde{\Psi}$  with minima at  $P = \pm P_0$ .

With this result, the minimized energy of the system can be expressed by

$$\begin{aligned}
 W &= \int_{-\infty}^{+\infty} \tilde{h}(P, P') dx = \int_{-\infty}^{+\infty} 2\tilde{h}^s(P) dx \\
 &= \int_{-P_0}^{P_0} 2\kappa_s \frac{\gamma}{\epsilon} \tilde{\Psi}(P) \sqrt{\frac{\kappa_i}{2\kappa_s \tilde{\Psi}(P)}} \frac{\epsilon}{P_0} dP \\
 &= \sqrt{2\kappa_i \kappa_s} \gamma \int_{-1}^1 \sqrt{\tilde{\Psi}(\bar{P})} d\bar{P} ,
 \end{aligned} \tag{5.32}$$

where the integration is with respect to the normalized order parameter  $\bar{P} = P/P_0$  and  $\tilde{\Psi}(\bar{P}) = \tilde{\Psi}(P)$ . The energy  $W$  depends only on  $\kappa_i$ ,  $\kappa_s$ ,  $\gamma$ , and on the *shape* of the normalized phase separating potential, but not on the parameter  $\epsilon$ . Therefore the parameter  $\gamma$  can be identified with the energy  $W$ , i.e.

$$W = \sqrt{2\kappa_i \kappa_s} \gamma \int_{-1}^1 \sqrt{\tilde{\Psi}(\bar{P})} d\bar{P} \stackrel{!}{=} \gamma , \tag{5.33}$$

which gives the first equation for the solution of  $\kappa_i$  and  $\kappa_s$ :

$$\kappa_i \kappa_s = \frac{1}{2} \left( \int_{-1}^1 \sqrt{\tilde{\Psi}(\bar{P})} d\bar{P} \right)^{-2} . \tag{5.34}$$

With reference to Fig. 5.2, the domain wall width is defined as

$$d = \frac{2P_0}{|P'(x_0)|} , \quad P(x_0) = 0 . \tag{5.35}$$

Making use of the results previously obtained from the variation procedure, one obtains

$$d = \epsilon \sqrt{\frac{2\kappa_i}{\kappa_s}} . \tag{5.36}$$

Therefore the parameter  $\epsilon$  is identified with the domain wall width  $d$ , and  $d = \epsilon = \epsilon\sqrt{2\kappa_i/\kappa_s}$  leads to second equation for the determination of  $\kappa_i$  and  $\kappa_s$ :

$$\kappa_s = 2\kappa_i . \quad (5.37)$$

As indicated before, the integrals in (5.32) depend on the shape of  $\Psi$ , i.e. on the constants  $a_i$ . For a typical set of  $a_i$ , numerical integration gives

$$\mathcal{I} := \int_{-1}^1 \sqrt{\tilde{\Psi}(\bar{P})} d\bar{P} \approx 1.4 . \quad (5.38)$$

Finally, one obtains

$$\kappa_s = \mathcal{I}^{-1} \approx 0.71 \quad \text{and} \quad \kappa_i = \frac{1}{2} \mathcal{I}^{-1} \approx 0.35 . \quad (5.39)$$

The result may be summarized as follows: In a 1d setting, the parameters  $\gamma$  and  $\epsilon$  can be identified as the energy of the interface and its width, respectively, if the calibration coefficients  $\kappa_s$  and  $\kappa_i$  are chosen according to Eq. (5.39) and  $\tilde{H}^{\text{ent}}$  is neglected. This gives rise to an analogous formulation of the phase separation potential and the gradient energy in Eqs. (5.15) and (5.16), respectively. It is noted that in the 2d or 3d case,  $\gamma$  becomes the specific domain wall energy, whereas in 1d it is the interface energy itself. The values for  $\kappa_s$  and  $\kappa_i$  are kept for the 2d simulations in Sec. 5.3, and their suitability will be shown therein.

### Interface velocity

In the following, a system with two domains separated by a  $180^\circ$  domain wall, which is loaded with an electric field parallel to the domain wall, is considered. The previous 1d model is extended to include the electric field and thus becomes

$$\tilde{h} = \kappa_s \frac{\gamma}{\epsilon} \tilde{\Psi}(P) + \frac{1}{2} \kappa_i \frac{\gamma \epsilon}{P_0^2} (P')^2 - P E_{\text{app}} , \quad (5.40)$$

where  $E_{\text{app}}$  is the applied uniform electric field. Evaluation of the Ginzburg-Landau evolution equation gives

$$\beta \dot{P} = \kappa_i \frac{\gamma \epsilon}{P_0^2} P'' - \kappa_s \frac{\gamma}{\epsilon} \frac{d\tilde{\Psi}}{dP} + E_{\text{app}} . \quad (5.41)$$

The position of the domain wall  $x_d$  is defined by means of  $P(x_d, t) = 0$ , i.e. the middle of the interface. The domain wall velocity  $v_d$  is then defined as  $v_d = \frac{dx_d}{dt}$ , and a short calculation shows that

$$v_d = \frac{dx_d}{dt} = - \left. \frac{\dot{P}}{P'} \right|_{x_d} = - \frac{\epsilon}{2P_0} \left. \dot{P} \right|_{x_d} = - \frac{\epsilon}{2P_0} \beta^{-1} E_{\text{app}} . \quad (5.42)$$

In 1d, the domain wall velocity is therefore proportional to the applied electric field and to the width of the interface.

Evaluating the evolution equation at  $\mathbf{P} = \mathbf{0}$  in the 2d model gives

$$\dot{\mathbf{P}} \Big|_{\mathbf{P}=\mathbf{0}} = \beta^{-1} \mathbf{E} . \quad (5.43)$$

For an isotropic inverse mobility tensor  $\beta = \beta \mathbf{1}$ , the domain wall velocity in 2d is given by

$$v_d = \frac{\epsilon}{2P_0} \beta^{-1} E_{\parallel} = \beta_0^{-1} E_{\parallel} , \quad (5.44)$$

where  $E_{\parallel}$  is the electric field component parallel to the domain wall, and the inverse mobility is now written as

$$\beta^{-1} = \frac{2P_0}{\epsilon} \beta_0^{-1} . \quad (5.45)$$

The use of  $\beta_0$  as inverse mobility constant guarantees that the domain wall dynamics is independent of the width of the interface. Furthermore, the relation  $v_d = \beta_0^{-1} E_{\parallel}$  coincides with the domain wall velocity of a planar  $180^\circ$  domain wall that is treated as a singular surface and for which a linear kinetic law relating its normal velocity to the jump in the configurational stress tensor is postulated (cf. Sec. 4.1).

## 5.2 Numerical implementation

The initial boundary value problem consisting of Eqs. (3.133)–(3.135), (3.143) and (5.24)–(5.27) is solved within a 2d finite element scheme. Plane 4-noded elements with five degrees of freedom ( $u_i$ ,  $\varphi$ ,  $P_i$ ) per node and bilinear ansatz functions are used in the spatial discretization. Time integration is accomplished by using an implicit first order method. The following outline of the numerical procedure does not cover every detail required for a complete summary. Further background on standard finite element techniques can be acquired from e.g. ZIENKIEWICZ & TAYLOR (2000), HUGHES (2000), and WRIGGERS (2009).

The starting point of the finite element formulation is the weak form of the field equations (3.133), (3.135), and (5.24). After multiplication with the test functions  $\boldsymbol{\eta}_u$ ,  $\eta_\varphi$ ,  $\boldsymbol{\eta}_P$ , subsequent partial integration, and on use of the boundary conditions (3.143), (5.25), and (5.27), the weak forms read

$$\int_{\mathcal{B}} (-\boldsymbol{\sigma} \cdot \nabla \boldsymbol{\eta}_u + \mathbf{f} \cdot \boldsymbol{\eta}_u) dv + \int_{\partial \mathcal{B}_t} \mathbf{t}^* \cdot \boldsymbol{\eta}_u da = 0 , \quad (5.46)$$

$$\int_{\mathcal{B}} (-\mathbf{D} \cdot \nabla \eta_\varphi - \rho \eta_\varphi) dv - \int_{\partial \mathcal{B}_\omega} \omega^* \eta_\varphi da = 0 , \quad (5.47)$$

$$\int_{\mathcal{B}} \left\{ \left( \beta \dot{\mathbf{P}} + \frac{\partial \tilde{H}^{\text{ent}}}{\partial \mathbf{P}} + \kappa_s \frac{\gamma}{\epsilon} \frac{\partial \tilde{\psi}}{\partial \mathbf{P}} \right) \cdot \boldsymbol{\eta}_{\mathbf{P}} + \kappa_i \frac{\gamma \epsilon}{P_0^2} \nabla \mathbf{P} \cdot \nabla \boldsymbol{\eta}_{\mathbf{P}} \right\} dv = 0 . \quad (5.48)$$

The geometry, the independent variables and their test functions are approximated by the shape functions and the nodal quantities. Denoted by an underbar, the discretized quantities and equations are represented in matrix notation. For a finite element  $\mathcal{B}^e$  this gives

$$\begin{aligned} \underline{\mathbf{x}} &= \sum_I^{n_{\text{el}}} N_{\mathbf{x}}^I \underline{\mathbf{x}}^I, \quad \underline{\mathbf{u}} = \sum_I^{n_{\text{el}}} N_{\mathbf{u}}^I \underline{\mathbf{u}}^I, \quad \underline{\varphi} = \sum_I^{n_{\text{el}}} N_{\varphi}^I \underline{\varphi}^I, \quad \underline{\mathbf{P}} = \sum_I^{n_{\text{el}}} N_{\mathbf{P}}^I \underline{\mathbf{P}}^I, \\ \underline{\boldsymbol{\eta}}_{\mathbf{x}} &= \sum_I^{n_{\text{el}}} N_{\mathbf{x}}^I \underline{\boldsymbol{\eta}}_{\mathbf{x}}^I, \quad \underline{\boldsymbol{\eta}}_{\mathbf{u}} = \sum_I^{n_{\text{el}}} N_{\mathbf{u}}^I \underline{\boldsymbol{\eta}}_{\mathbf{u}}^I, \quad \underline{\boldsymbol{\eta}}_{\varphi} = \sum_I^{n_{\text{el}}} N_{\varphi}^I \underline{\boldsymbol{\eta}}_{\varphi}^I, \quad \underline{\boldsymbol{\eta}}_{\mathbf{P}} = \sum_I^{n_{\text{el}}} N_{\mathbf{P}}^I \underline{\boldsymbol{\eta}}_{\mathbf{P}}^I. \end{aligned} \quad (5.49)$$

The superscript  $I$  denotes the node number,  $n_{\text{el}}$  is the number of nodes per element, and  $N_{\mathbf{x}}^I$ ,  $N_{\mathbf{u}}^I$ ,  $N_{\varphi}^I$ , and  $N_{\mathbf{P}}^I$  are the shape functions for the element geometry, the displacements, the electric potential, and the spontaneous polarization, respectively. The respective nodal values are denoted by  $\underline{\mathbf{x}}^I$ ,  $\underline{\mathbf{u}}^I$ ,  $\underline{\varphi}^I$ , and  $\underline{\mathbf{P}}^I$ .

For the 2d case, the differential operator matrices  $\underline{\mathbf{B}}_{\mathbf{u}}$ ,  $\underline{\mathbf{B}}_{\varphi}$ , and  $\underline{\mathbf{B}}_{\mathbf{P}}$  are defined by the derivatives of the shape functions:

$$\underline{\mathbf{B}}_{\mathbf{u}}^I = \begin{bmatrix} N_{\mathbf{u},1}^I & 0 \\ 0 & N_{\mathbf{u},2}^I \\ N_{\mathbf{u},2}^I & N_{\mathbf{u},1}^I \end{bmatrix}, \quad \underline{\mathbf{B}}_{\varphi}^I = \begin{bmatrix} N_{\varphi,1}^I \\ N_{\varphi,2}^I \end{bmatrix}, \quad \underline{\mathbf{B}}_{\mathbf{P}}^I = \begin{bmatrix} N_{\mathbf{P},1}^I & 0 \\ 0 & N_{\mathbf{P},2}^I \\ N_{\mathbf{P},2}^I & 0 \\ 0 & N_{\mathbf{P},1}^I \end{bmatrix}, \quad (5.50)$$

where  $N_{\cdot,k}^I$  denotes the partial derivative of a shape function with respect to the coordinate  $x_k$ . The approximated gradient quantities read

$$\begin{aligned} \underline{\boldsymbol{\varepsilon}} &= \sum_I^{n_{\text{el}}} \underline{\mathbf{B}}_{\mathbf{u}}^I \underline{\mathbf{u}}^I, \quad \underline{\mathbf{E}} = - \sum_I^{n_{\text{el}}} \underline{\mathbf{B}}_{\varphi}^I \underline{\varphi}^I, \quad \nabla \underline{\mathbf{P}} = \sum_I^{n_{\text{el}}} \underline{\mathbf{B}}_{\mathbf{P}}^I \underline{\mathbf{P}}^I, \\ \nabla \underline{\boldsymbol{\eta}}_{\mathbf{u}} &= \sum_I^{n_{\text{el}}} \underline{\mathbf{B}}_{\mathbf{u}}^I \underline{\boldsymbol{\eta}}_{\mathbf{u}}^I, \quad \nabla \underline{\boldsymbol{\eta}}_{\varphi} = \sum_I^{n_{\text{el}}} \underline{\mathbf{B}}_{\varphi}^I \underline{\boldsymbol{\eta}}_{\varphi}^I, \quad \nabla \underline{\boldsymbol{\eta}}_{\mathbf{P}} = \sum_I^{n_{\text{el}}} \underline{\mathbf{B}}_{\mathbf{P}}^I \underline{\boldsymbol{\eta}}_{\mathbf{P}}^I, \end{aligned} \quad (5.51)$$

which implies the use of the Voigt notation

$$\underline{\boldsymbol{\varepsilon}} = \begin{bmatrix} \varepsilon_{11} & \varepsilon_{22} & 2\varepsilon_{12} \end{bmatrix}^T, \quad \nabla \underline{\mathbf{P}} = \begin{bmatrix} P_{1,1} & P_{2,2} & P_{1,2} & P_{2,1} \end{bmatrix}^T, \quad (5.52)$$

and  $\underline{\mathbf{E}} = [E_1 \ E_2]^T$ . Insertion of the discretized equations (5.49) and (5.51) into the weak forms (5.46)–(5.48) yields the approximations

$$\bigcup_{e=1}^{n_e} \sum_{I=1}^{n_{el}} (\underline{\eta}_{\mathbf{u}}^I)^T \left[ \int_{\mathcal{B}^e} \left( -(\underline{\mathbf{B}}_{\mathbf{u}}^I)^T \underline{\boldsymbol{\sigma}} + N_{\mathbf{u}}^I \underline{\mathbf{f}} \right) dv + \int_{\partial \mathcal{B}^e} N_{\mathbf{u}}^I \underline{\mathbf{t}}^* da \right] = 0 , \quad (5.53)$$

$$\bigcup_{e=1}^{n_e} \sum_{I=1}^{n_{el}} \underline{\eta}_{\varphi}^I \left[ \int_{\mathcal{B}^e} \left( -(\underline{\mathbf{B}}_{\varphi}^I)^T \underline{\mathbf{D}} - N_{\varphi}^I \underline{\rho} \right) dv - \int_{\partial \mathcal{B}^e} N_{\varphi}^I \underline{\omega}^* da \right] = 0 , \quad (5.54)$$

$$\begin{aligned} \bigcup_{e=1}^{n_e} \sum_{I=1}^{n_{el}} (\underline{\eta}_{\mathbf{P}}^I)^T \int_{\mathcal{B}^e} \left\{ N_{\mathbf{P}}^I \left( \underline{\beta} \dot{\underline{\mathbf{P}}} + \frac{\partial \tilde{H}^{\text{ent}}}{\partial \underline{\mathbf{P}}} + \kappa_s \frac{\gamma}{\epsilon} \frac{\partial \tilde{\psi}}{\partial \underline{\mathbf{P}}} \right) \right. \\ \left. + \kappa_i \frac{\gamma \epsilon}{P_0^2} (\underline{\mathbf{B}}_{\mathbf{P}}^I)^T \nabla \underline{\mathbf{P}} \right\} dv = 0 . \end{aligned} \quad (5.55)$$

The integration is performed for each finite element, and the operator  $\bigcup$  symbolizes the assembly of the equations over all elements. The integrals in the brackets are the element residuals for node  $I$ :

$$\underline{\mathbf{R}}_{\sigma}^I = \int_{\mathcal{B}^e} \left( -(\underline{\mathbf{B}}_{\mathbf{u}}^I)^T \underline{\boldsymbol{\sigma}} + N_{\mathbf{u}}^I \underline{\mathbf{f}} \right) dv + \int_{\partial \mathcal{B}^e} N_{\mathbf{u}}^I \underline{\mathbf{t}}^* da , \quad (5.56)$$

$$\underline{\mathbf{R}}_{\mathbf{D}}^I = \int_{\mathcal{B}^e} \left( -(\underline{\mathbf{B}}_{\varphi}^I)^T \underline{\mathbf{D}} - N_{\varphi}^I \underline{\rho} \right) dv - \int_{\partial \mathcal{B}^e} N_{\varphi}^I \underline{\omega}^* da , \quad (5.57)$$

$$\underline{\mathbf{R}}_{\mathbf{P}}^I = \int_{\mathcal{B}^e} \left\{ N_{\mathbf{P}}^I \left( \underline{\beta} \dot{\underline{\mathbf{P}}} + \frac{\partial \tilde{H}^{\text{ent}}}{\partial \underline{\mathbf{P}}} + \kappa_s \frac{\gamma}{\epsilon} \frac{\partial \tilde{\psi}}{\partial \underline{\mathbf{P}}} \right) + \kappa_i \frac{\gamma \epsilon}{P_0^2} (\underline{\mathbf{B}}_{\mathbf{P}}^I)^T \nabla \underline{\mathbf{P}} \right\} dv . \quad (5.58)$$

With the more compact notation

$$\underline{\mathbf{R}}^I = \left[ (\underline{\mathbf{R}}_{\sigma}^I)^T \ \underline{\mathbf{R}}_{\mathbf{D}}^I \ (\underline{\mathbf{R}}_{\mathbf{P}}^I)^T \right]^T , \quad (5.59)$$

the element residual for the four-noded element  $e$  is introduced as

$$\underline{\mathbf{R}}^e = \left[ (\underline{\mathbf{R}}^1)^T \ (\underline{\mathbf{R}}^2)^T \ (\underline{\mathbf{R}}^3)^T \ (\underline{\mathbf{R}}^4)^T \right]^T . \quad (5.60)$$

Then the assembled system of equations reads

$$\bigcup_{e=1}^{n_e} (\underline{\eta}^e)^T \underline{\mathbf{R}}^e = 0 . \quad (5.61)$$

The assembled residual must vanish for arbitrary test functions, i.e.

$$\underline{\mathbf{R}} = \bigcup_{e=1}^{n_e} \underline{\mathbf{R}}^e = \mathbf{0} . \quad (5.62)$$



The global residual vector  $\underline{\mathbf{R}}$  is a function of the nodal degrees of freedom. These are collected in the global vector of degrees of freedom  $\underline{\mathbf{d}}$  so that

$$\underline{\mathbf{R}} = \underline{\mathbf{R}}(\underline{\mathbf{d}}, \dot{\underline{\mathbf{d}}}) . \quad (5.63)$$

The velocities are approximated by means of the implicit Euler method:

$$\dot{\underline{\mathbf{d}}} \approx \frac{\underline{\mathbf{d}}_{n+1} - \underline{\mathbf{d}}_n}{\Delta t_n} \quad (5.64)$$

with the time increment  $\Delta t_n$ . With respect to the time discretization, the indices  $n$  and  $n + 1$  denote quantities at the current and next time step in the Newton iteration, respectively.<sup>11</sup> The residual is then a function of the time-discretized degrees of freedom:  $\underline{\mathbf{R}}_{n+1} = \hat{\underline{\mathbf{R}}}(\underline{\mathbf{d}}_{n+1})$ . Postulating that the residual vanishes at the next time step  $t_{n+1}$ , one obtains the non-linear system of equations

$$\underline{\mathbf{R}}_{n+1} = \hat{\underline{\mathbf{R}}}(\underline{\mathbf{d}}_{n+1}) = \underline{\mathbf{0}} . \quad (5.65)$$

The Newton-Raphson method is used to find approximate solutions  $\underline{\mathbf{d}}_{n+1}^{i+1}$ , where  $i$  is used as the index of the iteration procedure. This requires the computation of the system matrix

$$\underline{\mathbf{S}}(\underline{\mathbf{d}}_{n+1}^i) = \left. \frac{\partial \hat{\underline{\mathbf{R}}}}{\partial \underline{\mathbf{d}}_{n+1}} \right|_{\underline{\mathbf{d}}_{n+1}^i} \quad (5.66)$$

as well as the current residual  $\underline{\mathbf{R}}_{n+1}^i$ . The next iterative solution is then calculated with

$$\underline{\mathbf{d}}_{n+1}^{i+1} = \underline{\mathbf{d}}_{n+1}^i - [\underline{\mathbf{S}}(\underline{\mathbf{d}}_{n+1}^i)]^{-1} \underline{\mathbf{R}}_{n+1}^i . \quad (5.67)$$

The system matrix  $\underline{\mathbf{S}}$  is to be constructed from the stiffness and damping matrix of the residual in Eq. (5.63). On the element level, the stiffness and damping matrix contributions are obtained by derivation with respect to  $\underline{\mathbf{u}}^J, \underline{\varphi}^J, \underline{\mathbf{P}}^J$  and  $\dot{\underline{\mathbf{u}}}^J, \dot{\underline{\varphi}}^J, \dot{\underline{\mathbf{P}}}^J$ , respectively:

$$\underline{\mathbf{K}}^{IJ} = \begin{bmatrix} \underline{\mathbf{R}}_{\underline{\mathbf{u}}^J}^I & \underline{\mathbf{R}}_{\underline{\varphi}^J}^I & \underline{\mathbf{R}}_{\underline{\mathbf{P}}^J}^I \end{bmatrix} = \begin{bmatrix} \underline{\mathbf{K}}_{\sigma\sigma}^{IJ} & \underline{\mathbf{K}}_{\sigma\text{D}}^{IJ} & \underline{\mathbf{K}}_{\sigma\text{P}}^{IJ} \\ \underline{\mathbf{K}}_{\text{D}\sigma}^{IJ} & \underline{\mathbf{K}}_{\text{DD}}^{IJ} & \underline{\mathbf{K}}_{\text{DP}}^{IJ} \\ \underline{\mathbf{K}}_{\text{P}\sigma}^{IJ} & \underline{\mathbf{K}}_{\text{PD}}^{IJ} & \underline{\mathbf{K}}_{\text{PP}}^{IJ} \end{bmatrix} \quad (5.68)$$

---

<sup>11</sup>Note that time discretization is only needed for the residual (5.58), the other two residuals are independent of  $\underline{\dot{\mathbf{P}}}$ .

and

$$\underline{\mathbf{D}}^{IJ} = \begin{bmatrix} \underline{\mathbf{R}}_{\underline{\mathbf{u}}^J}^I & \underline{\mathbf{R}}_{\dot{\varphi}^J}^I & \underline{\mathbf{R}}_{\dot{\mathbf{P}}^J}^I \end{bmatrix} = \begin{bmatrix} \mathbf{0} & \mathbf{0} & \mathbf{0} \\ \mathbf{0} & \mathbf{0} & \mathbf{0} \\ \mathbf{0} & \mathbf{0} & \underline{\mathbf{D}}_{\text{PP}}^{IJ} \end{bmatrix}. \quad (5.69)$$

The computation of the tangent matrix contributions is a straightforward, however lengthy calculation. Further details on the procedure can be found in App. A.5. In light of the time discretization in Eq. (5.64), the contributions to the system matrix read

$$\underline{\mathbf{S}}^{IJ} = \begin{bmatrix} \underline{\mathbf{K}}_{\sigma\sigma}^{IJ} & \underline{\mathbf{K}}_{\sigma\text{D}}^{IJ} & \underline{\mathbf{K}}_{\sigma\text{P}}^{IJ} \\ \underline{\mathbf{K}}_{\text{D}\sigma}^{IJ} & \underline{\mathbf{K}}_{\text{IJ}}^{\text{DD}} & \underline{\mathbf{K}}_{\text{DP}}^{IJ} \\ \underline{\mathbf{K}}_{\text{P}\sigma}^{IJ} & \underline{\mathbf{K}}_{\text{PD}}^{IJ} & \underline{\mathbf{K}}_{\text{PP}}^{IJ} + \frac{1}{\Delta t_n} \underline{\mathbf{D}}_{\text{PP}}^{IJ} \end{bmatrix}. \quad (5.70)$$

The element system matrix  $\underline{\mathbf{S}}^e$  is a  $20 \times 20$  matrix constructed by

$$\underline{\mathbf{S}}^e = \begin{bmatrix} \underline{\mathbf{S}}^{11} & \underline{\mathbf{S}}^{12} & \underline{\mathbf{S}}^{13} & \underline{\mathbf{S}}^{14} \\ \underline{\mathbf{S}}^{21} & \underline{\mathbf{S}}^{22} & \underline{\mathbf{S}}^{23} & \underline{\mathbf{S}}^{24} \\ \underline{\mathbf{S}}^{31} & \underline{\mathbf{S}}^{32} & \underline{\mathbf{S}}^{33} & \underline{\mathbf{S}}^{34} \\ \underline{\mathbf{S}}^{41} & \underline{\mathbf{S}}^{42} & \underline{\mathbf{S}}^{43} & \underline{\mathbf{S}}^{44} \end{bmatrix}. \quad (5.71)$$

The global system matrix in (5.66) is obtained by assembling the element matrices, i.e.

$$\underline{\mathbf{S}} = \bigcup_{e=1}^{n_e} \underline{\mathbf{S}}^e. \quad (5.72)$$

Due to the postulated existence of the thermodynamic potential  $\tilde{H}$ , the assembled system matrix  $\underline{\mathbf{S}}$  is symmetric; this can also be seen from the contributions to the element stiffness matrix, cf. App. A.5.

The integrals in Eqs. (5.56)–(5.58) are integrated by using standard four-point Gauss integration.

## 5.3 Examples

### 5.3.1 Introduction

The following numerical simulations are based on material data characterizing PZT-5H, for which a set of constants for transversely isotropic material behavior can be

found in DING & CHEN (2001, p. 12). These constants are slightly adapted to meet the symmetry prerequisites imposed by Eqs. (5.17) and (5.18):

$$\begin{aligned}\underline{\mathfrak{C}} &= \begin{bmatrix} 13 & 5.0 & 0 \\ 5.0 & 13 & 0 \\ 0 & 0 & 4.0 \end{bmatrix} \cdot 10^{10} \frac{\text{N}}{\text{m}^2} , \\ \underline{\mathfrak{e}} &= \begin{bmatrix} 0 & 0 & 17.0 \\ -6.5 & 23.3 & 0 \end{bmatrix} \frac{\text{C}}{\text{m}^2} , \\ \underline{\epsilon} &= \begin{bmatrix} 1.3 & 0 \\ 0 & 1.3 \end{bmatrix} \cdot 10^{-8} \frac{\text{C}}{\text{Vm}} .\end{aligned}\tag{5.73}$$

The value of the spontaneous polarization for PZT-5H is given in CHONG ET AL. (2008) by the estimate

$$P_0 = \frac{1}{0.83} P_{\text{sat}} \approx 0.32 \text{ C/m}^2 .\tag{5.74}$$

The geometric factor  $1/0.83$  accounts for the polycrystalline structure of the material due to which  $P_0$  is greater than  $P_{\text{sat}}$ .

The aforementioned publication also provides the lattice constants  $a$  and  $c$  of the tetragonal unit cell. In view of the definition of the spontaneous strain in Eq. (5.19), one obtains

$$\varepsilon^0 = 2 \frac{c - a}{c + 2a} \approx 0.0057\tag{5.75}$$

with  $a = 0.4051 \text{ nm}$  and  $c = 0.4086 \text{ nm}$ .

Ferroelectric domain walls are typically the width of a few unit cells.<sup>12</sup> With reference to MEYER & VANDERBILT (2002), the following values are used for the specific interface energy and width:

$$\gamma = 0.13 \frac{\text{J}}{\text{m}^2} , \quad \epsilon = 2 \cdot 10^{-9} \text{ m} .\tag{5.76}$$

The velocity of ferroelectric domain walls is dependent on the applied electric field (cf. Sec. 4.1). For electric fields near the coercive field  $E_c$ , domain wall

---

<sup>12</sup>See e.g. MERZ (1954), STEMMER ET AL. (1995), FOETH ET AL. (1999).

velocities are roughly of the order of 1 m/s. Since the literature seems to be unable to provide any precise data, the inverse mobility  $\beta = \beta \mathbf{1}$  is chosen by

$$\beta^{-1} = \frac{2P_0}{\epsilon} \frac{v_0}{E_c} = 0.32 \cdot 10^3 \frac{\text{A}}{\text{Vm}} , \quad (5.77)$$

where  $E_c = 1 \text{ MV/m}^{13}$  and  $v_0 = 1 \text{ m/s}$ . The parameters of  $\tilde{\psi}$  are chosen as

$$\begin{aligned} a_1 &= -1.125 , & a_2 &= -0.75 , & a_3 &= 3.3 , & a_4 &= 0.875 , \\ a_5 &= 0 , & a_6 &= 0 , & a_7 &= 0 , & a_8 &= 0 . \end{aligned} \quad (5.78)$$

For a detailed account on the calculation of these parameters, the reader is referred to App. A.4.

### 5.3.2 Parameter verification

#### Linear response

The choice of the electric enthalpy in Eq. (5.14) implies the structure of the constitutive equations (5.21)–(5.22). If the order parameter  $\mathbf{P}$  is fixed, i.e.  $\dot{\mathbf{P}} \equiv \mathbf{0}$ , then these equations reflect a linear piezoelectric constitutive law with respect to the current, fixed poling state. Within uniformly poled regions in which  $\mathbf{P}$  is equal to or near the minimizers of the phase separation potential, i.e. near the variants of the spontaneous states, the material tensors  $\mathbb{C}$ ,  $\epsilon$ , and  $\mathfrak{e}$  are the “classic” piezoelectric parameters.

However, since the order parameter is allowed to change, there will be an extra contribution to the electric displacement due to the change in  $\mathbf{P}$  when an electric field is applied. This extra polarization, induced by the external field, should be accounted for in the choice of  $\epsilon$  if necessary. A simple estimate of this extra polarization shows that this effect can be neglected for the chosen material parameters. For that purpose, a homogeneously poled region with  $\mathbf{P} = [0 \ P_0]^T$  is subjected to an electric field  $E_2$  in the  $x_2$ -direction; quasi-static conditions and stress-free support are assumed. As a consequence, Eq. (5.21) reduces to  $\mathbb{C}(\epsilon - \epsilon^0) = \mathfrak{e}^T \mathbf{E}$ , and thereby, with (5.14), the evolution equation (5.24) becomes

$$-\kappa_s \frac{\gamma}{\epsilon} \frac{\partial \tilde{\psi}}{\partial P_m} - (\epsilon_{ij} - \epsilon_{ij}^0) \frac{\partial \mathfrak{e}_{kij}}{\partial P_m} E_k - E_m = 0 . \quad (5.79)$$

By the assumption that  $\partial_{P_m} \mathfrak{e}_{kij} \ll 1$  (which is the case, see below), the middle summand in that equation can be neglected, so that for  $m = 2$  the previous equation

---

<sup>13</sup>Cf. CHONG ET AL. (2008).

reads

$$-\kappa_s \frac{\gamma}{\epsilon} \frac{\partial \tilde{\psi}}{\partial P_2} + E_2 = 0 . \quad (5.80)$$

The change in  $P_2$  due to the field  $E_2$  can be approximated by a Taylor expansion of  $\partial_{P_2} \tilde{\psi}$  around the spontaneous state  $(0, P_0)$ . Since, by definition,  $\partial_{P_2} \tilde{\psi}(0, P_0) = 0$ , this gives

$$\kappa_s \frac{\gamma}{\epsilon} \frac{\partial^2 \tilde{\psi}(0, P_0)}{\partial P_2^2} (P_2 - P_0) = E_2 . \quad (5.81)$$

Evaluating the second partial derivative gives the value  $15/P_0^2$ , and with the abbreviation

$$\kappa_P := \frac{\epsilon P_0^2}{15 \kappa_s \gamma} , \quad (5.82)$$

the resulting linear relation for  $P_2$  then reads

$$P_2 - P_0 = \kappa_P E_2 . \quad (5.83)$$

The parameter  $\kappa_P$  is the dielectric constant associated with the electric displacement due to a change in  $P_2$ . If, for a different set of material parameters,  $\kappa_P$  should reach the value of the material parameter  $\epsilon_{11}$ , the former can be reduced by changing the shape of the separation potential and thereby altering the value of  $\kappa_s$ . For the chosen material parameters,  $\kappa_P = 1.5 \cdot 10^{-10} \text{ C}/(\text{Vm})$ . This value would have to be subtracted from the value of  $\epsilon_{11} = 1.3 \cdot 10^{-8} \text{ C}/(\text{Vm})$ . In view of the assumption of an isotropic dielectric tensor and the difference of roughly 1% in the two values, the influence of  $\kappa_P$  can be neglected.

The piezoelectric response will also depend on the change of  $\boldsymbol{\varepsilon}^0$  and  $\mathbf{e}$  as both depend on  $\mathbf{P}$ . By assuming quasi-static and stress-free conditions once more, a simulation shows that the components  $\varepsilon_{ij}^0$  are linear in the applied electric field. This can be seen in Fig. 5.4 a), where the differences between  $\varepsilon_{ij}^0$  and their initial values are plotted. The deviation from the latter is well below 3%, revealing the small influence of the change in  $\mathbf{P}$ .

Under stress-free conditions, the piezoelectric law reduces to

$$\boldsymbol{\varepsilon} - \boldsymbol{\varepsilon}^0 = \mathbf{e} \mathbf{C}^{-\text{T}} \mathbf{E} = \mathbf{d}^{\text{T}} \mathbf{E} . \quad (5.84)$$

Figure 5.4 b) shows the strain response for the prescribed electric field. The linear relationship is in excellent quantitative agreement with Eq. (5.84), which implies that  $\mathbf{e}$  does not change significantly under the electric loading.

The results of these preceding calculations permit the interpretation of  $\mathbf{C}$ ,  $\mathbf{e}$ , and  $\boldsymbol{\varepsilon}$  as the linear piezoelectric material constants. The extra electric displacement contributed by changes in  $\mathbf{P}$  due to a small-signal electric field is negligible with respect to the dielectric polarization.

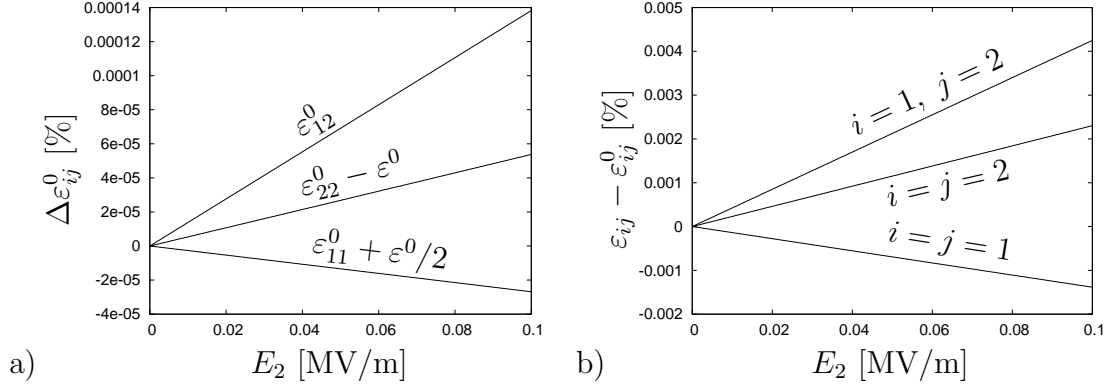


Figure 5.4: a) The change in the spontaneous strain components under electrical loading is very small compared to  $\epsilon^0 = 0.57\%$ , which is used in the simulations; this effect can therefore be ignored in the following. b) Linear piezoelectric response to electrical loading of the poled s phase. The influence of the electric field on the order parameter-dependent material constants  $\epsilon^0(\mathbf{P})$  and  $\mathfrak{e}(\mathbf{P})$  is negligible.

### 180° domain wall

A planar 180° domain wall is modeled with a rectangular region of  $20 \text{ nm} \times 40 \text{ nm}$  under stress-free support and vanishing electric potential on the boundary. The initial conditions for  $\mathbf{P}$  are chosen to define a vertical sharp 180° interface in the center of the region. During the simulation, the interface becomes diffuse and quickly reaches a state of equilibrium. This is illustrated in Fig. 5.5 where  $P_2$  and  $D_2$  are plotted. The geometry of the phase transition leads to a tensile stress  $\sigma_{22}$  in the interface, see Fig. 5.6. The three parts of the phase field potential,  $\tilde{H}^{\text{ent}}$ ,  $\tilde{H}^{\text{sep}}$  and  $\tilde{H}^{\text{int}}$ , are plotted in Figs. 5.6 and 5.7. The difference in the order of magnitude

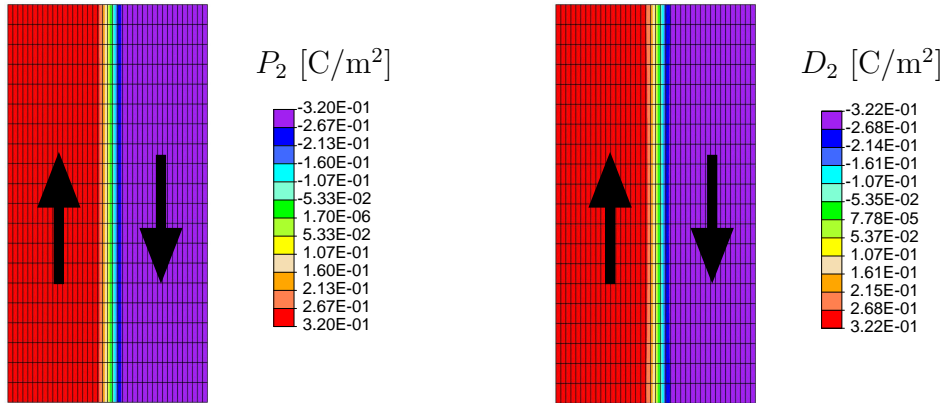


Figure 5.5: Distribution of  $P_2$  and  $D_2$ , 180° domain wall.

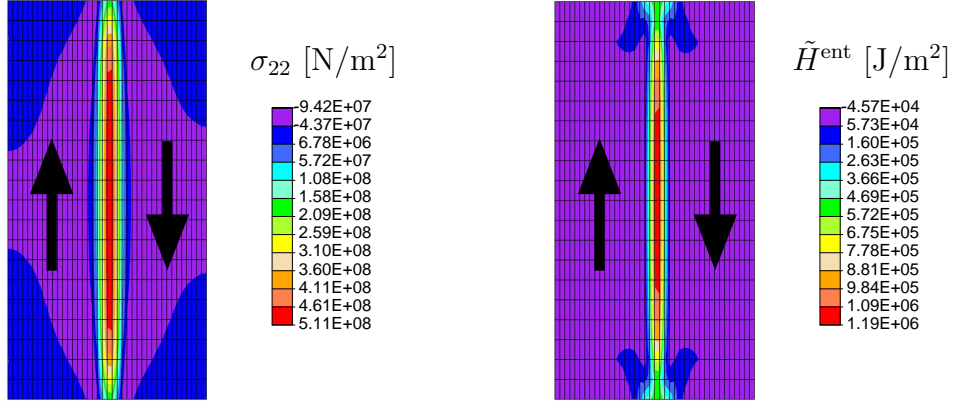


Figure 5.6: Distribution of  $\sigma_{22}$  and  $\tilde{H}^{\text{ent}}$ ,  $180^\circ$  domain wall. The stress  $\sigma_{22}$  in and around the interfacial region is due to the transition of  $\epsilon^0$  from a tetragonal to a cubic and back to a tetragonal state across the interface.

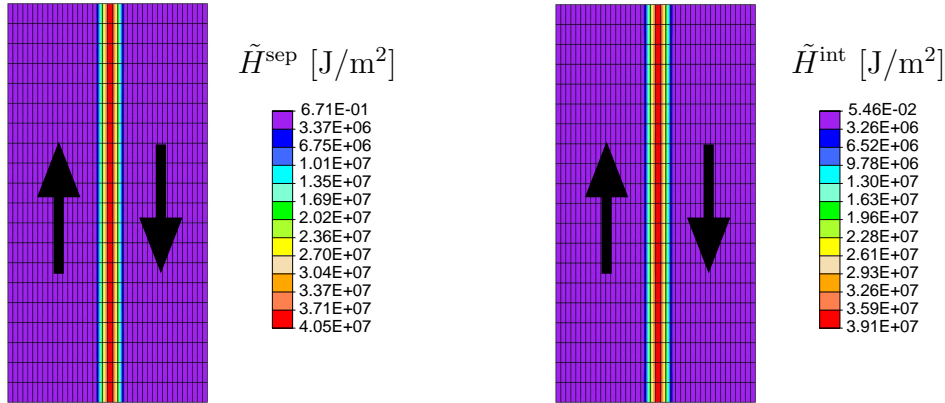


Figure 5.7: The phase separation and gradient energy densities are considerably larger than  $\tilde{H}^{\text{ent}}$  plotted in Fig. 5.6.

between  $\tilde{H}^{\text{sep}} + \tilde{H}^{\text{int}}$  and  $\tilde{H}^{\text{ent}}$  justifies the basic working assumption of Sec. 5.1.3, namely that the former outweighs the latter.

The intrinsic length scale  $\epsilon$  requires a mesh resolution which is able to resolve the interfaces. In order to find a reasonable spatial discretization, the previous simulation is repeated for different element edge lengths in the  $x_1$ -direction, i.e. in the direction perpendicular to the domain wall. Figure 5.8 a) contains a plot of the element edge length vs. the interface width  $d$  by means of Eq. (5.35). For edge lengths smaller than  $\epsilon/4$ , the numerically obtained interface width differs from the value of  $\epsilon$  by less than 5%. If the edge length is near  $\epsilon$ , then  $d$  depends strongly on the position of the middle of the interface within the element. In view of these

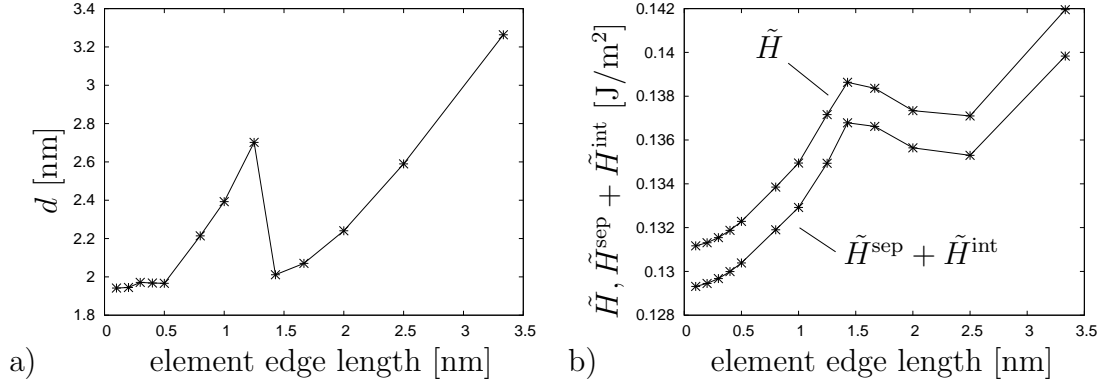


Figure 5.8: a) The numerically calculated 180° interface width is influenced by the element edge length used in the simulation. Given  $\epsilon = 2$  nm, the element edge length should be chosen as  $\epsilon/4$ . b) The numerically obtained specific 180° domain wall energy varies with the element edge length used in the simulations. The deviations amount up to 10% with respect to  $\gamma = 0.13$  J/m².

results, a maximum element edge length of  $\epsilon/4$  is indicated.

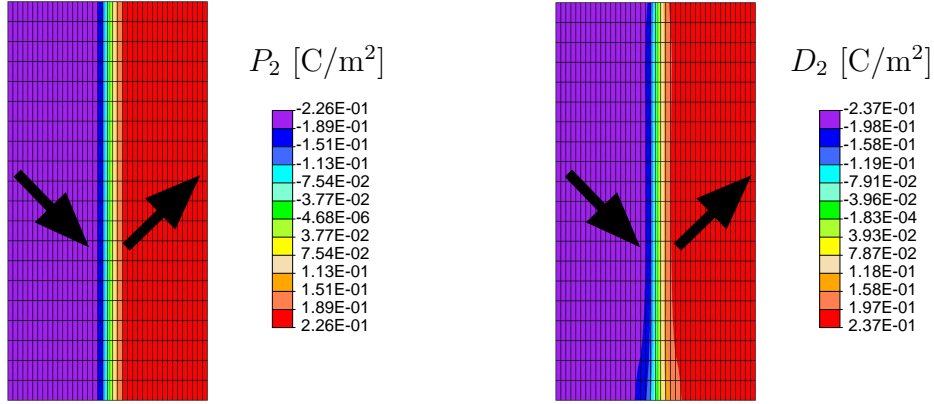
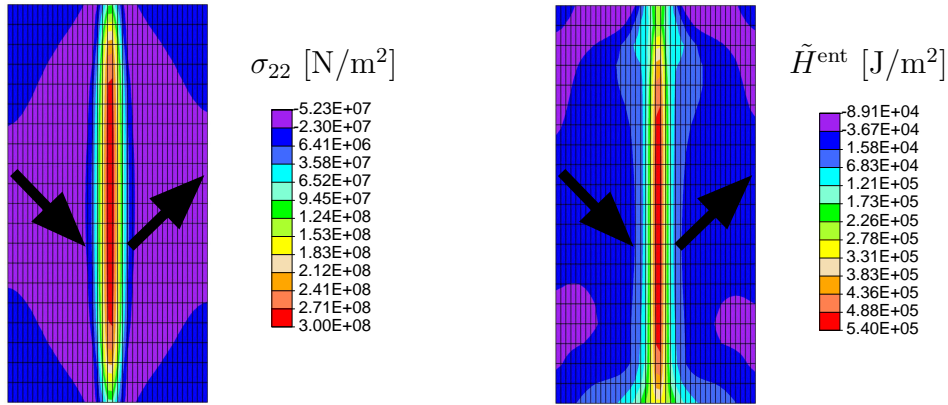
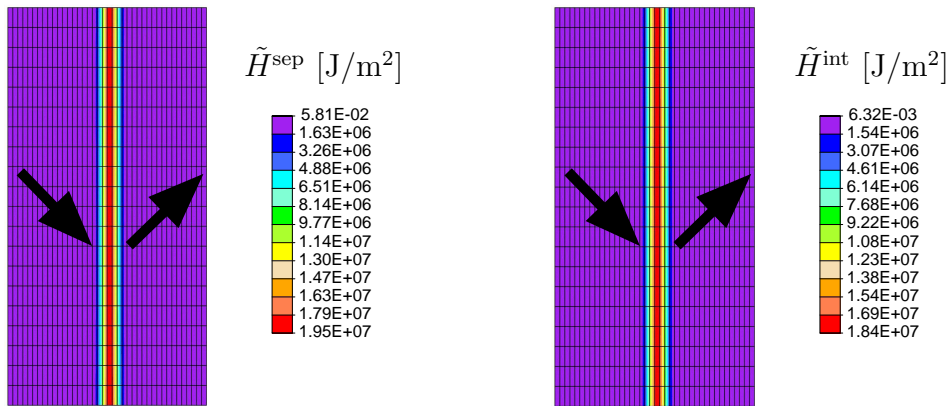
The contributions to the specific energy of an interface are obtained by integrating the fields  $\tilde{H}^{\text{ent}}$ ,  $\tilde{H}^{\text{sep}}$ , and  $\tilde{H}^{\text{int}}$  along the horizontal path in the center of the discretized region. This procedure circumvents the boundary effects visible in Fig. 5.6 by assuming that these fields are homogeneous in the vertical direction. The numerically obtained values are shown in Fig. 5.8 b). For element edge lengths less than  $\epsilon/4$ , the calculated specific energies deviate less than 2% from the value of  $\gamma$ . Even for large edge lengths, the difference is below 10%.

### 90° domain wall

The simulations performed for the 180° interface are repeated for a 90° domain wall. Figure 5.9 shows contour plots of  $P_2$  and  $D_2$ ; the orientation of the crystal axes is rotated 45° with respect to the  $x_1$ - $x_2$  coordinate system used in the preceding simulations. The tensile stress  $\sigma_{22}$  and the distribution of  $\tilde{H}^{\text{ent}}$ ,  $\tilde{H}^{\text{sep}}$ , and  $\tilde{H}^{\text{int}}$  are plotted in Figs. 5.10 and 5.11. As for the 180° interface, the stress  $\sigma_{22}$  originates from the varying  $\epsilon^0(\mathbf{P})$  across the interfacial region; the energy contribution from  $\tilde{H}^{\text{ent}}$  is also small compared to  $\tilde{H}^{\text{sep}}$  and  $\tilde{H}^{\text{int}}$ .

Analogously to the 180° case, the interface width and the specific energy are computed for a 90° domain wall. Figure 5.12 a) shows that the calculated interface widths increase with coarsening mesh resolution. The values for the 180° domain wall show that the two interfaces are of comparable width. This is supported



Figure 5.9: Distribution of  $P_2$  and  $D_2$ ,  $90^\circ$  domain wall.Figure 5.10: Distribution of  $\sigma_{22}$  and  $\tilde{H}^{\text{ent}}$ ,  $90^\circ$  domain wall.Figure 5.11: Phase separation and gradient energy densities,  $90^\circ$  domain wall. The contributions from  $\tilde{H}^{\text{sep}}$  and  $\tilde{H}^{\text{int}}$  to the interface energy outweigh the contribution from  $\tilde{H}^{\text{ent}}$ , cf. Fig. 5.10.

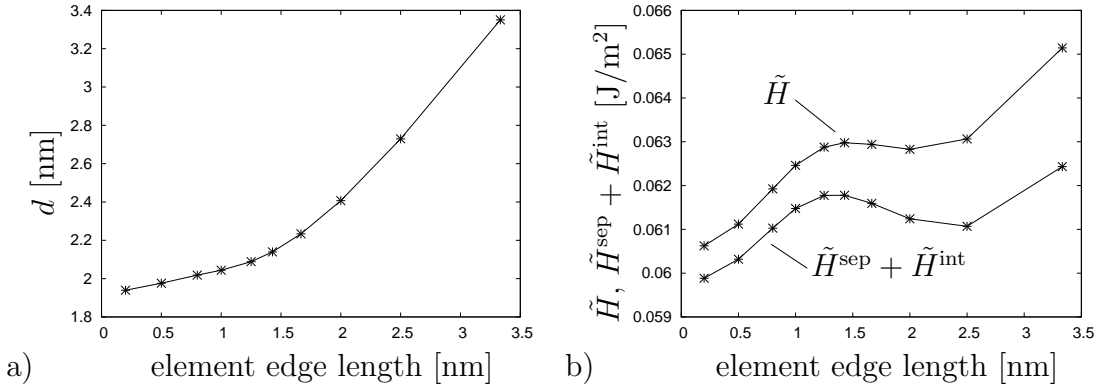


Figure 5.12: a) With increasing element edge length, the calculated 90° interface widths deviate strongly from the given material parameter  $\epsilon = 2$  nm. b) The calculated 90° interface energy densities vary with the element edge length to an extent comparable to the 180° case, cf. Fig. 5.8 b).

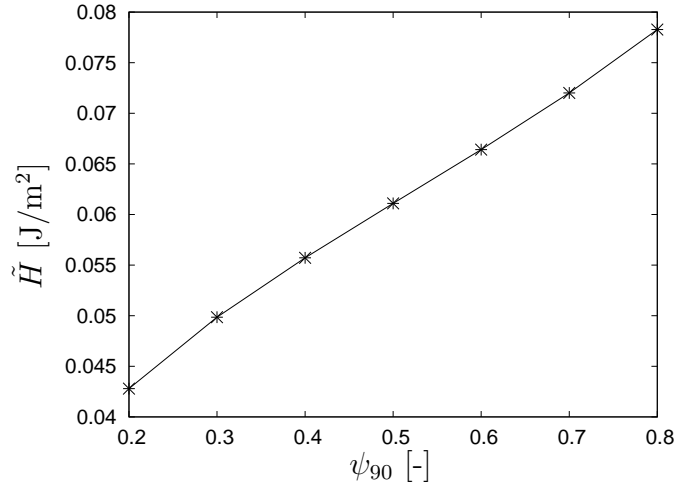


Figure 5.13: Influence of the auxiliary parameter  $\psi_{90}$  introduced in App. A.4 on  $\tilde{H}$ . Due to the nearly linear relationship, the parameter  $\psi_{90}$  can be used to adjust the 90° domain wall energy.

by recent results in the literature (cf. MEYER & VANDERBILT 2002, STEMMER ET AL. 1995).

The contributions to the numerically obtained specific interface energy are plotted in Figs. 5.12 b) and 5.13. The set of  $a_i$  defined in (5.78) yields a 90° interfacial energy which amounts to about one half of the 180° domain wall energy. This is also in good agreement with experimental data and atomistic simulations, see MEYER & VANDERBILT (2002), STEMMER ET AL. (1995) and the references cited therein. The 90° interface energy can further be adjusted by changing the

parameter  $\psi_{90}$  (see App. A.4) which is used in the calculation of the non-zero coefficients  $a_i$  in Eq. (5.78). The graph in Fig. 5.13 shows that there is a linear relation between  $\psi_{90}$  and the specific  $90^\circ$  interface energy, which lies approximately between  $0.35\gamma$  and  $0.6\gamma$ .

### Domain wall dynamics

The dynamics of  $180^\circ$  and  $90^\circ$  interfaces is studied on the basis of the previous simulations. The discretized region is now  $40 \text{ nm} \times 40 \text{ nm}$ , and the applied voltage difference of  $4 \cdot 10^{-2} \text{ V}$  induces an electric field of  $1 \text{ MV/m}$ . Since the domain wall remains planar during its movement, it is reasonable to define the interface position with  $P_2(x_1, x_2^c) = 0$ , where  $x_2^c$  lies in the center of the mesh in the vertical direction.

At the beginning of the simulation, the electric field is activated for the time interval  $\Delta t$ . During this time, the interface moves by the distance  $\Delta x$ ; the average domain wall velocity is then given by  $v_d = \Delta x / \Delta t$ . With the estimate in Eq. (5.44) and the value of  $\beta^{-1}$  given in Eq. (5.77), a  $180^\circ$  interface velocity of  $v_d = 1 \text{ m/s}$  is to be expected.

Figures 5.14a) and b) show the resulting domain wall velocities for varying element edge lengths in the  $x_1$ -direction and for different values for  $\epsilon$ , respectively. In view of Eq. (5.44) and the chosen value of  $\beta^{-1}$ , the calculated values for  $v_d$  are considerably higher than the expected value of  $v_d = 1 \text{ m/s}$ . Since the center of the interface need not lie on an element edge, the values of  $\dot{\mathbf{P}}$  are not evaluated exactly at  $\mathbf{P} = \mathbf{0}$ . This leads to a higher absolute value of  $\dot{P}_2$  to which this

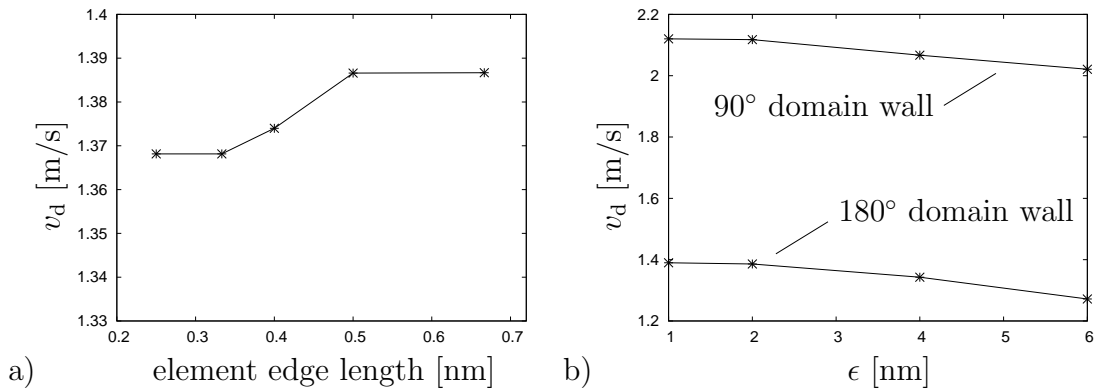


Figure 5.14: a) The  $180^\circ$  domain wall velocity is nearly independent of the element edge length but, for numerical reasons, higher than the expected value of  $1 \text{ m/s}$ . b) Both the  $180^\circ$  and  $90^\circ$  domain wall velocity show only a weak dependence on the interface width.

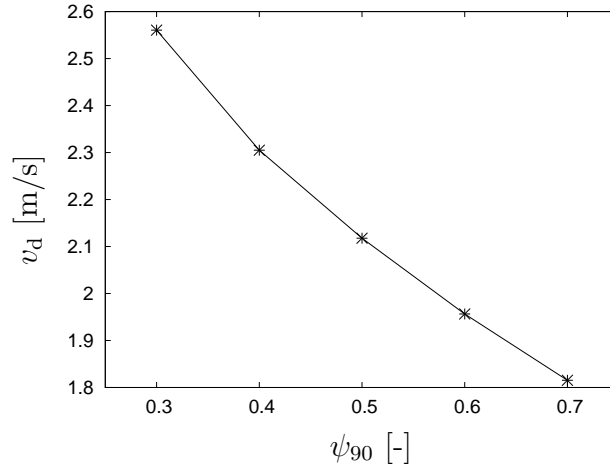


Figure 5.15: The velocity of the 90° domain wall is almost linear in the auxiliary parameter  $\psi_{90}$  used in App. A.4.

deviation in  $v_d$  is to be attributed. The figures also show that  $v_d$  varies only slightly with a change in the mesh discretization normal to the interface. Due to the rescaling of  $\beta^{-1}$  in (5.45),  $v_d$  depends only mildly on the interface width. It is noted that  $\beta^{-1}$  represents the inner time scale of the model; thus the interface velocity is proportional to  $\beta^{-1}$ .

The results for the 90° domain wall are shown in Figs. 5.14 b) and 5.15. The interface velocities are approximately 50% higher as compared to the 180° case. The dependency of  $v_d$  on  $\epsilon$  is also comparably low. The interface velocity is however strongly influenced by the parameter  $\psi_{90}$ , see Fig. 5.15 besides App. A.4.

### 5.3.3 Domain wall pinning

Domain wall mobility and motion are affected by different kinds of defects which can be a cause for the slowing or pinning of domain walls.<sup>14</sup> The following simulations are concerned with a defected electrode and two kinds of “frozen polarization” defects.

#### Electrode defect

As in Sec. 4.3.1, an electrode defect is modeled by imposing the boundary condition  $\mathbf{D} \cdot \mathbf{n} = 0$  or  $\varphi^* = 0$  over the length of the defect width. Figure 5.16 shows the

<sup>14</sup>Cf. BRENNAN (1993), YANG ET AL. (1999), SCOTT & DAWBER (2000), KONTOS & LANDIS (2009), BHATTACHARYA & HIGGINS (2009).

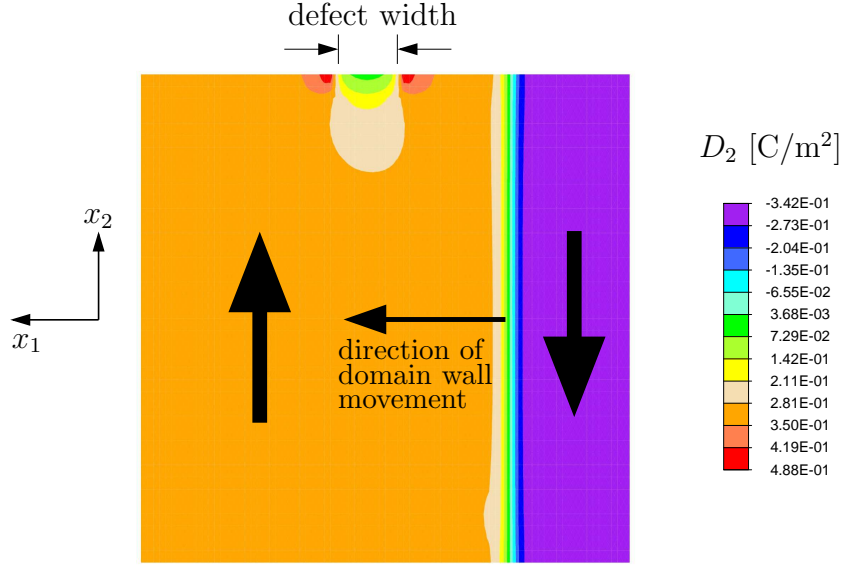


Figure 5.16: Initial configuration for a  $180^\circ$  domain wall driven toward the electrode defect by an applied electric field activated for a fixed time interval.

initial configuration in which a  $180^\circ$  domain wall is located to the right of a defect. An external electric field is applied for a fixed time interval, driving the domain wall toward the defect. The influence of the defect on the domain wall mobility is studied by calculating the average domain wall velocity for that time interval. This requires the determination of the interface position, which depends on the vertical direction due to the bending of the interface near the defect. As a working assumption, the interface positions are determined from  $P_2(x_1, x_2^c) = 0$  where  $x_2^c$  stands for the center of the mesh in the vertical direction, i.e.  $x_2^c = 0$  in Fig. 5.16.

For the defect condition  $\varphi^* = 0$ , the obtained average velocities are plotted versus the driving field in Fig. 5.17; the linear relation of the defect-free case is shown for comparison. The smaller defect has no pinning effect on the domain wall, but its mobility is severely decreased. The other defect is wide enough to lead to domain wall pinning for all applied driving fields. For the strongest field, pinning takes place within the fixed time interval; for the weaker fields, the (slower) domain walls are pinned only if the time interval of the activated driving field is extended such that a stationary state is reached. The pinning effect can be explained by a strong positive electric field  $E_2$  around the defect which prevents switching in that area. Since this disturbance is only local, switching continues in lower parts of the interface, which leads to domain wall bending.

The defect condition  $\mathbf{D} \cdot \mathbf{n} = 0$  has a considerably weaker effect on the interface mobility. This can be seen in Fig. 5.18, where average interface velocities are

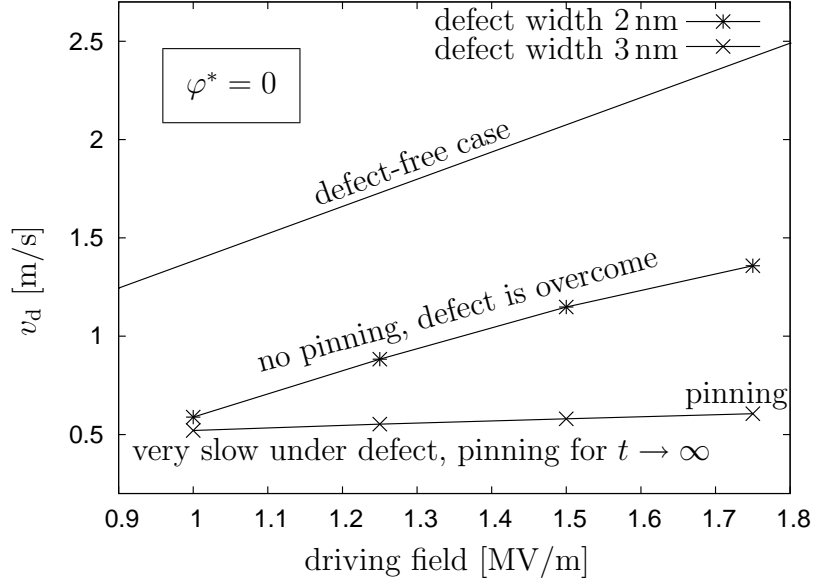


Figure 5.17: Both of the two defects modeled with  $\varphi^* = 0$  have an impeding effect on the defect mobility as reflected by the average domain wall velocity  $v_d$ . While the smaller defect has no pinning effect and can be overcome by the domain wall, the wider defect ultimately leads to pinning.

plotted against the driving field for three different interface widths (which are wider compared to the previous simulations).

Again, the linear velocity for the defect-free case is plotted for comparison. The smallest defect has only little influence on the interface mobility; it is overcome for all driving fields except for the lowest, where the final interface position (after application of the driving field for the fixed time interval) is located at the end of the defect. For this defect, pinning takes place for driving fields below approximately 0.4 MV/m. For the 10 nm defect, pinning takes place at a higher driving field compared to the smaller defect, and the domain wall does not even reach the end of the defect for the lowest driving field. The situation is similar for the widest defect where the domain wall is pinned for an even higher driving field. Note that the graphs for 10 nm and 15 nm intersect the other two graphs, which indicates an increased domain wall mobility for low driving fields despite the fact that the former graphs belong to the wider, i.e. stronger, defects. This behavior is due to the strong negative electric field  $E_2$  around the defect needed to compensate for the electric displacement from the spontaneous polarization. The same result was obtained in Sec. 4.3.1 in the context of the sharp interface approach. As can be seen in Fig. 4.11, the average driving force has a very high absolute value and

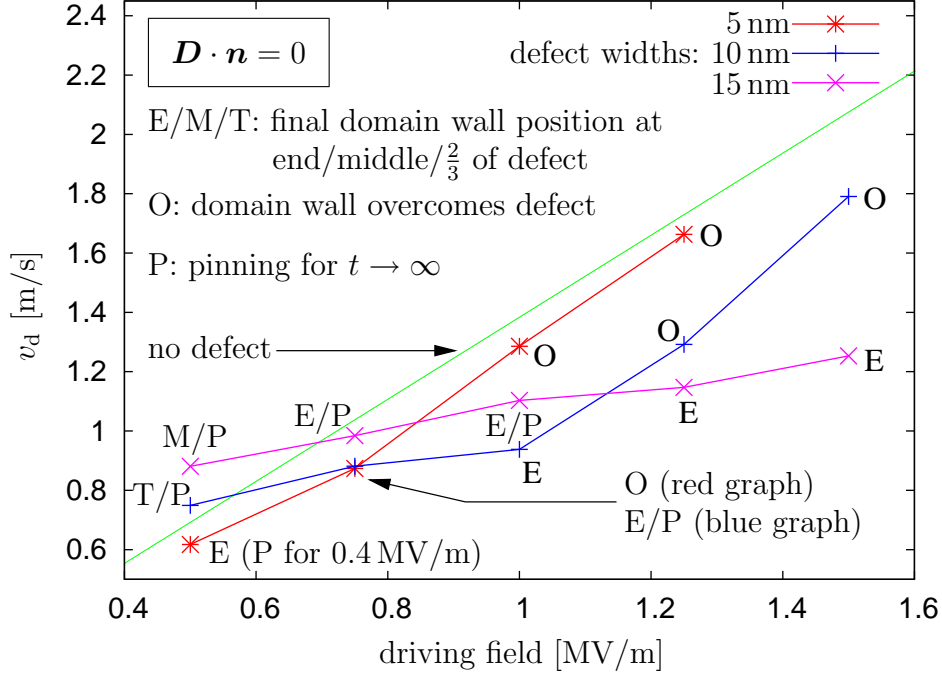


Figure 5.18: The defects modeled with  $\mathbf{D} \cdot \mathbf{n} = 0$  also have an impeding effect on the domain wall mobility. The smaller defects can be overcome at lower driving fields, and the critical pinning fields increase with defect width. The increased mobilities for low driving fields compared to the defect-free case are due to the strong electric field in the defect area which lead to accelerated poling.

drives the domain wall through the defect area at an increased velocity compared to the defect free-case for which  $T_n = -2 \text{ kJ/m}^3$ .

### Polarization defect

A polarization defect is regarded as a microscopic area in which the spontaneous polarization is frozen in the sense that switching is impossible in that area. As noted in Sec. 4.3.3, this phenomenon has been observed in PZT thin films in the context of electrical fatigue (cf. GRUVERMAN ET AL. 1996, COLLA ET AL. 1998).

In the following, the influence of polarization defects on the mobility of  $180^\circ$  and  $90^\circ$  domain walls is studied. The defect under consideration is a quadratic region of  $2 \text{ nm} \times 2 \text{ nm}$ , which is of the same length scale as the interface width. In that region the spontaneous polarization is assigned the fixed value  $\mathbf{P}^{\text{def}}$ . Except for the evolution equation, all field equations apply for the defect just as well as for the surrounding material.



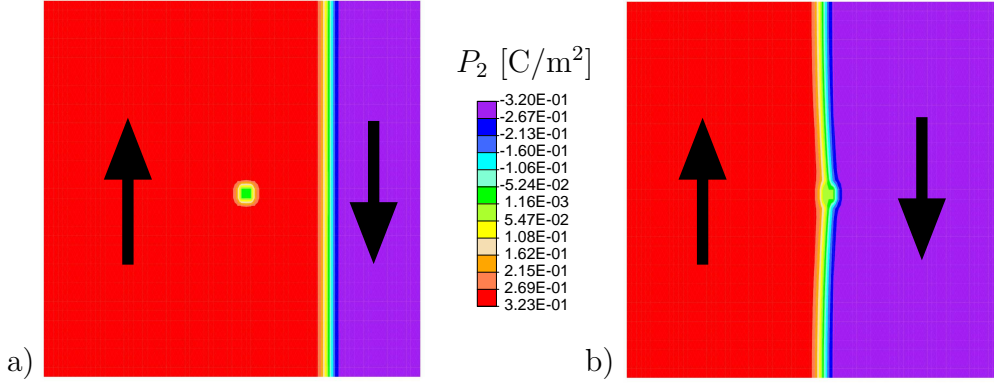


Figure 5.19: 180° domain wall approaching a polarization defect with  $\mathbf{P}^{\text{def}} = \mathbf{0}$ . a) initial configuration; b) pinning of the domain wall.

Figure 5.19 a) shows the initial 180° configuration with the defect in the center when the driving field of 1 MV/m is activated for a fixed time interval. For the defect polarization  $\mathbf{P}^{\text{def}} = \mathbf{0}$ , the simulation shows that the domain wall is pinned at the defect, cf. Fig. 5.19 b). The same result is obtained when a 90° interface is considered (which is not depicted).

The preceding simulations are extended by varying the defect polarization for both the 180° and the 90° domain wall. In the first case,  $\mathbf{P}^{\text{def}} = [0 \ P^{\text{def}}]^T$  in the range of  $-1.5 \leq P^{\text{def}}/P_0 \leq 1.5$ ; in the 90° case,  $\mathbf{P}^{\text{def}} = \frac{\sqrt{2}}{2} [P_0 \ P^{\text{def}}]^T$  for the interval  $-1.5 \leq P^{\text{def}}/P_0 \leq 1.5$ , which coincides with the interval of the 180° case. Then the average velocity of the domain wall is calculated from the interface positions at the beginning and the end of the simulation. These positions are obtained as the solution of  $P_2(x, y_0) = 0$  where  $y_0$  designates the center of the mesh in the vertical direction. The resulting average interface velocities are shown in Fig. 5.20. Negative values on the abscissa represent a “pre-aligned” spontaneous polarization while positive values indicate a non-switchable defect polarization. The interface velocity for the defect-free case is dashed for comparison. If  $\mathbf{P}^{\text{def}}$  is pre-aligned and close to the equilibrium polarization at the ratio of  $-1$ , domain walls are not pinned but instead are attracted by the defect, which explains their increased mobility compared to the defect-free case. On the other hand, as  $\mathbf{P}^{\text{def}}$  becomes more unfavorable, the domain wall mobility decreases. Domain wall pinning takes place where the two graphs lie below the dashed line.

If the driving field is strong enough, a defect with  $\mathbf{P}^{\text{def}} = \mathbf{0}$  can be overcome by the domain wall. Figure 5.21 illustrates the detachment of a 180° domain wall for an external field of 10 MV/m.



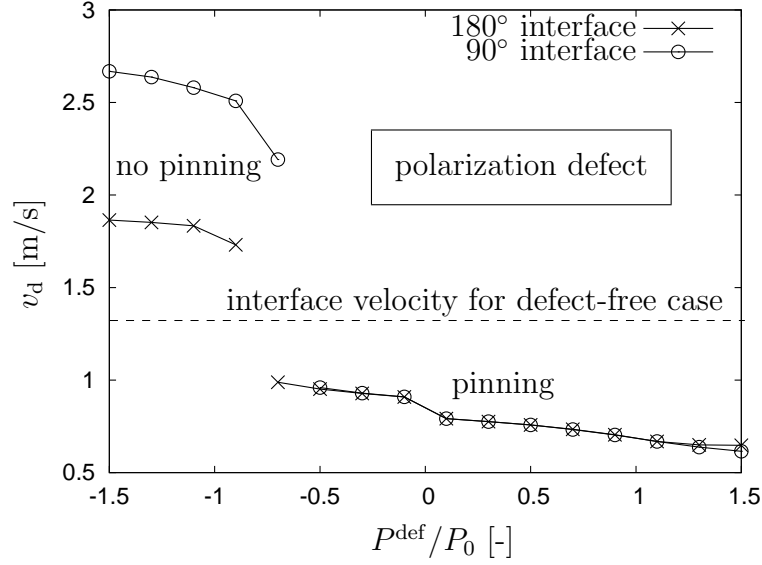


Figure 5.20: The effect of the polarization defect on the domain wall mobility, reflected by the average interface velocity  $v_d$ , depends on the value of the defect polarization. For ratios around  $-1$  (“pre-aligned”), the domain walls are more mobile as compared to the defect-free scenario and no pinning takes place. As indicated, domain wall pinning occurs for those parts of the two graphs which lie below the dashed line.

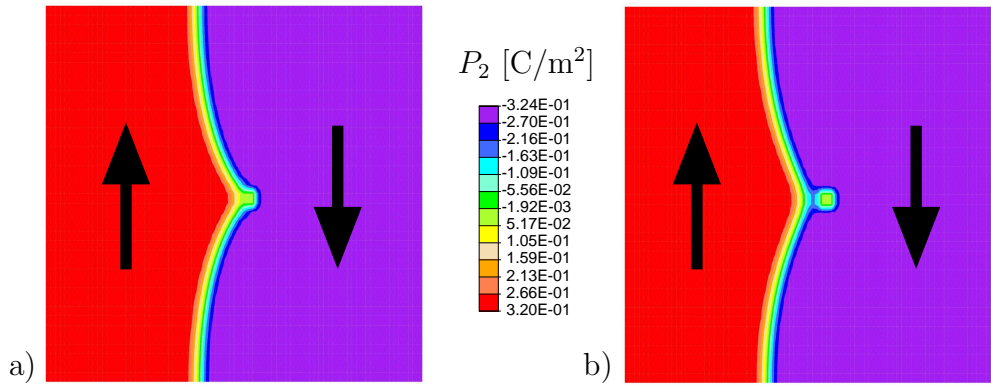


Figure 5.21:  $180^\circ$  domain wall overcoming a polarization defect with  $\mathbf{P}^{\text{def}} = \mathbf{0}$ , strong driving field. a) before detachment; b) after detachment from the defect.

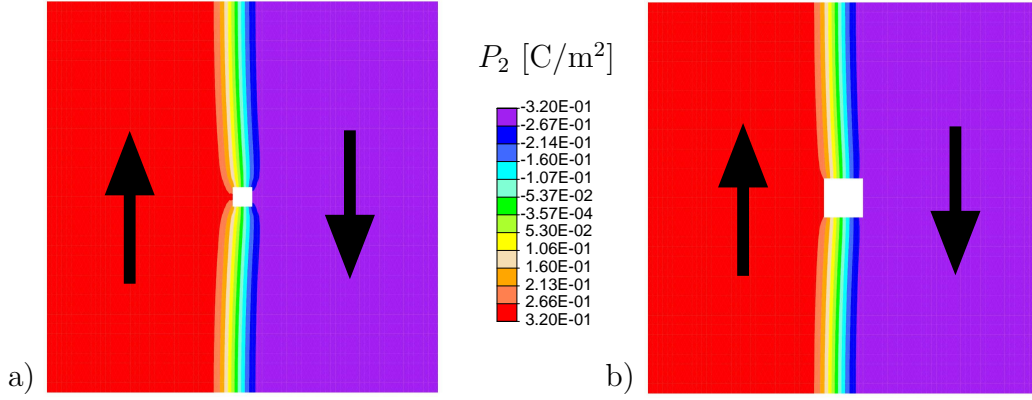


Figure 5.22: 180° domain wall pinned by a) small and b) large side defect.

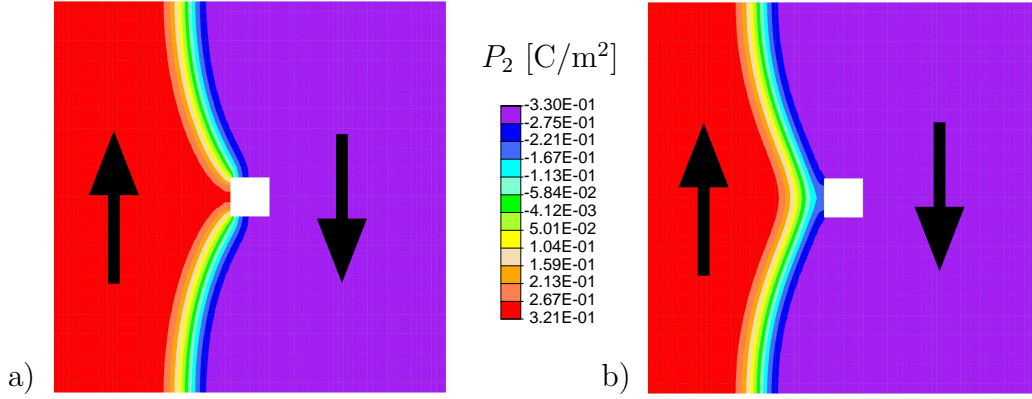


Figure 5.23: 180° domain wall overcoming side defect, strong driving field. a) before detachment; b) after detachment from the defect.

### Side defect

The third type of defect under investigation is a hole inside the material. The defect is modeled with a quadratic region in the center of the meshed region that remains unmeshed; its boundary is assumed to be charge and stress free. Starting with an initial configuration analogous to Fig. 5.19 a), the domain wall is driven toward the defect with a driving field of 1 MV/m. Figure 5.22 shows the final configurations for defect edge lengths of  $\epsilon/2$  and  $\epsilon$ . In both cases, the domain wall is pinned in the center of the defect. When the driving field is increased to 10 MV/m, the domain wall can overcome the defect; this situation is shown in Fig. 5.23.

A similar simulation was presented in Sec. 4.3.2 for gadolinium molybdate (GMO). There, the mobility of the domain wall was only slightly reduced and no pinning was observed. The two simulations differ in the material parameters,

the geometry and defect size, and in the modeling of the interfaces (sharp interface vs. phase field). Rerunning the presented phase field simulation using parameters for GMO makes no difference with respect to the pinning effect. Furthermore, the defect size is significantly smaller in the phase field simulation, and increasing its size would lead to an even stronger pinning effect. Therefore the different outcome of the simulations is to be attributed to the different interface modeling approaches. With regard to the GMO experiments, in which the defect reaches into the material only to a certain extent, a 3d simulation would allow for a realistic modeling of the defect geometry. Under such conditions, the driving field remains intact in regions sufficiently far away from the defect so that domain wall movement should be impeded only mildly.

### 5.3.4 Microstructure evolution

In some sense, the above simulations all belong to “microstructure evolution”; however, the view was limited to simple cases with just one interface. In this section, the focus lies on the evolution of more complex microstructures.

With respect to the phase field model, microstructure evolution depends mainly on the imposed boundary conditions, the initial configuration with respect to  $\mathbf{P}$ , and the relation between the specific interface energy vs. the electric enthalpy  $\tilde{H}^{\text{ent}}$ . For the first set of simulations, the initial conditions on  $\mathbf{P}$  are chosen to reflect the “least structured” state, i.e. a state of randomly oriented spontaneous polarization. Two cases are considered: case a)  $|\mathbf{P}(\mathbf{x}, 0)|/P_0 \ll 1$ , thus resembling conditions just below the Curie temperature, and case b)  $|\mathbf{P}(\mathbf{x}, 0)|/P_0 = 1$ . The mechanical boundary conditions are assumed stress free with statically determinate support. Electrically, both homogeneous Dirichlet and homogeneous Neumann conditions are considered.

Figure 5.24 illustrates the microstructure evolution in a region of  $40 \text{ nm} \times 40 \text{ nm}$  with  $\varphi^* = 0$  on the boundary for case a) and case b). At the beginning of the evolution, an intricate domain structure starts to form, becoming less complex as time proceeds. The case a) simulation evolves slower in terms of complexity reduction in the microstructure. However, for both simulations, the final configuration is a single domain state in which all interfaces have transcended the boundaries. The system has then reached its minimal energy configuration.

The previous simulation is repeated for the electrical boundary condition  $\mathbf{D} \cdot \mathbf{n} = 0$ . The microstructure evolution is qualitatively very similar to the one shown in Fig. 5.24 and is therefore not displayed here. The charge-free boundary condition necessitates either the spontaneous polarization to be aligned with the boundary

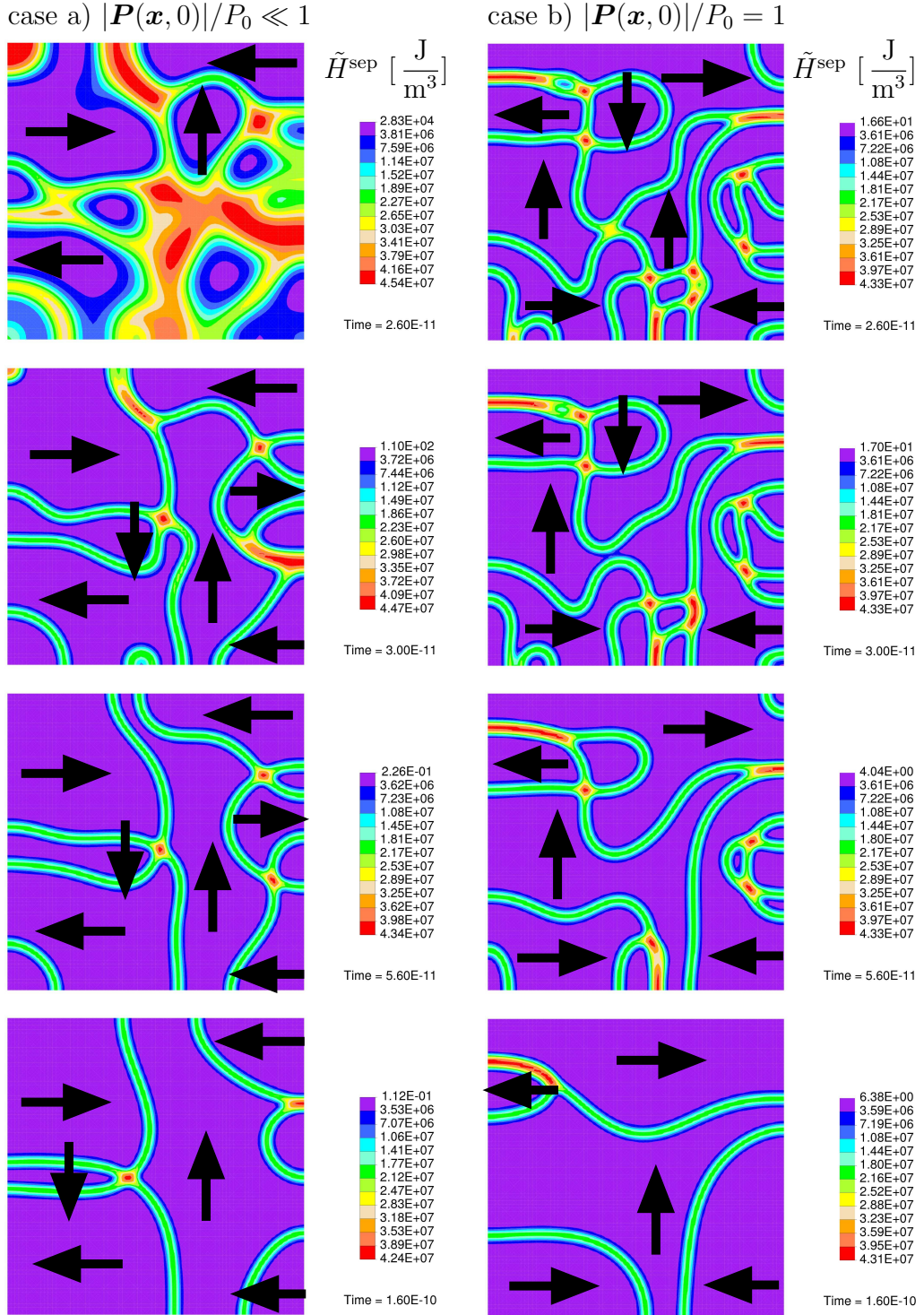


Figure 5.24: Domain structure evolution for  $\varphi^* = 0$  boundary condition starting with random initial polarizations case a) and case b).



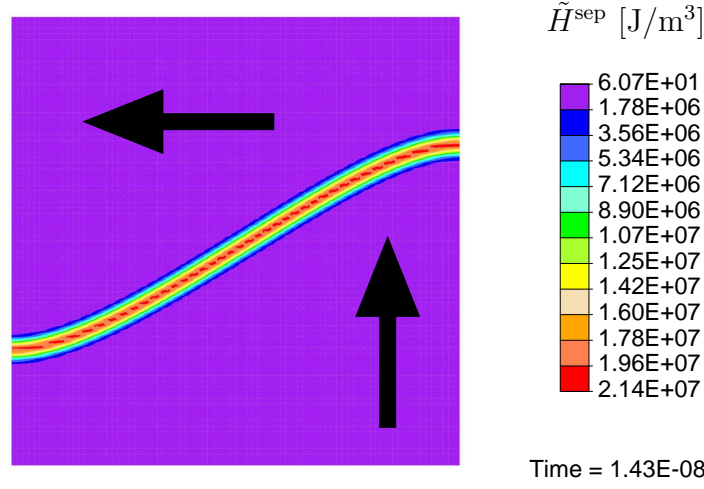


Figure 5.25: Final configuration for  $\mathbf{D} \cdot \mathbf{n} = 0$  on the boundary for both case a) and case b) random initial polarization, cf. Fig. 5.24.

or the compensation of misaligned spontaneous polarization by an electric field. The first possibility requires the formation of interfaces to create a vortex-like domain structure. In the present simulations, the final configurations for case a) and b) coincide with the configuration shown in Fig. 5.25. The equilibrated system contains just one  $90^\circ$  domain wall while the spontaneous polarization perpendicular to the boundary is compensated by the electric field.

The specific domain wall energy of PZT-5H is relatively high compared to other ferroelectrics (see e.g. PADILLA ET AL. 1996). The effect of different specific interface energies on the microstructure evolution is studied in the following set of simulations. By choosing a case a) random initial polarization in a region of  $20 \text{ nm} \times 10 \text{ nm}$  and by applying electrically homogeneous Neumann boundary conditions, the variation of the parameter  $\gamma$  leads to the equilibrium configurations shown in Fig. 5.26. For  $\gamma = \gamma_0$ , the cost of forming domain walls is high enough to allow for misaligned spontaneous polarization vectors at the boundary. As the creation of interfaces becomes more favorable with smaller values for  $\gamma$ , an increasing part of the boundary is characterized by aligned spontaneous polarization. It is completely aligned for  $\gamma = \frac{1}{20}\gamma_0$ , and the result is a vortex-like pattern with four  $90^\circ$  and one  $180^\circ$  domain wall.

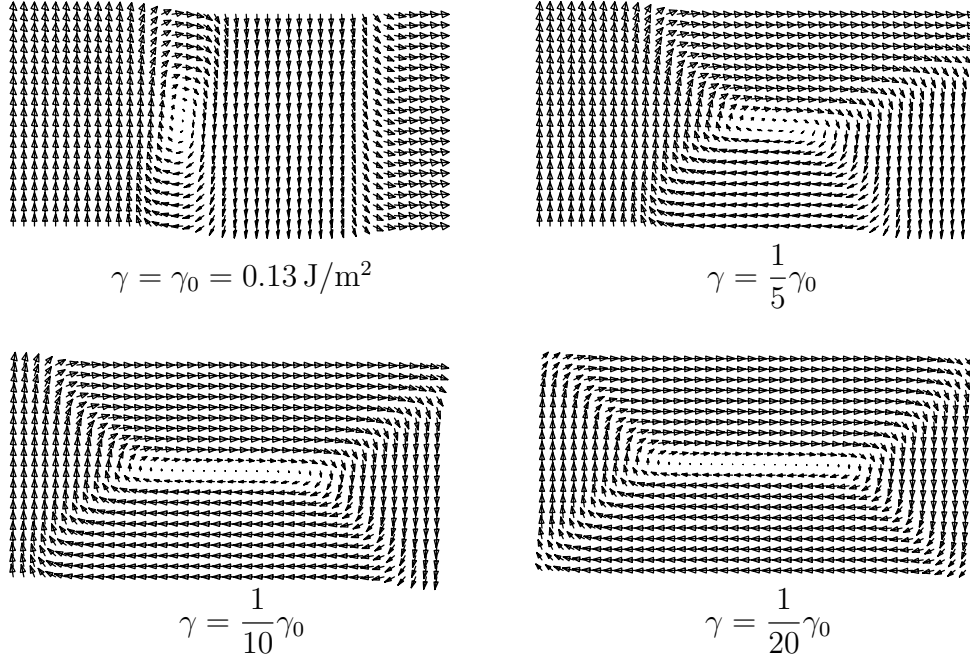


Figure 5.26: The value of the characteristic interface width  $\gamma$  has a profound influence on the outcome of the microstructure evolution which started with a case a) random initial polarization; charge-free boundary conditions are applied.

### 5.3.5 Bimodality

In SCHMITT ET AL. (2007), domain structures of unpoled  $\text{Pb}(\text{Zr}_{1-x}\text{Ti}_x)\text{O}_3$  samples with different Zr/Ti compositions were investigated in a detailed TEM study. The study reveals a characteristic configuration of alternating broad and narrow  $90^\circ$  domains, referred to as bimodal domain structure. Figure 5.27 shows bimodal domain configurations in two samples with different Zr/Ti compositions. The average ratio of the volume fractions of narrow and wide domain is approximately 1 : 2 with absolute widths of 66 nm and 147 nm.

In the following, an attempt is made to simulate bimodal domain configurations with the current phase field model. The question arises under which kind of initial and boundary conditions stationary bimodal states can be achieved. It is, for example, possible that an initially bimodal configuration evolves to a unimodal state, or that narrow domains lose width and eventually vanish completely.

The first simulation uses the (somewhat artificial) boundary condition  $\varphi^* = 0$  on the boundary  $\partial\mathcal{B}$ ; the initial bimodal configuration is shown in Fig. 5.28. The discretized region is  $600 \text{ nm} \times 100 \text{ nm}$  containing  $1200 \times 20$  elements. The mesh refinement in the  $x_1$ -direction gives an element edge length of 0.5 nm, one fourth

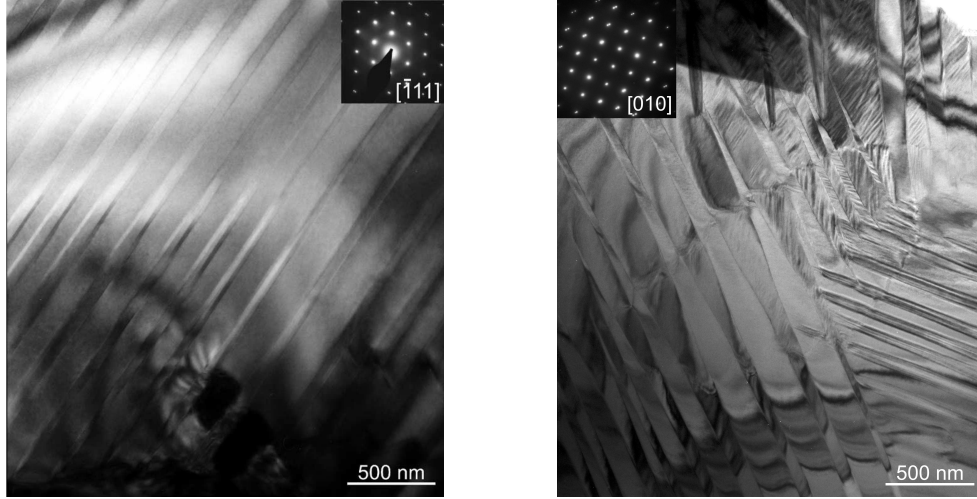


Figure 5.27: Bimodal 90° domain patterns in unpoled PZT samples, reprinted from SCHMITT ET AL. (2007). The left image is for tetragonal single phase  $\text{Pb}(\text{Zr}_{0.45}\text{Ti}_{0.55})\text{O}_3$ , the right image for  $\text{Pb}(\text{Zr}_{0.545}\text{Ti}_{0.455})\text{O}_3$ .

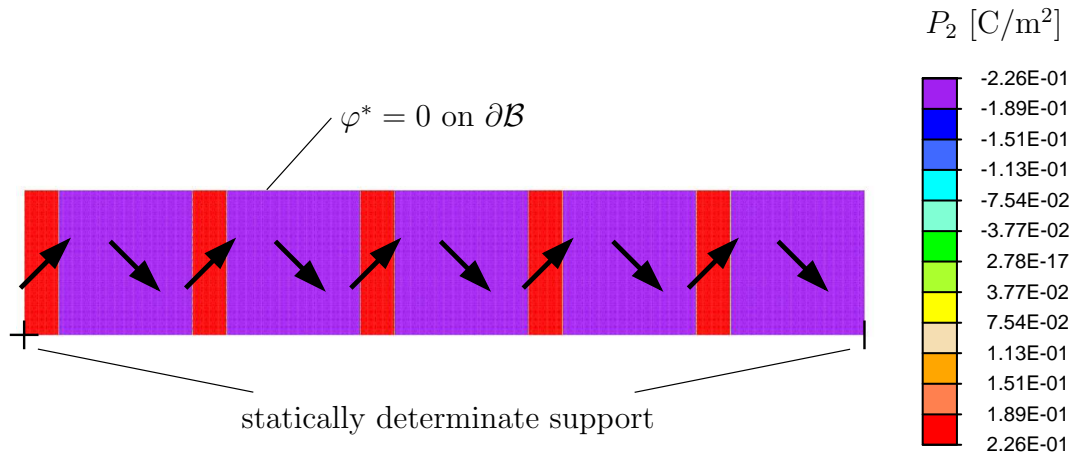


Figure 5.28: Bimodal initial conditions with  $\varphi^* = 0$  on the boundary and static support. The structure “dissolves” to a single domain poled in the  $\searrow$ -direction.

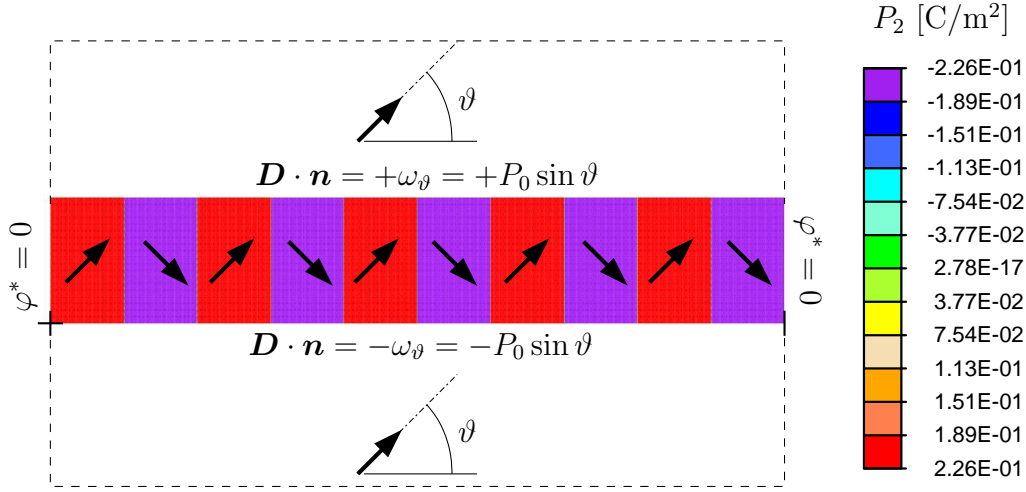


Figure 5.29: The initially unimodal configuration is bordered by regions with uniform polarization modeled with equivalent surface charge loadings  $\mp\omega_\vartheta$  at the top and bottom, respectively.

the value of  $\epsilon$ . The simulation is run until the system is in equilibrium, i.e.  $\dot{\mathbf{P}} = \mathbf{0}$  in  $\mathcal{B}$ . In the course of the time evolution, the widths of the narrow domains decrease, and the final state shows just one domain poled in the  $\searrow$ -direction. On the other hand, the use of a coarser mesh, i.e.  $800 \times 20$  elements, results in a stationary bimodal domain structure. The reason for this different outcome is not obvious at all. Since the system is free of external loading, the evolution of the order parameter is extremely slow. In the dissolving process, this evolution takes place in the interfacial regions where the spatial discretization plays an important role (cf. Sec. 5.3.2). The use of a coarser mesh may reduce the accuracy of the simulation so that the subtle changes in the microstructure observed when using a finer mesh cannot be resolved.

The boundary and initial conditions are now changed as depicted in Fig. 5.29. The initially unimodal configuration is assumed to be bordered by a uniformly polarized region at the top and bottom; this polarization is characterized by its angle  $\vartheta$  to the horizontal. Instead of discretizing the dashed regions in Fig. 5.29, the electric boundary condition  $\mathbf{D} \cdot \mathbf{n} = \pm\omega_\vartheta$  is applied to the top and bottom boundary, respectively. The strain mismatch at this boundary is ignored to isolate the electric effect on the domain evolution. The values of  $\omega_\vartheta$  are then given by  $\omega_\vartheta = P_0 \sin \vartheta$ . Specifically, the cases  $\vartheta = 0$ ,  $\vartheta = 4.05^\circ$ ,  $\vartheta = 8.13^\circ$ , and  $\vartheta = 16.4^\circ$  are considered.

The resulting stationary domain configurations are shown in Fig. 5.30. For  $\vartheta = 0$ , the final domain pattern is unimodal as is to be expected from symmetry



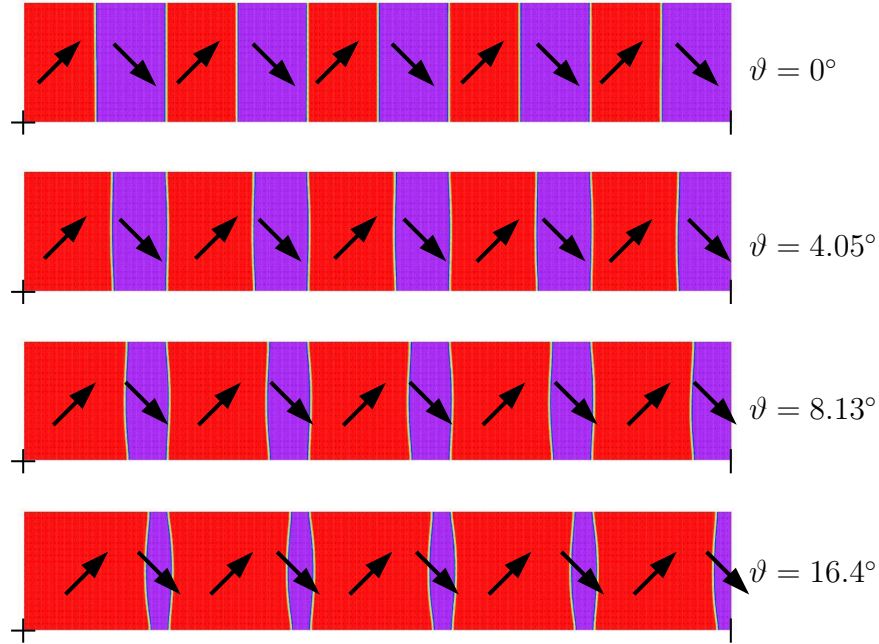


Figure 5.30: Resulting stationary domain configurations for different charge conditions at the top and bottom boundary, cf. Fig. 5.29. Bimodality becomes more pronounced as the surface charge density increases.

considerations. Since the boundary is charge free, all domains are electrically equitable. The situation changes if  $\vartheta > 0$ . The domains poled in the  $\nearrow$ -direction are electrically more favorable than the domains poled in the  $\nwarrow$ -direction, and bimodality becomes more distinct with increasing angles. For angles above roughly  $25^\circ$ , the narrow domains vanish, which eventually leads to homogeneously poled states.

In the last setting, the influence of mechanical loading is studied. The geometry and electrical loading conditions are identical to the case  $\omega_\vartheta = 0$  in the foregoing simulations. Additionally, a pure shear stress loading  $\tau$  is applied as indicated in Fig. 5.31. Although the electric boundary condition favors a unimodal domain pattern, the application of the mechanical load  $\tau = 50$  MPa results in a bimodal configuration as can be seen in the same figure. The bimodality is more pronounced for higher stresses; smaller values for  $\tau$  lead to a lesser degree of bimodality.

The simulations show that bimodal domain structures can be explained by the electrical conditions imposed by neighboring domains. On the other hand, bimodality can also be stress induced. It remains unclear whether the electrical or the mechanical effect dominates in the material; most likely, one will have to take both into account to understand the phenomenon of bimodality. Furthermore, the TEM

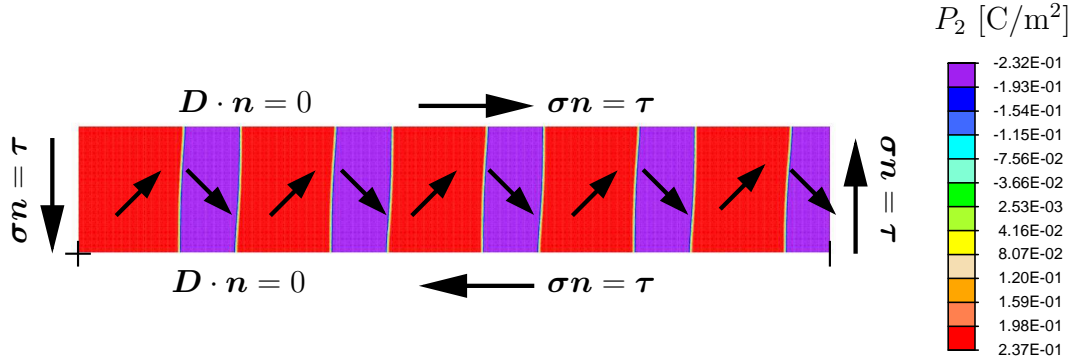


Figure 5.31: Resulting stationary domain configuration under pure shear stress loading and charge-free boundary conditions. The degree of bimodality is more pronounced as the strength of the shear stress is increased.

study in SCHMITT ET AL. (2007) reveals that the degree of bimodality depends on the Zr/Ti-composition of individual samples, some exhibiting bimodal domain structures to different degrees, others showing no bimodality in the investigated regions.

### 5.3.6 Wedge formation

Figure 5.32 shows a TEM image reprinted from SCHMITT ET AL. (2010) in which the two wedge-shaped domains form charge-neutral in-plane  $90^\circ$  interfaces with the domains bordering the flanks of the wedges. To the left, the wedges are bordered by another domain polarized in the opposite direction relative to the polarization

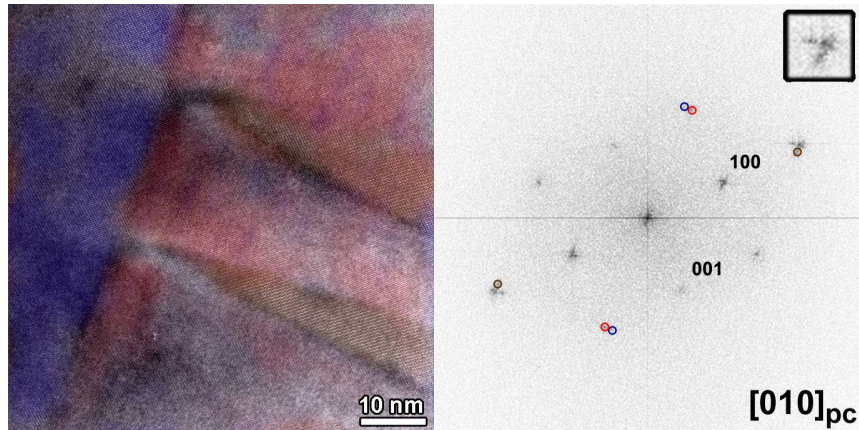


Figure 5.32: Wedge-shaped structure in  $90^\circ$  domain pattern, reprinted from SCHMITT ET AL. (2010).

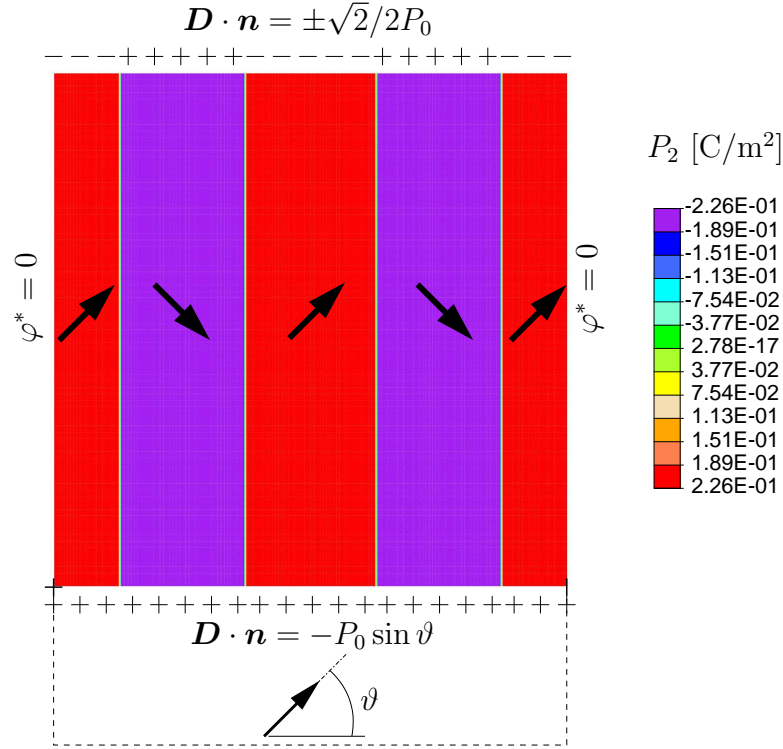


Figure 5.33: The initially unimodal configuration is subjected to the sketched electric boundary conditions; this causes the wedge-shaped structures shown in Fig. 5.34. The configuration shown in Fig. 5.32 is represented by  $\vartheta = 45^\circ$ .

of the wedges which results in a charged interface at the tips of the wedges.

This domain geometry is investigated with a set of simulations under the conditions sketched in Fig. 5.33. The discretized region is  $80 \text{ nm} \times 80 \text{ nm}$  with  $160 \times 80$  elements. The electrical boundary condition at the bottom is formulated analogously to the preceding simulations (cf. Fig. 5.29). On the top boundary, a prescribed charge density preserves the initially equidistant domain spacing. As before,  $\varphi^* = 0$  on the lateral sides.

The resulting stationary domain structures for  $\vartheta = 12.2^\circ$ ,  $\vartheta = 16.4^\circ$ ,  $\vartheta = 20.7^\circ$ , and  $\vartheta = 25.1^\circ$  are shown in Fig. 5.34. The wedges become more distinct with increasing values for  $\vartheta$ , just as was the case for the degree of bimodality in Fig. 5.31. For higher angles, including  $\vartheta = 45^\circ$ , which corresponds to the experimental setting shown in Fig. 5.32, the electrical mismatch causes the tips of the wedges to recede to the top boundary until a homogeneous poling state is reached. Since the mechanical mismatch at the bottom boundary was ignored, the formation of wedge-like structures can be explained solely on electrical grounds. The possibility of a mechanical or a combined cause can however not be excluded.

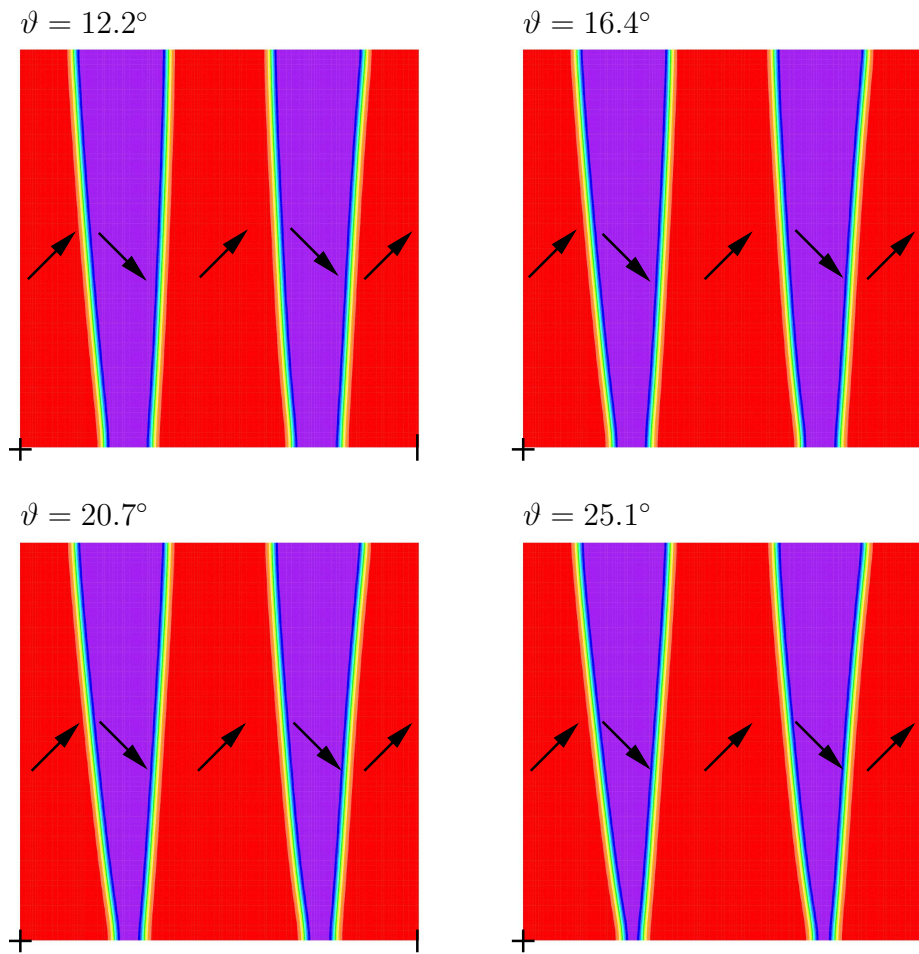


Figure 5.34: Resulting wedge-shaped domain configurations for different electrical loading conditions at the bottom boundary, cf. Fig. 5.33.

# Chapter 6

## Effective material behavior

The coercive field  $E_c$  is a macroscopic property of ferroelectric ceramics with regard to cyclic uniaxial electric loading. Using the material parameters stated in Sec. 5.3.1, one can obtain the numerical coercive field for the single crystal by applying an electric field to a region which is uniformly poled in the opposite direction. The resulting value for  $E_c$  exceeds experimentally determined coercive fields for single crystals by a factor of approximately one thousand, making a realistic simulation with the given set of material parameters impossible. The present phase field model, which applies primarily to microstructure evolution, can however be modified to allow for the simulation of the *macroscopic* behavior under uniaxial/multiaxial electric and mechanical loading; this is shown in the following.

### 6.1 Theory

The phase field model presented in Sec. 5.1 is altered in that microstructural aspects are ignored, i.e. domains and interfaces are not taken into account. This means that  $\nabla \mathbf{P} \equiv \mathbf{0}$ ; hence Eq. (5.16) becomes trivial. The parameters in Eq. (5.15) lose their physical meaning and have to undergo a metamorphosis under which the (macroscopic) coercive field  $E_c$  appears. The former separation potential becomes the *switching* potential  $\tilde{H}^{\text{sw}}$ :

$$\tilde{H}^{\text{sw}}(\mathbf{P}) = \kappa_{\text{sw}} P_0 E_c \tilde{\psi}(\mathbf{P}) , \quad (6.1)$$

where  $\kappa_{\text{sw}}$  is a calibration constant which ensures that the value of  $E_c$  coincides with the numerically obtained coercive field. The value of  $\kappa_{\text{sw}}$  is estimated using a reduced model in which  $\tilde{H}^{\text{ent}}(\mathbf{E}, \mathbf{P}) = -\mathbf{P} \cdot \mathbf{E}$ . The potential then reads

$$\tilde{H}(\mathbf{E}, \mathbf{P}) = -\mathbf{P} \cdot \mathbf{E} + \kappa_{\text{sw}} P_0 E_c \tilde{\psi}(\mathbf{P}) , \quad (6.2)$$



and the evolution equation is then given by

$$\dot{\mathbf{P}} = \beta^{-1} \left( \mathbf{E} - \kappa_{\text{sw}} P_0 E_c \frac{\partial \tilde{\psi}}{\partial \mathbf{P}} \right) . \quad (6.3)$$

The initial conditions are chosen as  $\mathbf{P}_0 = [0 \ P_0]^T$ , and a linearly increasing electric field is applied in the opposite direction of poling so that the solution only depends on  $P_2$ . Furthermore, quasi-static conditions are assumed with respect to the evolution of  $\mathbf{P}$ , i.e.  $\beta^{-1} \rightarrow \infty$ . In view of Eq. (6.3), the coercive field is reached when the right summand in the parenthesis becomes maximal, which means that the strongest electric field for which equilibrium can be achieved is reached. This is equivalent to the condition

$$\frac{\partial^2 \tilde{\psi}}{\partial P_2^2} = 0 . \quad (6.4)$$

Adopting  $\tilde{\psi}$  from Eq. (5.20) gives a sixth-degree polynomial in  $P_2$ . Given the coefficients  $a_i$  in Table 6.1, the resulting “critical” spontaneous polarization is  $P_c \approx 0.87P_0$ . Applying the equilibrium condition  $\dot{\mathbf{P}} = \mathbf{0}$  to Eq. (6.3) and evaluating the equation for  $P_2 = P_c$  and  $E_2 = E_c$  yields the equation for the determination of  $\kappa_{\text{sw}}$ :

$$\kappa_{\text{sw}} P_0 \frac{\partial \tilde{\psi}(0, P_c)}{\partial P_2} = 1 \quad \implies \quad \kappa_{\text{sw}} \approx 0.27 . \quad (6.5)$$

### Uniaxial electric and mechanical loading

The theoretical considerations are verified with a uniaxial electric and a mechanical loading scenario. Since the problem is homogeneous, the simulations are done using just one finite element subjected to the loading histories plotted in Fig. 6.1. The

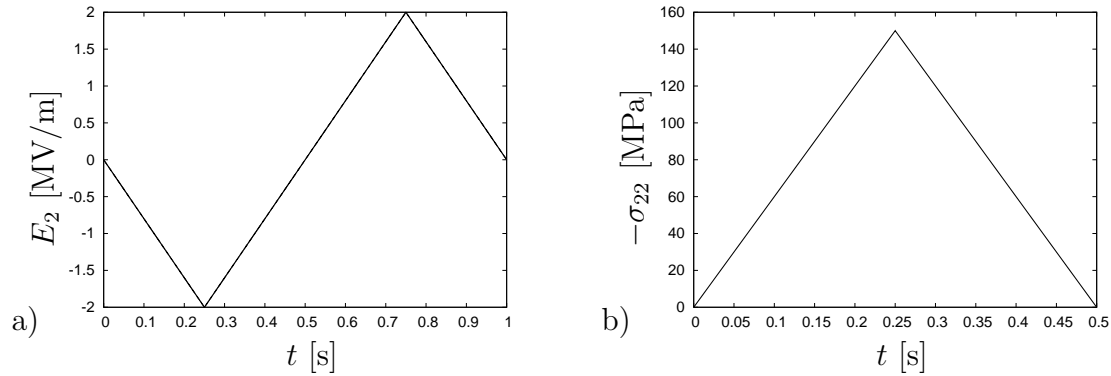


Figure 6.1: Loading histories for the uniaxial electric and mechanical loading simulations.

$P_0$ [C/m <sup>2</sup> ]	$\varepsilon^0$ [%]	$\beta^{-1}$ [A/(Vm)]	$E_c$ [MV/m]	
0.27	0.23	$1.7 \cdot 10^{-7}$	1.0	
$a_1$	$a_2$	$a_3$	$a_4$	$a_5$
1.0	-1.1	5.425	27.75	-11.55
$a_6$	$a_7$	$a_8$	$a_9$	
-122.05	6.225	259.75	127.9	

Table 6.1: Material parameters used in the simulations for the uniaxial loading scenarios given in Fig. 6.1.

remaining boundary conditions are given by statically determinate support and  $\varphi = 0$  or, in the case of electric loading, a prescribed potential difference. The parameters used in the simulations are stated in Eq. (6.8) and in Table 6.1. The initial poling state is assumed as fully poled in the  $x_2$ -direction.

The model responses for the two loading histories (Fig. 6.1) are plotted in Figs. 6.2 and 6.3 for three different mobilities  $\beta^{-1}$ . The typical dielectric and butterfly hysteresis behavior are qualitatively reproduced during the 180° switching process. The response is highly dependent on the mobility; the quasi-static loading case is approximated by the highest mobility. For lower values of  $\beta^{-1}$ , the evolution of  $\mathbf{P}$  “lags” behind the applied loading, which causes a shift in the coercive field as can be seen in both plots in Fig. 6.2. This dependency on the mobility translates directly to a change of the loading frequency: doubling the mobility has the same effect as reducing the loading frequency by half.

The compressive stress loading (Fig. 6.3) causes a 90° switching of spontaneous polarization. In the simulation, the crystal axes were rotated by 5° to break the symmetry of the problem with respect to  $x_2$ -axis. Failing to do so leads to a pathological model response, since the spontaneous polarization would change only in the  $P_2$ -component which corresponds to 180° switching. The effect of this slight rotation can be seen by taking a close look at the unloading interval in the  $\sigma_{22}$ - $\Delta D_2$  plot in which the tangent is not quite vertical.

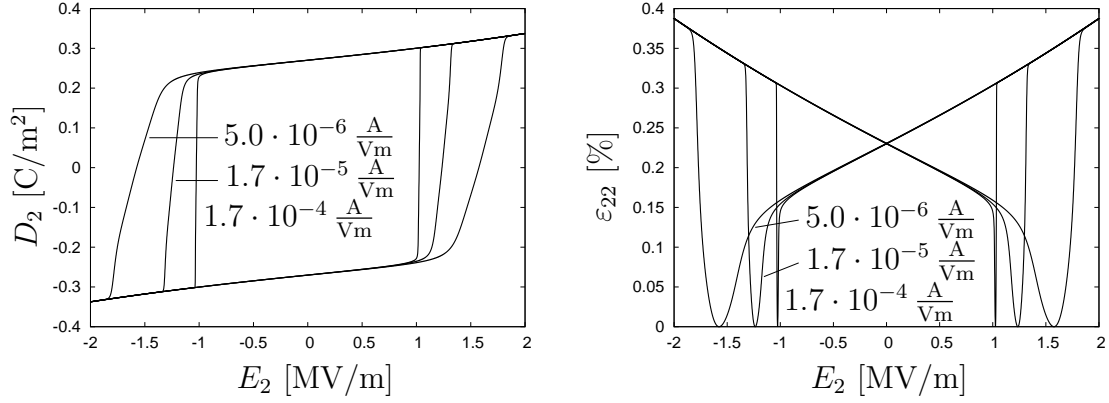


Figure 6.2: Dielectric and butterfly hystereses resulting from the uniaxial electric loading history shown in Fig. 6.1 a) for different mobilities  $\beta^{-1}$ . The quasi-static case is approximated by the highest value of  $\beta^{-1}$ .

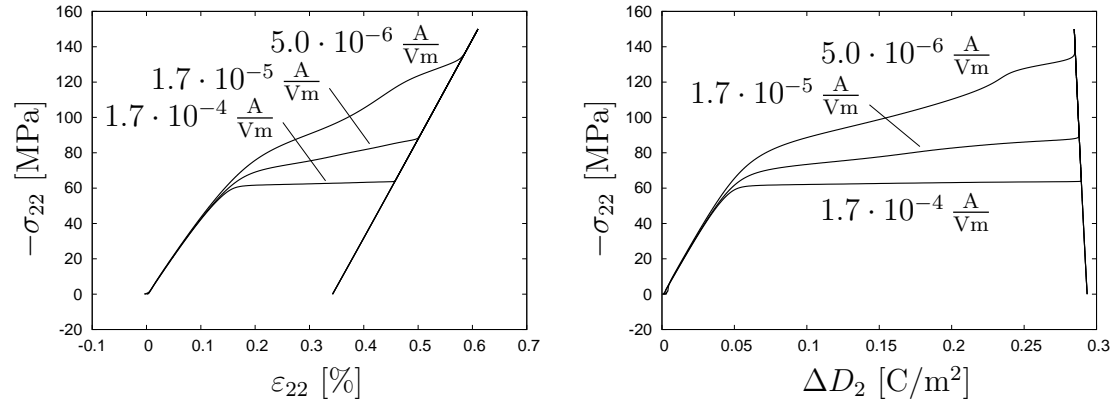


Figure 6.3: Stress hystereses resulting from the uniaxial mechanical loading history shown in Fig. 6.1 b) for different mobilities  $\beta^{-1}$  (cf. Fig. 6.2). The change in  $D_2$  is with respect to the initial value of  $D_2$ .



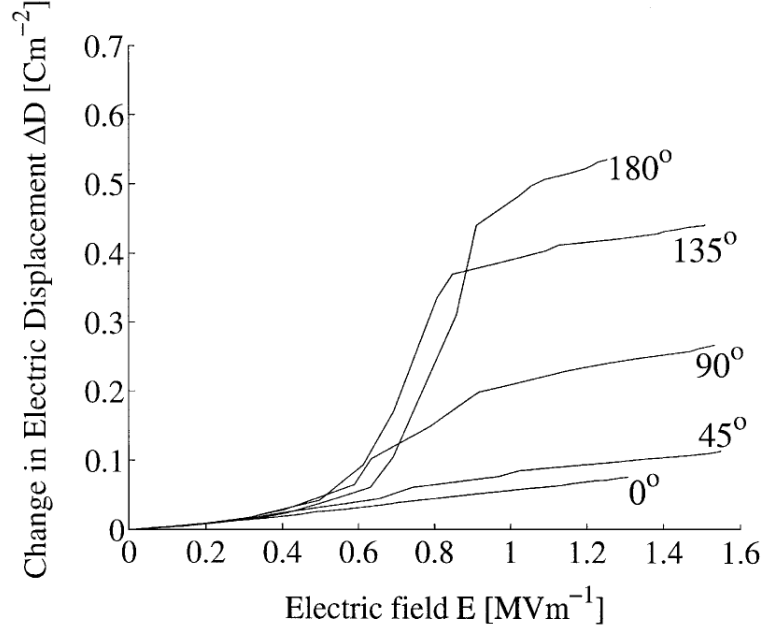


Figure 6.4: Measured dielectric responses for different angles  $\vartheta$ . Reprinted from HUBER & FLECK (2001).

## 6.2 Multiaxial loading

### Experiments by Huber and Fleck

HUBER & FLECK (2001) compared data obtained from a multi-axial loading experiment with results from three different material models: a self-consistent crystal plasticity model, a simplified viscoplastic crystal model, and a phenomenological model. In the experiments, a parent specimen of unpoled polycrystalline PZT-5H was poled by the application of an electric field of 1.5 MV/m for 100 s. Subsequently, the parent specimen was cut at different angles to the poling direction, so that an electric field could be applied at angles of  $0^\circ - 180^\circ$  to the polarization direction at increments of  $15^\circ$ . Each specimen was then subjected to an electric field which was increased from 0 to 1.5 MV/m and then decreased to 0 over a time of 30 s.

Figure 6.4 shows the measured electric displacement  $\Delta D$  for angles of  $0^\circ$ ,  $45^\circ$ ,  $90^\circ$ ,  $135^\circ$ , and  $180^\circ$ . The change in remanent polarization  $\Delta P_r$  was estimated by

$$\Delta P_r = \Delta D - \kappa E, \quad (6.6)$$

where the dielectric constant  $\kappa$  was calculated from the  $0^\circ$  poling curve. With this estimation the maximum value of switchable polarization was identified as

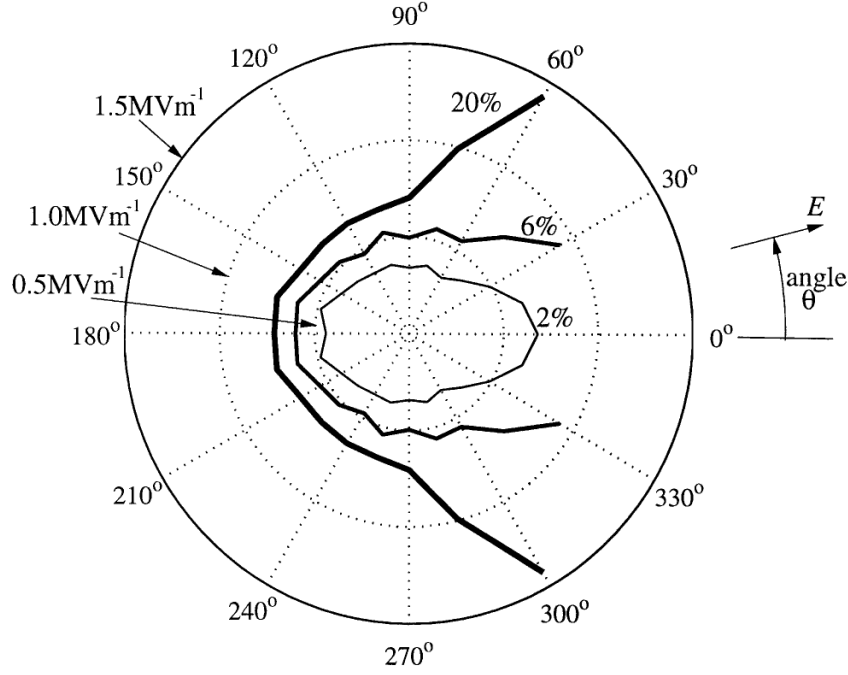


Figure 6.5: Measured offset yield surfaces, reprinted from HUBER & FLECK (2001). The angle  $\theta$  in the figure corresponds to the angle  $\vartheta$  used in this chapter.

$\Delta P_r^{\max} = 0.48 \text{ C/m}^2$ . The yield point was then defined as the electric field at which a fixed value of remanent polarization is reached. Measured yield surfaces for offset values of  $\Delta P_r = 0.01 \text{ C/m}^2$ ,  $0.03 \text{ C/m}^2$ , and  $0.1 \text{ C/m}^2$  (approximately 2%, 6%, and 20% of  $\Delta P_r^{\max}$  observed in the  $180^\circ$  specimen) are shown in Fig. 6.5.

### Orientation averaging

Due to the complexity of a ferroelectric polycrystal, it is currently too expensive to use the phase field model to simulate a realistically complex domain structure of multiple grains. However, as was shown in Sec. 6.1, the phase field model can be modified to simulate the effective  $180^\circ$  poling behavior. A simple averaging procedure over lattice orientations makes the modified phase field model usable for multiaxial loading scenarios.

An initially unpoled polycrystal consists of grains with different net polarizations which add up to a macroscopically vanishing net polarization. When the saturation polarization is reached during a poling experiment, each grain is polarized maximally in the poling direction. The initial unpoled state is now captured by considering  $n$  fully poled single crystals with rotated crystal axes at increments

of  $\Delta\vartheta = 360^\circ/n$ . The initial polarization for  $\vartheta = 0$  undergoes the same orthogonal transformation as the crystal axes. The poling process of the parent sample is then simulated by applying the loading history used in the cited experiment to each of the  $n$  crystals in a serial manner and averaging over the resulting field quantities with respect to the crystal orientations. The effective electric displacement, which is of interest here, is then given by

$$\langle \mathbf{D} \rangle = \frac{1}{n} \sum_{i=1}^n \mathbf{D}^{(i)} , \quad (6.7)$$

where  $\mathbf{D}^{(i)}$  is the electric displacement of the  $i$ -th grain. In the simulations, lattice orientations from  $0^\circ - 180^\circ$  by  $5^\circ$  increments are considered. The range between  $180^\circ - 360^\circ$  is captured by symmetry considerations.

## Results

The material parameters are identified by fitting the numerically obtained poling curve to the experimental  $180^\circ$  poling curve in Fig. 6.4. The values used in the simulations are given in Table 6.2 and furthermore by

$$\begin{aligned} \underline{\mathbb{C}} &= \begin{bmatrix} 7.56 & 3.4 & 0 \\ 3.4 & 7.56 & 0 \\ 0 & 0 & 2.08 \end{bmatrix} \cdot 10^{10} \frac{\text{N}}{\text{m}^2} , \\ \underline{\mathfrak{e}} &= \begin{bmatrix} 0 & 0 & 17.0 \\ -6.5 & 23.3 & 0 \end{bmatrix} \frac{\text{C}}{\text{m}^2} , \\ \underline{\epsilon} &= \begin{bmatrix} 1.0 & 0 \\ 0 & 1.0 \end{bmatrix} \cdot 10^{-9} \frac{\text{C}}{\text{Vm}} . \end{aligned} \quad (6.8)$$

Figure 6.6 shows the calculated change in electric displacement  $\Delta D$  for electric fields applied at  $0^\circ$ ,  $45^\circ$ ,  $90^\circ$ ,  $135^\circ$ , and  $180^\circ$  to the initial poling direction. The  $180^\circ$  curve is in reasonable agreement with the dotted experimental data, while the other curves reproduce the measured curves in Fig. 6.4 at least qualitatively.

The definition of reversible and irreversible polarization plays a crucial role in the construction of the yield surfaces. Experimentally, the dielectric permittivity  $\kappa$

$P_0$ [C/m <sup>2</sup> ]	$\epsilon^0$ [%]	$\beta^{-1}$ [A/(Vm)]	$E_c$ [MV/m]	
0.29	1.4	$1.7 \cdot 10^{-7}$	0.54	
$a_1$	$a_2$	$a_3$	$a_4$	$a_5$
1.0	-1.1	5.425	27.75	-11.55
$a_6$	$a_7$	$a_8$	$a_9$	
-122.05	6.225	259.75	127.9	

Table 6.2: Material parameters used in the simulations for the yield surfaces.

can be calculated from the initial slope  $\partial D/\partial E$ . With respect to the currently used model, the reversible polarization results from the dielectric permittivity *and partly* from the change in  $\mathbf{P}$  which evolves under external fields due to Eq. (6.3). The latter contribution is non-linear in the electric field (since  $\tilde{\psi}$  is non-linear) even for small signals so that one cannot identify an “effective”  $\kappa$  for the range of electric fields in question. Consequently, the split into reversible and irreversible polarization is ambiguous. In our case, the numerically computed slope  $\partial D/\partial E$  lies approximately between  $1.3 \cdot 10^{-8}$  C/(Vm) and  $3.5 \cdot 10^{-8}$  C/(Vm); as a working assumption,  $\kappa = 2.4 \cdot 10^{-8}$  C/(Vm) is used for the construction of the yield surfaces.

Each point of the yield surface is obtained analogously to Huber and Fleck’s procedure, i.e. the remanent polarization  $\Delta P_r$  is estimated by means of Eq. (6.6). Figure 6.7 shows the calculated yield surfaces for offset values of  $\Delta P_r = 0.01$  C/m<sup>2</sup>,  $0.03$  C/m<sup>2</sup>, and  $0.1$  C/m<sup>2</sup> (corresponding to approximately 2%, 6%, and 20% of  $\Delta P_r^{\max}$ ). The curves corresponding to 6% and 20% offset polarization are both open, i.e. the remanent polarization does not reach the 6% and 20% offset values in the range of  $\vartheta < 20^\circ$  and  $\vartheta < 55^\circ$ , respectively. Keeping in mind that the experiments were done at  $15^\circ$  increments ( $5^\circ$  was used in the simulation), this is in very good agreement with the experimental curves. All in all, the calculated yield surfaces are in excellent qualitative and good quantitative agreement with Huber and Fleck’s experimental data.

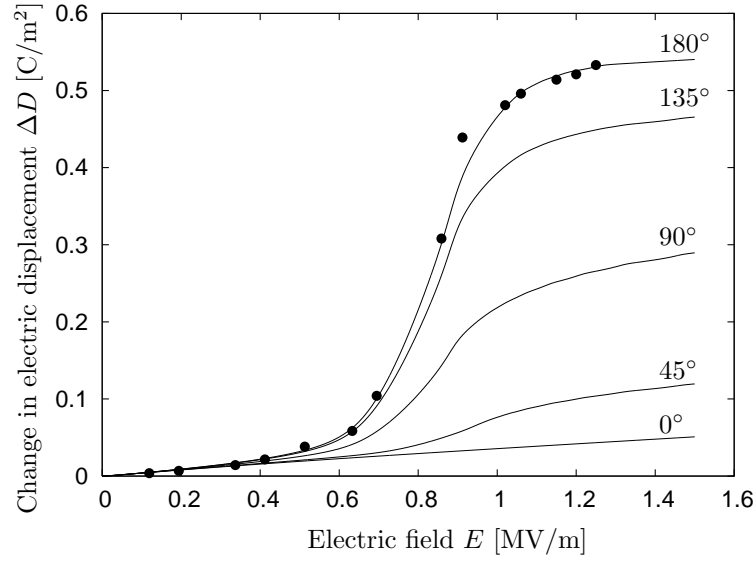


Figure 6.6: Calculated dielectric responses. The experimental values for  $\vartheta = 180^\circ$  are dotted (cf. Fig. 6.4).

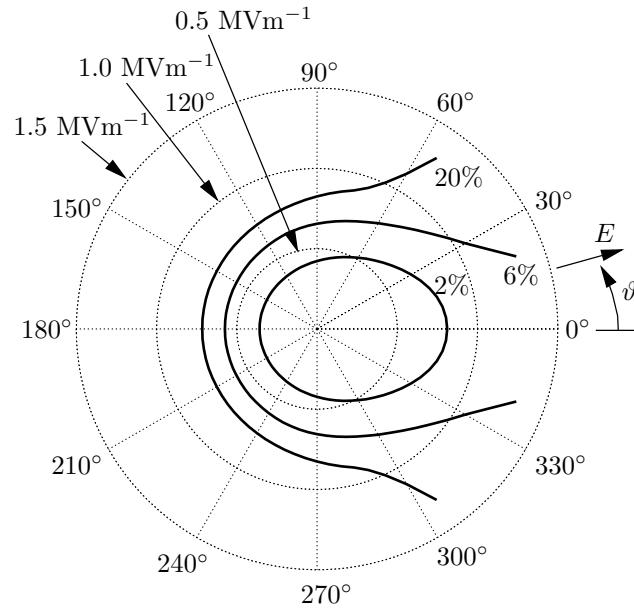


Figure 6.7: Calculated yield surfaces for offset values of 2%, 6%, and 20% of  $\Delta P_r^{\max}$  (cf. Fig. 6.5).



# Chapter 7

## Conclusion

In this work two different models for the simulation of the microstructure evolution in ferroelectrics have been presented. In the first approach, a ferroelectric domain wall is viewed as a singular surface across which the spontaneous polarization observes a discontinuity. The linear electromechanically coupled field problem is solved numerically with the finite element method for fixed domain wall positions. The resulting driving or configurational force is then used to postulate a kinetic law for the domain wall velocity. The simulations are concerned with the effect of different kinds of defects on the motion of a single planar domain wall in single crystal gadolinium molybdate. It is shown that a defect in one of the electrodes or a hole through the side faces can lead to domain wall pinning; the same result is obtained for different polarization defects.

The second approach is based on an order parameter concept which gives rise to a phase field model in which the spontaneous polarization becomes an independent field variable. By choosing an extended thermodynamical framework which postulates a balance law for a micro-force stress tensor, the constitutive relations and the evolution equation for the spontaneous polarization are derived from the phase field potential. The resulting equations are numerically solved with finite elements; the nodal degrees of freedom are the mechanical displacement, the electric potential, and the spontaneous polarization. Time integration is achieved by means of an implicit first order scheme which is implemented with a Newton-Raphson iteration at each time step. In a first set of simulations, the statics and kinetics of single  $180^\circ$  and  $90^\circ$  domain walls is studied, and the parameters introduced in the phase field model are verified. Another series of simulations is concerned with the effect of an electrode defect, a defect in the side faces, and various polarization defects on the mobility of  $180^\circ$  and  $90^\circ$  domain walls. Depending on the electric field strength and the size of a defect, the motion of a domain wall can be more or less affected

and domain wall pinning may take place. Bimodal domain patterns and wedge-like domain structures observed in PZT are ascribed to electrical and/or mechanical boundary conditions. Finally, a macroscopic material model is derived based on the electric enthalpy and the phase separation potential. The model is then used to calculate yield surfaces for the irreversible polarization which are compared with experimental findings in the literature.

The phase field model presented in this work offers a quite general and flexible tool for the simulation of the microstructure evolution in ferroelectric materials. It can be altered, for example, to allow for different unit cell structures and possible phase transitions between them. Other kinds of defects such as point defects can be implemented within the given finite element frame, see e.g. GOY (2010). An extension of the phase field to 3d can be done in a straightforward manner and would provide a more realistic basis to study domain structures and their evolution. Future work should examine the electric and mechanical conditions at grain boundaries in more detail to study the effects on the switching behavior within a grain. Furthermore one might try to incorporate the phase field model in a numerical multiscale homogenization scheme.



# Appendix

## A.1 Driving force acting on a 180° interface

Based on the geometry and boundary conditions sketched in Fig. 4.3, the driving force acting on a 180° interface can be approximated as shown in the following.

Inserting the configurational stress (4.2) into the driving force (4.6) and observing Eqs. (3.128)<sub>2</sub> and (3.141), one obtains

$$\begin{aligned}
 \tau_n &= [[H]] - \mathbf{n}_S \cdot ([[(\nabla \mathbf{u})^T \boldsymbol{\sigma}]] \mathbf{n}_S) + \mathbf{n}_S \cdot ([[ \mathbf{E} \otimes \mathbf{D} ]] \mathbf{n}_S) \\
 &= \frac{1}{2} [[(\boldsymbol{\varepsilon} - \boldsymbol{\varepsilon}^0) \cdot [\mathbb{C}(\boldsymbol{\varepsilon} - \boldsymbol{\varepsilon}^0)]]] - [[(\boldsymbol{\varepsilon} - \boldsymbol{\varepsilon}^0) \cdot (\mathbf{e}^T \mathbf{E})]] \\
 &\quad - \frac{1}{2} [[\mathbf{E} \cdot (\boldsymbol{\epsilon} \mathbf{E})]] - [[\mathbf{P}^0 \cdot \mathbf{E}]] - \mathbf{n}_S \cdot ([[(\nabla \mathbf{u})^T] \boldsymbol{\sigma} - [[\mathbf{E}] \otimes \mathbf{D}) \mathbf{n}_S].
 \end{aligned} \tag{A.1}$$

Given the material parameters in Eqs. (4.25)–(4.26) and provided that the electric field is not significantly stronger than approximately 1 MV/m, the terms in the second line of Eq. (A.1) and the first term in the third line can be considered to be small compared to  $[[\mathbf{P}^0 \cdot \mathbf{E}]]$ . By the same arguments, the last term in the third line of (A.1) can be dismissed, because the jumps of  $(\nabla \mathbf{u})^T$  and  $\mathbf{E}$  in the normal direction are small compared to  $[[\mathbf{P}^0 \cdot \mathbf{E}]]$ . This gives the approximation

$$\tau_n \approx [[\mathbf{P}^0 \cdot \mathbf{E}]] = 2P^0 E_2 \tag{A.2}$$

which is then used to obtain relations for the threshold field  $T_0$  and the interface mobility  $\mu$ .

## A.2 Comparison of phase field models

The phase field models used in ZHANG & BHATTACHARYA (2005) and SU & LANDIS (2007) use the total material polarization  $\mathbf{P}^{\text{mat}}$  as the order parameter, which leads to a structurally different thermodynamic potential compared to the

potential used here. These differences become apparent upon evaluating the constitutive equations and the resulting balance equations. The electric constitutive equations for the two models read

$$\mathbf{D} = \epsilon_0 \mathbf{E} + \mathbf{P}^{\text{mat}} \quad \text{and} \quad \mathbf{D} = \mathfrak{e}(\boldsymbol{\varepsilon} - \boldsymbol{\varepsilon}^0) + \boldsymbol{\epsilon} \mathbf{E} + \mathbf{P} , \quad (\text{A.3})$$

respectively. With the isotropic permittivity  $\boldsymbol{\epsilon} = \epsilon_{11} \mathbf{1}$ , the electric balance equations then become

$$\epsilon_0 \Delta \varphi - \text{div } \mathbf{P}^{\text{mat}} = 0 \quad \text{and} \quad \epsilon_{11} \Delta \varphi - \text{div}(\mathfrak{e}(\boldsymbol{\varepsilon} - \boldsymbol{\varepsilon}^0) + \mathbf{P}) = 0 \quad (\text{A.4})$$

or, in terms of functional dependencies,

$$\epsilon_0 \Delta \varphi - \text{div } \hat{\mathbf{f}}(\mathbf{P}^{\text{mat}}) = 0 \quad \text{and} \quad \epsilon_{11} \Delta \varphi - \text{div } \tilde{\mathbf{f}}(\boldsymbol{\varepsilon}, \mathbf{P}) = 0 , \quad (\text{A.5})$$

where  $\hat{\mathbf{f}}$  coincides with the identity function. The left hand side equations only depend on  $\varphi$  and the order parameter while the other also depend on the strain  $\boldsymbol{\varepsilon}$ . Also, the right hand side equations contain a linear dielectric and piezoelectric law which the other do not include. As a consequence, the cited models cannot be able to reproduce the linear dielectric and piezoelectric behavior in the way possible with the current phase field model.

The same applies for the mechanical balance equation. Using the same arrangement as above, one can compare the functional dependencies by writing

$$\begin{aligned} \text{div}(\hat{\mathbf{g}}_1(\boldsymbol{\varepsilon}) + \hat{\mathbf{g}}_2(\mathbf{P}^{\text{mat}}) + \hat{\mathbf{g}}_3(\boldsymbol{\varepsilon}, \mathbf{P}^{\text{mat}})) &= \mathbf{0} \quad \text{and} \\ \text{div}(\tilde{\mathbf{g}}_1(\boldsymbol{\varepsilon}) + \tilde{\mathbf{g}}_2(\mathbf{P}) + \tilde{\mathbf{g}}_3(\mathbf{E}, \mathbf{P})) &= \mathbf{0} , \end{aligned} \quad (\text{A.6})$$

where  $\hat{\mathbf{g}}_i$  and  $\tilde{\mathbf{g}}_i$  are tensor-valued functions. Both equations contain two functions that only depend on  $\boldsymbol{\varepsilon}$  and the order parameter, respectively (indices 1 and 2). The first equation shows no dependency on the electric field while the second reflects the linear relationship between the stress and the electric field.

The main differences between the present model and the models proposed in ZHANG & BHATTACHARYA (2005) and SU & LANDIS (2007) are: (1) the choice of the order parameter and (2) the structural differences in the phase field potential, which, as a consequence, result in a different mechanical and electric balance law and different constitutive equations. In the cited models, the dielectric and piezoelectric response is dependent on the non-linear evolution of the order parameter, and the field equations are not explicitly coupled in the strain and the electric field. On the contrary, the featured model implements linear constitutive laws and is fully coupled in  $\boldsymbol{\varepsilon}$  and  $\mathbf{E}$ .

### A.3 Alternative derivation of the evolution equation

The Ginzburg-Landau evolution equation can be derived from the internal dissipation inequality (3.140) by using  $\mathfrak{q} = \{\mathbf{P}, \nabla \mathbf{P}\}$  as internal variables, i.e.  $H = \tilde{H}(\boldsymbol{\varepsilon}, \mathbf{E}, \mathbf{P}, \nabla \mathbf{P})$ . Inserting this enthalpy in the dissipation inequality (3.140) with subsequent integration then gives

$$-\int_{\mathcal{B}} \frac{\partial \tilde{H}}{\partial \mathbf{P}} \cdot \dot{\mathbf{P}} \, dv - \int_{\mathcal{B}} \frac{\partial \tilde{H}}{\partial \nabla \mathbf{P}} \cdot \dot{\nabla \mathbf{P}} \, dv \geq 0. \quad (\text{A.7})$$

After integration by parts one obtains

$$-\int_{\mathcal{B}} \left( \frac{\partial \tilde{H}}{\partial \mathbf{P}} - \operatorname{div} \frac{\partial \tilde{H}}{\partial \nabla \mathbf{P}} \right) \cdot \dot{\mathbf{P}} \, dv - \int_{\partial \mathcal{B}} \left( \frac{\partial \tilde{H}}{\partial \nabla \mathbf{P}} \mathbf{n} \right) \cdot \dot{\mathbf{P}} \, da \geq 0. \quad (\text{A.8})$$

The balance of energy (3.99) contains the tacit assumption that the surface stress thermodynamically conjugate to  $\dot{\mathbf{P}}$  vanishes everywhere on the boundary. As shown in Sec. 5.1.1, where a stress system of micro-forces is considered, the expression  $\partial_{\nabla \mathbf{P}} \tilde{H}$  in (A.8) is identical to the micro-force stress tensor. Because of the *a priori* assumption that this stress vanishes on the boundary, the dissipation inequality can be satisfied with the Ginzburg-Landau equation

$$\dot{\mathbf{P}} = -\beta^{-1} \left( \frac{\partial \tilde{H}}{\partial \mathbf{P}} - \operatorname{div} \frac{\partial \tilde{H}}{\partial \nabla \mathbf{P}} \right) \quad (\text{A.9})$$

which is equivalent to the evolution equation (5.12) obtained in Sec. 5.1.1.

### A.4 Parameters of the phase separation potential

It is not a trivial task to determine the coefficients  $a_i$  in the phase separation potential (5.20). In Sec. 5.3.2–5.3.5 the reduced sixth-order polynomial

$$\tilde{\psi} = 1 + \frac{a_1}{P_0^2} (P_1^2 + P_2^2) + \frac{a_2}{P_0^4} (P_1^4 + P_2^4) + \frac{a_3}{P_0^4} P_1^2 P_2^2 + \frac{a_4}{P_0^6} (P_1^6 + P_2^6) \quad (\text{A.10})$$

is used. This polynomial is already normalized so that  $\tilde{\psi}(0,0) = 1$ ; symmetry considerations regarding the interchangeability of  $P_1$  and  $P_2$  as well as of  $\pm P_1$

(and  $\pm P_2$ ) are already taken into account by virtue of its construction. The following conditions are used for the determination of the four coefficients in  $\tilde{\psi}$ . The location and function value of the local minima are defined by

$$\tilde{\psi}(P_0, 0) = 0 , \quad (\text{A.11})$$

$$\partial_{P_1} \tilde{\psi}(P_0, 0) = 0 . \quad (\text{A.12})$$

Another prominent point is the  $90^\circ$  switching barrier which is located at an angle of  $45^\circ$  to the crystal axes. Location and function value are specified by

$$\tilde{\psi}(\iota P_0, \iota P_0) = \psi_{90} , \quad (\text{A.13})$$

$$\partial_{P_1} \tilde{\psi}(\iota P_0, \iota P_0) = 0 \quad (\text{A.14})$$

with  $0 < \iota < 1$ . This gives the linear system of equations

$$\begin{bmatrix} 1 & 1 & 0 & 1 \\ 2 & 4 & 0 & 6 \\ 2\iota^2 & 2\iota^4 & \iota^4 & 2\iota^6 \\ 2\iota & 4\iota^3 & 2\iota^3 & 6\iota^5 \end{bmatrix} \begin{bmatrix} a_1 \\ a_2 \\ a_3 \\ a_4 \end{bmatrix} = \begin{bmatrix} 0 \\ 0 \\ \psi_{90} \\ 0 \end{bmatrix} . \quad (\text{A.15})$$

In Sec. 5.3.2, the parameter  $\psi_{90}$  is shown to be in a linear relationship with the specific  $90^\circ$  interface energy and can thus be physically interpreted. The value of  $\iota$  is determined with a condition that preserves the shape of  $\tilde{\psi}$  for varying  $\psi_{90}$ . Using  $\psi_{90} = 0.5$  and  $\iota = 0.63$ , the four coefficients  $a_i$  are calculated and subsequently used in the evaluation of the (somewhat arbitrary) condition

$$\int_{-P_0}^{P_0} \tilde{\psi}(P_1, 0) dP_1 = \frac{6}{5} P_0 . \quad (\text{A.16})$$

This gives an equation which contains  $\psi_{90}$  and  $\iota$ , and with a Taylor expansion around  $\psi_{90} = 0.5$  one obtains

$$\iota = 0.89 - 0.52\psi_{90} - 0.44(\psi_{90} - 0.5)^2 , \quad (\text{A.17})$$

which ensures that the shape of  $\tilde{\psi}$  does not degenerate.

## A.5 Element stiffness and damping matrix

The element stiffness matrix is obtained by differentiation of the element residuals (5.56)–(5.58) with respect to the nodal degrees of freedom of the element as

stated in Eq. (5.68). For that purpose, the discretized constitutive equations

$$\underline{\sigma} = \underline{\mathbb{C}} (\underline{\varepsilon} - \underline{\varepsilon}^0) - \underline{\mathfrak{e}}^T \underline{E}, \quad \underline{D} = \underline{\mathfrak{e}} (\underline{\varepsilon} - \underline{\varepsilon}^0) + \underline{\epsilon} \underline{E} + \underline{P} \quad (\text{A.18})$$

are stated besides the chain rule for the derivatives with respect to  $\underline{P}^J$  in Eq. (5.58):

$$\frac{\partial}{\partial \underline{P}^J} = \frac{\partial}{\partial \underline{P}} \frac{\partial \underline{P}}{\partial \underline{P}^J} = N_P^J \frac{\partial}{\partial \underline{P}}. \quad (\text{A.19})$$

Carrying out the partial derivatives gives

$$\underline{K}_{\sigma\sigma}^{IJ} = - \int_{\mathcal{B}^e} (\underline{B}_u^I)^T \underline{\mathbb{C}} \underline{B}_u^J dv, \quad (\text{A.20})$$

$$\underline{K}_{\sigma D}^{IJ} = - \int_{\mathcal{B}^e} (\underline{B}_u^I)^T \underline{\mathfrak{e}}^T \underline{B}_\varphi^J dv, \quad (\text{A.21})$$

$$\underline{K}_{\sigma P}^{IJ} = \int_{\mathcal{B}^e} (\underline{B}_u^I)^T \left( \underline{\mathbb{C}} \frac{\partial \underline{\varepsilon}^0}{\partial \underline{P}} + \frac{\partial \underline{\mathfrak{e}}^T}{\partial \underline{P}} \underline{E} \right) N_P^J dv, \quad (\text{A.22})$$

$$\underline{K}_{D\sigma}^{IJ} = - \int_{\mathcal{B}^e} (\underline{B}_\varphi^I)^T \underline{\mathfrak{e}} \underline{B}_u^J dv, \quad (\text{A.23})$$

$$K_{DD}^{IJ} = \int_{\mathcal{B}^e} (\underline{B}_\varphi^I)^T \underline{\epsilon} \underline{B}_\varphi^J dv, \quad (\text{A.24})$$

$$\underline{K}_{DP}^{IJ} = - \int_{\mathcal{B}^e} (\underline{B}_\varphi^I)^T \left[ \frac{\partial \underline{\mathfrak{e}}}{\partial \underline{P}} (\underline{\varepsilon} - \underline{\varepsilon}^0) - \underline{\mathfrak{e}} \frac{\partial \underline{\varepsilon}^0}{\partial \underline{P}} + \underline{1} \right] N_P^J dv, \quad (\text{A.25})$$

$$\underline{K}_{P\sigma}^{IJ} = \int_{\mathcal{B}^e} N_P^I \left( \frac{\partial (\underline{\varepsilon}^0)^T}{\partial \underline{P}} \underline{\mathbb{C}} + \underline{E}^T \frac{\partial \underline{\mathfrak{e}}}{\partial \underline{P}} \right) \underline{B}_u^J dv, \quad (\text{A.26})$$

$$\underline{K}_{PD}^{IJ} = - \int_{\mathcal{B}^e} N_P^I \left[ - \frac{\partial (\underline{\varepsilon}^0)^T}{\partial \underline{P}} \underline{\mathfrak{e}}^T + (\underline{\varepsilon} - \underline{\varepsilon}^0)^T \frac{\partial \underline{\mathfrak{e}}^T}{\partial \underline{P}} + \underline{1} \right] \underline{B}_\varphi^J dv, \quad (\text{A.27})$$

$$\begin{aligned} \underline{K}_{PP}^{IJ} = & - \int_{\mathcal{B}^e} \left\{ - N_P^I \left[ \frac{\partial^2 (\underline{\varepsilon}^0)^T}{\partial \underline{P}^2} \underline{\sigma} - \frac{\partial (\underline{\varepsilon}^0)^T}{\partial \underline{P}} \left( \underline{\mathbb{C}} \frac{\partial \underline{\varepsilon}^0}{\partial \underline{P}} + \frac{\partial \underline{\mathfrak{e}}^T}{\partial \underline{P}} \underline{E} \right) \right] N_P^J \right. \\ & - N_P^I \left( - \frac{\partial (\underline{\varepsilon}^0)^T}{\partial \underline{P}} \frac{\partial \underline{\mathfrak{e}}^T}{\partial \underline{P}} + (\underline{\varepsilon} - \underline{\varepsilon}^0)^T \frac{\partial^2 \underline{\mathfrak{e}}^T}{\partial \underline{P}^2} \right) N_P^J \underline{E} \\ & \left. + N_P^I \kappa_s \frac{G}{\epsilon} \frac{\partial^2 \tilde{\psi}}{\partial \underline{P}^2} N_P^J + \kappa_i \frac{G\epsilon}{P_0^2} (\underline{B}_P^I)^T \underline{B}_P^J \right\} dv. \end{aligned} \quad (\text{A.28})$$

The remaining derivatives of  $\underline{\mathfrak{e}}$ ,  $\underline{\varepsilon}^0$ , and  $\tilde{\psi}$  with respect to  $\underline{P}$  follow directly — observing the Voigt notation in  $\underline{\varepsilon}^0$  — from Eqs. (5.18)–(5.20) and are not carried out explicitly here. Evaluation of Eq. (5.69) gives

$$\underline{D}_{PP}^{IJ} = - \int_{\mathcal{B}^e} N_P^I \underline{\beta} N_P^J dv, \quad (\text{A.29})$$

the remaining contributions vanish identically.



# Bibliography

- Ahluwalja, R. & Cao, W. (2000), ‘Influence of dipolar defects on switching behavior in ferroelectrics’, *Phys. Rev. B* **63**(1), 012103.
- Ahluwalja, R. & Cao, W. (2003), ‘Effect of surface induced nucleation of ferroelastic domains on polarization switching in constrained ferroelectrics’, *J. Appl. Phys.* **93**(1), 537–544.
- Ahluwalja, R., Lookman, T., Saxena, A. & Cao, W. (2005), ‘Domain-size dependence of piezoelectric properties of ferroelectrics’, *Phys. Rev. B* **72**(1), 014112.
- Allik, H. & Hughes, T. J. R. (1970), ‘Finite element method for piezoelectric vibration’, *Int. J. Numer. Meth. Eng.* **2**(2), 151–157.
- Bhattacharya, K. & Higgins, M. J. (2009), ‘Imaging ferroelectric hysteresis and domain wall pinning’, *arXiv:1001.0099*.
- Bhattacharya, K. & Ravichandran, G. (2003), ‘Ferroelectric perovskites for electromechanical actuation’, *Acta Mater.* **51**(19), 5941–5960.
- Brennan, C. (1993), ‘Model of ferroelectric fatigue due to defect/domain interactions’, *Ferroelectrics* **150**(1), 199–208.
- Cahn, J. W. & Hilliard, J. E. (1958), ‘Free energy of a nonuniform system; I. Interfacial free energy’, *J. Chem. Phys.* **28**(2), 258–267.
- Cao, W. & Barsch, G. R. (1990), ‘Landau-Ginzburg model of interphase boundaries in improper ferroelastic Perovskites of  $d_{4h}^{18}$  symmetry’, *Phys. Rev. B* **41**(7), 4334–4348.
- Cao, W., Barsch, G. R. & Krumhansl, J. A. (1990), ‘Quasi-one-dimensional solutions for domain walls and their constraints in improper ferroelastics’, *Phys. Rev. B* **42**(10), 6396–6401.

- Cao, W. & Cross, L. E. (1991), ‘Theory of tetragonal twin structures in ferroelectric perovskites with a first-order phase transition’, *Phys. Rev. B* **44**(1), 5–12.
- Chen, X., Fang, D. N. & Hwang, K. C. (1997), ‘Micromechanics simulation of ferroelectric polarization switching’, *Acta Mater.* **45**(8), 3181–3189.
- Chong, K. B., Guiu, F. & Reece, M. J. (2008), ‘Thermal activation of ferroelectric switching’, *J. Appl. Phys.* **103**(1), 014101.
- Choudhury, S., Li, Y. L., Krill III, C. E. & Chen, L.-Q. (2005), ‘Phase-field simulation of polarization switching and domain evolution in ferroelectric polycrystals’, *Acta Mater.* **53**(20), 5313–5321.
- Choudhury, S., Li, Y. L., Krill III, C. E. & Chen, L.-Q. (2007), ‘Effect of grain orientation and grain size on ferroelectric domain switching and evolution: Phase field simulations’, *Acta Mater.* **55**(4), 1415–1426.
- Coldren, L. A., Lemons, R. A., Glass, A. M. & Bonner, W. A. (1977), ‘Electronically variable delay using ferroelastic-ferroelectrics’, *Appl. Phys. Lett.* **30**(10), 506–508.
- Coleman, B. D. & Noll, W. (1963), ‘The thermodynamics of elastic materials with heat conduction and viscosity’, *Arch. Rational Mech. Anal.* **13**(1), 167–178.
- Colla, E. L., Hong, S., Taylor, D. V., Tagantsev, A. K., Setter, N. & No, K. (1998), ‘Direct observation of region by region suppression of the switchable polarization (fatigue) in  $\text{Pb}(\text{Zr,Ti})\text{O}_3$  thin film capacitors with Pt electrodes’, *Appl. Phys. Lett.* **72**(21), 2763–2765.
- Devonshire, A. F. (1949), ‘Theory of barium titanate — Part I’, *Phil. Mag. Ser. 7* **40**(309), 1040–1063.
- Devonshire, A. F. (1954), ‘Theory of ferroelectrics’, *Adv. Phys.* **3**(10), 85–130.
- Ding, H. & Chen, W. (2001), *Three dimensional problems of piezoelectricity*, Nova Science Publishers, Inc., Huntington, New York.
- Eringen, A. C. (1963), ‘On the foundations of electroelastostatics’, *Int. J. Eng. Sci.* **1**(1), 127–153.
- Fließbach, T. (2008), *Elektrodynamik*, Vol. II of *Lehrbuch zur Theoretischen Physik*, 5th edn, Spektrum Akademischer Verlag, Heidelberg.



- Flippen, R. B. (1975), ‘Domain wall dynamics in ferroelectric/ferroelastic molybdates’, *J. Appl. Phys.* **46**(3), 1068–1071.
- Foeth, M., Sfera, A., Stadelmann, P. & Buffat, P.-A. (1999), ‘A comparison of HREM and weak beam transmission electron microscopy for the quantitative measurement of the thickness of ferroelectric domain walls’, *J. Electron Microsc.* **48**(6), 717–723.
- Fried, E. & Gurtin, M. E. (1993), ‘Continuum theory of thermally induced phase transitions based on an order parameter’, *Phys. D: Nonlinear Phenomena* **68**(3–4), 326–343.
- Fried, E. & Gurtin, M. E. (1994), ‘Dynamic solid-solid transitions with phase characterized by an order parameter’, *Phys. D: Nonlinear Phenomena* **72**(4), 287–308.
- Goy, O. (2010), Point defects in piezoelectric materials – continuum mechanical modelling and numerical simulation, PhD thesis, Technische Universität Kaiserslautern, Kaiserslautern.
- Gross, D., Kolling, S., Mueller, R. & Schmidt, I. (2003), ‘Configurational forces and their application in solid mechanics’, *Eur. J. Mech. A/Solids* **22**(5), 669–692.
- Gruverman, A., Auciello, O. & Tokumoto, H. (1996), ‘Investigation of fatigue effects in Pb(Zr,Ti)O<sub>3</sub> films’, *Appl. Phys. Lett.* **69**(21), 3191–3193.
- Gurtin, M. E. (1981), *An introduction to continuum mechanics*, Academic Press, New York, London, Toronto, Sidney, San Francisco.
- Gurtin, M. E. (1991), ‘On thermomechanical laws for the motion of a phase interface’, *J. Appl. Math. Phys. (ZAMP)* **42**(3), 370–388.
- Gurtin, M. E. (1996), ‘Generalized Ginzburg-Landau and Cahn-Hilliard equations based on a microforce balance’, *Phys. D: Nonlinear Phenomena* **92**(3–4), 178–192.
- Gurtin, M. E. (2000), *Configurational forces as basic concept of continuum physics*, Vol. 137 of *Applied Mathematical Sciences*, Springer-Verlag, New York, Berlin, Heidelberg.
- Gurtin, M. E. & Struthers, A. (1990), ‘Multiphase thermomechanics with interfacial structure; 3. Evolving phase boundaries in the presence of bulk deformation’, *Arch. Rational Mech. Anal.* **112**(2), 97–160.

- Gurtin, M. E. & Voorhees, P. W. (1993), 'The continuum mechanics of coherent two-phase elastic solids with mass transport', *Proc. R. Soc. Lond. A* **440**(1909), 323–343.
- Haupt, P. (2000), *Continuum mechanics and theory of materials*, Springer-Verlag, Berlin, Heidelberg, New York.
- Höchli, U. T. (1972), 'Elastic constants and soft optical modes in gadolinium molybdate', *Phys. Rev. B* **6**(5), 1814–1823.
- Holzappel, G. A. (2000), *Nonlinear solid mechanics: A continuum approach for engineering*, John Wiley & Sons, Ltd, Chichester, New York, Weinheim.
- Hu, H.-L. & Chen, L.-Q. (1997), 'Computer simulation of 90° ferroelectric domain formation in two-dimensions', *Mater. Sci. Eng. A* **238**(1), 182–191.
- Hu, H.-L. & Chen, L.-Q. (1998), 'Three-dimensional computer simulation of ferroelectric domain formation', *J. Am. Ceram. Soc.* **81**(3), 492–500.
- Huber, J. E. & Fleck, N. A. (2001), 'Multi-axial electrical switching of a ferroelectric: theory versus experiment', *J. Mech. Phys. Solids* **49**(4), 785–811.
- Huber, J. E., Fleck, N. A., Landis, C. M. & McMeeking, R. M. (1999), 'A constitutive model for ferroelectric polycrystals', *J. Mech. Phys. Solids* **47**(8), 1663–1697.
- Hughes, T. J. R. (2000), *The finite element method: Linear static and dynamic finite element analysis*, Dover Publications, Inc., Mineola, New York.
- Hwang, S. C. & Arlt, G. (2000), 'Switching in ferroelectric polycrystals', *J. Appl. Phys.* **87**(2), 869–875.
- Hwang, S. C., Lynch, C. S. & McMeeking, R. M. (1995), 'Ferroelectric/ferroelastic interactions and a polarization switching model', *Acta Metall. Mater.* **43**(5), 2073–2084.
- Ikeda, T. (1990), *Fundamentals of piezoelectricity*, Oxford University Press, Oxford.
- Jackson, J. D. (1999), *Classical electrodynamics*, 3rd edn, John Wiley & Sons, Inc., New York.
- Jaffe, B., Cook Jr., W. R. & Jaffe, H. (1971), *Piezoelectric ceramics*, Vol. 3 of *Non-metallic solids*, Academic Press, London.

- Jona, F. & Shirane, G. (1993), *Ferroelectric crystals*, Dover Publications, Inc., Mineola, New York.
- Kamlah, M. (2001), ‘Ferroelectric and ferroelastic piezoceramics – modeling of electromechanical hysteresis phenomena’, *Continuum Mech. Therm.* **13**(4), 219–268.
- Kamlah, M., Liskowsky, A. C., McMeeking, R. M. & Balke, H. (2005), ‘Finite element simulation of a polycrystalline ferroelectric based on a multidomain single crystal switching model’, *Int. J. Solids Struct.* **42**(9–10), 2949–2964.
- Kamlah, M. & Wang, Z. (2003), *A thermodynamically and microscopically motivated constitutive model for piezoceramics*, Wissenschaftliche Berichte FZKA 6880, Forschungszentrum Karlsruhe, Karlsruhe.
- Kessler, H. & Balke, H. (2006a), ‘A continuum analysis of charge induced ferroelectric domain wall motions’, *J. Mech. Phys. Solids* **54**(1), 86–112.
- Kessler, H. & Balke, H. (2006b), ‘A continuum analysis of the driving forces of ferroelectric/ferroelastic domain wall motions’, *J. Mech. Phys. Solids* **54**(1), 113–127.
- Keve, E. T., Abrahams, S. C. & Bernstein, J. L. (1971), ‘Ferroelectric ferroelastic paramagnetic beta-Gd<sub>2</sub>(MoO<sub>4</sub>)<sub>3</sub> crystal structure of the transition-metal molybdates and tungstates. VI’, *J. Chem. Phys.* **54**(7), 3185–3194.
- Kienzler, R. & Herrmann, G. (2000), *Mechanics in material space; with applications to defect and fracture mechanics*, Springer-Verlag, Berlin, Heidelberg, New York.
- Kim, S.-J., Choi, J. & Kwak, M. K. (2003), ‘A finite element prediction of ferroelectric switching behavior using a regular dodecahedron RVE’, *Comp. Mech.* **31**(6), 469–478.
- Kontsos, A. & Landis, C. M. (2009), ‘Computational modeling of domain wall interactions with dislocations in ferroelectric crystals’, *Int. J. Solids Struct.* **46**(6), 1491–1498.
- Landau, L. D. & Lifshitz, E. M. (1980), *The classical theory of fields*, Vol. 2 of *Course of theoretical physics*, 4th edn, Butterworth-Heinemann, Amsterdam, Boston, Heidelberg.

- Landau, L. & Lifshitz, E. (1984), *Electrodynamics of continuous media*, Vol. 8 of *Course of theoretical physics*, 2nd edn, Butterworth-Heinemann, Amsterdam, Boston, Heidelberg.
- Landis, C. M. (2002), ‘A new finite-element formulation for electromechanical boundary value problems’, *Int. J. Numer. Meth. Eng.* **55**(5), 613–628.
- Landis, C. M. (2004), ‘Non-linear constitutive modeling of ferroelectrics’, *Curr. Opin. Solid State Mater. Sci.* **8**(1), 59–69.
- Loge, R. E. & Suo, Z. (1996), ‘Nonequilibrium thermodynamics of ferroelectric domain evolution’, *Acta Mater.* **44**(8), 3429–3438.
- Lu, W., Fang, D.-N., Li, C. & Hwang, K.-C. (1999), ‘Nonlinear electric-mechanical behavior and micromechanical modelling of ferroelectric domain evolution’, *Acta Mater.* **47**(10), 2913–2926.
- Lupascu, D. C. (2004), *Fatigue in ferroelectric ceramics and related issues*, Springer-Verlag, Berlin, Heidelberg.
- Lupascu, D. C., Shur, V. Y. & Shur, A. G. (2002), ‘Dynamics of a single-planar domain wall in ferroelectric-ferroelastic  $\text{Gd}_2(\text{MoO}_4)_3$ ’, *Appl. Phys. Lett.* **80**(13), 2359–2361.
- Marsden, J. E. & Tromba, A. J. (2003), *Vector calculus*, 5th edn, W. H. Freeman Company, New York.
- Maugin, G. A. (1993), *Material inhomogeneities in elasticity*, Chapman & Hall, London, Glasgow, New York, Tokyo, Melbourne, Madras.
- McMeeking, R. M. & Landis, C. M. (2005), ‘Electrostatic forces and stored energy for deformable dielectric materials’, *J. Appl. Mech.* **72**(4), 581–590.
- McMeeking, R. M., Landis, C. M. & Jimenez, S. M. A. (2007), ‘A principle of virtual work for combined electrostatic and mechanical loading of materials’, *Int. J. Non-Linear Mech.* **42**(6), 831–838.
- Mehling, V. (2007), Phenomenological modeling of ferroelectric material behavior, PhD thesis, Technische Universität Darmstadt, Darmstadt.
- Merz, W. J. (1954), ‘Domain formation and domain wall motions in ferroelectric  $\text{BaTiO}_3$  single crystals’, *Phys. Rev.* **95**(3), 690–698.

- Meyer, B. & Vanderbilt, D. (2002), ‘*Ab initio* study of ferroelectric domain walls in  $\text{PbTiO}_3$ ’, *Phys. Rev. B* **65**(10), 104111.
- Michelitsch, T. & Kreher, W. S. (1998), ‘A simple model for the nonlinear material behavior of ferroelectrics’, *Acta Mater.* **46**(14), 5085–5094.
- Mokrý, P., Tagantsev, A. K. & Fousek, J. (2007), ‘Pressure on charged domain walls and additional imprint mechanism in ferroelectrics’, *Phys. Rev. B* **75**(9), 094110.
- Mueller, R., Gross, D. & Lupascu, D. C. (2006), ‘Driving forces on domain walls in ferroelectric materials and interaction with defects’, *Comput. Mater. Sci.* **35**(1), 42–52.
- Mueller, R., Kolling, S. & Gross, D. (2002), ‘On configurational forces in the context of the finite element method’, *Int. J. Numer. Meth. Eng.* **53**(7), 1557–1574.
- Newnham, R. E., McKinstry, H. A., Gregg, C. W. & Stitt, W. R. (1969), ‘Lattice parameters of ferroelectric rare earth molybdates’, *phys. status solidi (b)* **32**(1), K49–K51.
- Ogden, R. W. (1984), *Non-linear elastic deformations*, Dover Publications, Inc., Mineola, New York.
- Padilla, J., Zhong, W. & Vanderbilt, D. (1996), ‘First-principles investigation of  $180^\circ$  domain walls in  $\text{BaTiO}_3$ ’, *Phys. Rev. B* **53**(10), R5969–R5973.
- Purcell, E. M. (1965), *Electricity and magnetism*, Vol. 2 of *Berkeley physics course*, McGraw-Hill, Inc., New York.
- Schmidt, I. (1997), Gleichgewichtsmorphologien elastischer Einschlüsse, PhD thesis, Technische Hochschule Darmstadt, Darmstadt.
- Schmitt, L. A., Fuess, H., Schrade, D., Mueller, R., Xu, B.-X., Kungl, H. & Hoffmann, J. (2010), ‘Bimodal domain configuration in  $\text{Pb}[\text{Zr}_{0.375}\text{Ti}_{0.625}]\text{O}_3$  and  $\text{Pb}[\text{Zr}_{0.45}\text{Ti}_{0.55}]\text{O}_3$  ferroelectrics’. *In preparation*.
- Schmitt, L. A., Schönauf, K. A., Theissmann, R., Fuess, H., Kungl, H. & Hoffmann, M. (2007), ‘Composition dependence of the domain configuration and size in  $\text{Pb}(\text{Zr}_{1-x}\text{Ti}_x)\text{O}_3$  ceramics’, *J. Appl. Phys.* **101**(7), 074107.
- Schrade, D., Mueller, R., Gross, D., Utschig, T., Shur, V. Y. & Lupascu, D. C. (2007a), ‘Interaction of domain walls with defects in ferroelectric materials’, *Mech. Mater.* **39**(2), 161–174.

- Schrade, D., Mueller, R., Xu, B. X. & Gross, D. (2007b), ‘Domain evolution in ferroelectric materials: A continuum phase field model and finite element implementation’, *Comput. Meth. Appl. Mech. Eng.* **196**(41–44), 4365–4374.
- Schrade, D., Müller, R. & Gross, D. (2009), ‘Parameter identification in phase field models for ferroelectrics’, *Proc. Appl. Math. Mech.* **9**(1), 369–370.
- Schrade, D., Xu, B. X., Müller, R. & Gross, D. (2008), ‘On phase field modeling of ferroelectrics: parameter identification and verification’, *ASME Conf. Proc. (Smart Materials, Adaptive Structures and Intelligent Systems 2008)* **1**, 299–306.
- Scott, J. & Dawber, M. (2000), ‘Oxygen-vacancy ordering as a fatigue mechanism in perovskite ferroelectrics’, *Appl. Phys. Lett.* **76**(25), 3801–3803.
- Shur, V. Y., Gruverman, A. L., Kuminov, V. P. & Tonkachyova, N. A. (1990), ‘Dynamics of plane domain walls in lead germanate and gadolinium molybdate’, *Ferroelectrics* **111**(1), 197–206.
- Shur, V. Y., Gruverman, A. L., Kuminov, V. P. & Tonkachyova, N. A. (1992), ‘Dynamics of incoherent domain walls in gadolinium molybdate’, *Ferroelectrics* **130**(1), 341–346.
- Shur, V. Y., Nikolaeva, E. V., Rumyantsev, E. L., Shishkin, E. I., Subbotin, A. L. & Kozhevnikov, V. L. (1999), ‘Smooth and jump-like dynamics of the plane domain wall in gadolinium molybdate’, *Ferroelectrics* **222**(1), 323–331.
- Simha, N. K. & Bhattacharya, K. (1998), ‘Kinetics of phase boundaries with edges and junctions’, *J. Mech. Phys. Solids* **46**(12), 2323–2359.
- Simha, N. K. & Bhattacharya, K. (2000), ‘Kinetics of phase boundaries with edges and junctions in a three-dimensional multi-phase body’, *J. Mech. Phys. Solids* **48**(12), 2619–2641.
- Stemmer, S., Streiffer, S. K., Ernst, F. & Rühle, M. (1995), ‘Atomistic structure of 90° domain walls in ferroelectric PbTiO<sub>3</sub> thin films’, *Phil. Mag. A* **71**(3), 713–724.
- Su, Y. & Landis, C. M. (2007), ‘Continuum thermodynamics of ferroelectric domain evolution: theory, finite element implementation, and application to domain wall pinning’, *J. Mech. Phys. Solids* **55**(2), 280–305.

- Toda, M., Tosima, S., Shima, E. & Iwasa, T. (1973), ‘Variable delay devices using ferroelastic and ferroelectric crystal  $\text{Gd}_2(\text{MoO}_4)_3$ ’, *IEEE Trans. Son. Ultrason.* **SU-20**(4), 376–379.
- Toupin, R. A. (1956), ‘The elastic dielectric’, *J. Rational Mech. Anal.* **5**(6), 849–915.
- Tsakmakis, C. (1998), *Kontinuumsmechanik II*, Lecture script, Institut für Mechanik I, Technische Universität Darmstadt, Darmstadt.
- Utschig, T. (2005), Wechselwirkung ferroelektrischer Domänenwände mit geladenen und ungeladenen Defekten, PhD thesis, Technische Universität Darmstadt, Darmstadt.
- Vu, D. K., Steinmann, P. & Possart, G. (2006), ‘Numerical modelling of non-linear electroelasticity’, *Int. J. Numer. Meth. Eng.* **70**(6), 685–704.
- Wang, J. & Kamlah, M. (2008), ‘Domain structures of ferroelectric nanotubes controlled by surface charge compensation’, *Appl. Phys. Lett.* **93**(4), 042906.
- Wang, J., Shi, S.-Q., Chen, L.-Q., Li, Y. & Zhang, T.-Y. (2004), ‘Phase-field simulations of ferroelectric/ferroelastic polarization switching’, *Acta Mater.* **52**(3), 749–764.
- Wilmanski, K. (2008), *Continuum thermodynamics; Part I: Foundations*, Vol. 77 of *Series on advances in mathematics for applied sciences*, World Scientific Publishing Co. Pte. Ltd., New Jersey, London, Singapore, Beijing, Shanghai, Hong Kong, Taipei, Chennai.
- Wriggers, P. (2009), *Nonlinear finite element methods*, Springer-Verlag, Berlin, Heidelberg.
- Xu, Y. (1991), *Ferroelectric materials and their applications*, Elsevier Science Publishers B.V., Amsterdam.
- Yang, T. J., Gopalan, V., Swart, P. J. & Mohideen, U. (1999), ‘Direct observation of pinning and bowing of a single ferroelectric domain wall’, *Phys. Rev. Lett.* **82**(20), 4106–4109.
- Zhang, W. & Bhattacharya, K. (2005), ‘A computational model of ferroelectric domains. Part I: Model formulation and domain switching’, *Acta Mater.* **53**(1), 185–198.

- Zhou, D. (2003), *Experimental investigation of non-linear constitutive behavior of PZT piezoceramics*, Wissenschaftliche Berichte FZKA 6869, Forschungszentrum Karlsruhe, Karlsruhe.
- Zienkiewicz, O. C. & Taylor, R. L. (2000), *The finite element method*, 5th edn, Butterworth-Heinemann, Oxford, Auckland, Boston, Johannesburg, Melbourne, New Delhi.



# Lebenslauf

**David Schrade**

Sandbergstraße 37  
64285 Darmstadt

★ 7. November 1979 in Darmstadt

1999	Abitur an der Pestalozzischule Idstein (Gymnasium)
1999–2001	Studium des Bauingenieurwesens an der Technischen Universität Darmstadt
2001	Vordiplom in der Fachrichtung Bauingenieurwesen
2001–2004	Studium der Mechanik an der Technischen Universität Darmstadt
2004	Diplom in der Fachrichtung Mechanik
2004–2009	Wissenschaftlicher Mitarbeiter zunächst am Institut für Mechanik, Fachbereich Mechanik, dann am Fachgebiet Festkörpermechanik, Fachbereich Bauingenieurwesen und Geodäsie, Technische Universität Darmstadt
seitdem	Wohnhaft in Darmstadt